UNIVERSIDAD COMPLUTENSE DE MADRID
FACULTAD DE CIENCIAS FÍSICAS
Departamento de Física Teórica I

TESIS DOCTORAL

Long-time collisionless relaxation of zonal flows in toroidal fusion devices

Relajación no colisional y a tiempos largos de flujos zonales en dispositivos de fusión toroidales

MEMORIA PARA OPTAR AL GRADO DE DOCTOR

PRESENTADA POR

Pedro Monreal González

Directores

Iván Calvo Rubio
Edilberto Sánchez González

Madrid

ISBN: 978-84-09-18559-7

Long-time collisionless relaxation of zonal flows in toroidal fusion devices

Relajación no colisional y a tiempos largos de flujos zonales en dispositivos de fusión toroidales

Autor: Pedro Monreal González

Directores: Iván Calvo Rubio & Edilberto Sánchez González

TESIS DOCTORAL

Departamento de Física Teórica I

Facultad de Ciencias Físicas

UNIVERSIDAD COMPLUTENSE DE MADRID

Madrid, 2017.

Long-time collisionless relaxation of zonal flows in toroidal fusion devices

Relajación no colisional y a tiempos largos de flujos zonales en dispositivos de fusión toroidales

Tesis doctoral presentada por

Pedro Monreal González

para optar al grado de Doctor en Física.

Directores de la tesis: Iván Calvo Rubio y Edilberto Sánchez González,
Laboratorio Nacional de Fusión (CIEMAT).

Departamento de Física Teórica I

Facultad de Ciencias Físicas

UNIVERSIDAD COMPLUTENSE DE MADRID

Madrid, 2017.

Contents

Resumen

Relajación no colisional y a tiempos largos de flujos zonales en dispositivos de fusión toroidales

Los dispositivos más prometedores para la producción de energía de fusión por confinamiento magnético son los tokamaks y stellarators. Aunque estos conceptos han sido estudiados durante décadas, hay cuestiones importantes que siguen sin entenderse. Una de estas cuestiones está relacionada con la degradación del confinamiento debido al transporte turbulento de partículas y energía producido por las microinestabilidades en el plasma. Por lo tanto, la comprensión de la física que se esconde detrás de los mecanismos que controlan estas inestabilidades es de crucial importancia para el desarrollo de futuros reactores de fusión.

La reducción del transporte turbulento gracias a la acción de los flujos zonales, tanto en tokamaks como en stellarators, es un fenómeno conocido. Estos flujos están asociados a perturbaciones de potencial electrostático constantes en superficies de flujo y que tienen una estructura radial. Aunque la interacción entre la turbulencia y los flujos zonales es un proceso no lineal, el estudio de su relajación lineal proporciona una información muy útil sobre el problema y es interesante por varios motivos: Desde el punto de vista teórico, el proceso de relajación de una perturbación zonal puede describirse usando ecuaciones precisas y relativamente sencillas; podemos encontrar aproximaciones semianalíticas para entender mejor el problema físico y los resultados de las simulaciones girocinéticas; algunas de las magnitudes asociadas con el problema lineal son relevantes experimentalmente, por ejemplo la frecuencia de oscilación y los tiempos de decaimiento característicos.

Rosenbluth y Hinton estudiaron la evolución de una perturbación inicial de potencial zonal con número de onda pequeño en geometría de tokamak, mostrando que la perturbación no se amortigua completamente por procesos no colisionales sino que alcanza un valor finito a largo plazo, conocido como el nivel residual.

Recientemente, el análisis del problema se ha extendido a stellarators, aunque el nivel residual se ha estudiado principalmente para longitudes de

onda largas. Además, se ha demostrado que el proceso de relajación en los stellarators exhibe un rasgo característico, no presente en los tokamaks: una oscilación amortiguada. La frecuencia de esta oscilación y el nivel residual pueden ser parámetros relevantes en la regulación del transporte turbulento y, por tanto, su cálculo eficiente y preciso resulta de gran importancia.

En esta tesis, presentamos la derivación de las ecuaciones que describen la evolución no colisional y a tiempos largos de una perturbación inicial zonal en geometrías de tokamak y stellarator y para longitudes de onda arbitrarias. A partir de estas ecuaciones obtenemos las expresiones para el nivel residual y la frecuencia de oscilación de flujos zonales. La evaluación de dichas expresiones implica integraciones en el espacio de fases que no pueden ser realizadas analíticamente, excepto en geometrías de tokamak simplificadas. Por este motivo, desarrollamos el código CAS3D-K para evaluar rápida y exactamente estas expresiones. Utilizamos este método semianáltico para evaluar el nivel residual en dispositivos toroidales y comparamos nuestros cálculos con resultados analíticos y los resultados de dos códigos girocinéticos independientes, EUTERPE y GENE. Presentamos cálculos del nivel residual de flujos zonales en tokamaks y stellarators para una gama más amplia de longitudes de onda que las disponibles previamente en la literatura. Calculamos la frecuencia de flujos zonales en varios stellarators. También mostramos que nuestra herramienta numérica es más rápida que las simulaciones girocinéticas con diferencias de varios órdenes de magnitud en el tiempo de cálculo. Finalmente, presentamos la primera evidencia experimental de la oscilación de flujos zonales, medida en el stellarator TJ-II.

Esta tesis queda organizada de la siguiente manera:

- **Capítulo 1:** Presentamos los principales conceptos sobre la evolución de los flujos zonales en dispositivos de fusión por confinamiento magnético y su relación con la reducción del transporte turbulento.

- **Capítulo 2:** En este capítulo describimos analíticamente la evolución lineal y no colisional de los flujos zonales como un problema de valor inicial. Para ello, derivamos expresiones que describen el nivel residual en geometrías de tokamak y stellarator para longitudes de onda arbitrarias. También derivamos la expresión de la frecuencia de oscilación de flujos zonales en stellarators.

- **Capítulo 3:** En este capítulo damos una visión general de los métodos numéricos que se utilizan a lo largo de los siguientes capítulos. En particular, se pone especial énfasis en el desarrollo del código CAS3D-K relativo a la implementación de las operaciones de promediado que se usarán en los cálculos.

- **Capítulo 4:** Comparamos los cálculos semianalíticos del nivel residual en tokamaks y stellarators a longitudes de onda arbitrarias frente a

los resultados obtenidos de simulaciones con dos códigos girocinéticos independientes: el código global EUTERPE y la versión radialmente local de GENE. Dichas comparaciones muestran un acuerdo muy bueno. También mostramos que los cálculos con CAS3D-K (es decir, los cálculos semianalíticos) pueden ser de gran utilidad para evaluar de forma rápida y precisa el nivel residual y para realizar validaciones de códigos girocinéticos, especialmente en geometría de stellarator. El contenido de este capítulo está basado en el artículo [P Monreal *et al.* *Plasma Physics and Controlled Fusion* **58**, 045018 (2016), "Residual zonal flows in tokamaks and stellarators at arbitrary wavelengths"].

- **Capítulo 5:** En este capítulo se muestran cálculos semianalíticos y girocinéticos de la frecuencia de oscilación de flujos zonales. En particular, mostramos cálculos en una serie de tokamaks con relación de aspecto grande obtenidos con diferentes valores de rizado magnético y en los stellarators W7-X, TJ-II y LHD. Estas son las primeras comparaciones entre un método semianalítico y simulaciones girocinéticas. El contenido de este capítulo ha sido enviado recientemente para su publicación en una revista científica y puede encontrarse en la referencia [P Monreal *et al.* Aceptado para su publicación en *Plasma Physics and Controlled Fusion* "Semianalytical calculation of the zonal-flow oscillation frequency in stellarators"].

- **Capítulo 6:** Presentamos las primeras medidas experimentales de la oscilación de flujos zonales y su comparación con los cálculos obtenidos a través de los métodos numéricos descritos en el Capítulo 5. Estas comparaciones muestran en buen acuerdo, apoyando de este modo la validez de las predicciones teóricas de la frecuencia de flujos zonales. La mayor parte del contenido de este capítulo se encuentra en el artículo [J A Alonso *et al.* Aceptado para su publicación en *Physical Review Letters*, "Observation of oscillatory radial electric field relaxation in a helical plasma"].

- **Capítulo 7:** En el capítulo final presentamos las conclusiones y los principales resultados de esta tesis.

Abstract

Long-time collisionless relaxation of zonal flows in toroidal fusion devices

The most promising devices for the production of fusion energy in magnetic confinement are tokamaks and stellarators. Although these concepts have been studied for decades there are important issues that remain unsolved. One of these issues is related to the degradation of the confinement due to the turbulent transport of particles and energy produced by the microinstabilities in the plasma. Therefore, understanding the physics behind the mechanisms that control these instabilities is of crucial importance for the development of future fusion reactors.

The reduction of turbulent transport by zonal flows, in tokamaks and stellarators, is a widely accepted phenomenon. These flows are associated to electrostatic potential perturbations constant on flux surfaces with a radial structure. Although the interaction between turbulence and zonal flows is a non-linear process, the study of its linear relaxation is interesting for several reasons: From the theory point of view, the relaxation process of a zonal perturbation can be described using accurate and relatively easy equations; we can find semianalytical approximations to gain insight into the physical problem and the results from gyrokinetic simulations; some quantities associated with the linear problem are experimentally relevant, for example the oscillation frequency and characteristic decay times.

Rosenbluth and Hinton studied the evolution of an initial zonal potential perturbation with small wavenumber in tokamak geometry, showing that the perturbation is not completely damped by collisionless processes but reaches a finite value at long times, the so-called zonal-flow residual level.

Recently, the analysis of the problem has been extended to stellarators but the residual level has been studied mainly at long wavelengths. In addition, it has been shown that the relaxation process in stellarators exhibits a characteristic feature, not present in tokamaks: a damped oscillation. The frequency of this oscillation and the residual level might be relevant parameters in the regulation of turbulent transport, and therefore their efficient

and accurate calculation is important.

In this thesis, we present the equations that describe the long-time and collisionless evolution of an initial zonal perturbation in tokamak and stellarator geometries and for arbitrary wavelengths. Then, we obtain the expressions for the residual level and the zonal-flow oscillation frequency. The evaluation of such expressions involves phase-space integrations that cannot be performed analytically, except in simplified tokamak geometries. For this reason, we extend further a numerical tool to evaluate fast and accurately these expressions, the code CAS3D-K. We use this semianalytical method to evaluate the residual level in toroidal devices and we compare our calculations with analytical results and the results from two independent gyrokinetic codes, EUTERPE and GENE. We provide residual zonal-flow calculations in tokamaks and in stellarators for a wider range of wavelengths than previously available in the literature. We calculate the zonal-flow frequency in several stellarator devices. We also show that our numerical tool is faster than gyrokinetic simulations with differences of several orders of magnitude in computing time. Finally, we report on the first experimental evidence of the zonal-flow oscillation, measured in the TJ-II stellarator.

This thesis is organized as follows:

- **Chapter 1:** We introduce the main concepts regarding the evolution of zonal flows in magnetic confinement fusion devices and their relation with the reduction of turbulent transport.

- **Chapter 2:** In this chapter we describe analytically the linear and collisionless evolution of zonal flows as an initial value problem. We derive expressions for the residual zonal-flow level in tokamak and stellarator geometries and for arbitrary wavelengths. We also derive the expression of the zonal-flow oscillation frequency in stellarators.

- **Chapter 3:** In this chapter we give an overview of the numerical methods used throughout the following chapters. More emphasis is put on the code developments in CAS3D-K for the implementation of the required averaging operations that will be used in the semianalytical calculations.

- **Chapter 4:** In this chapter we compare semianalytical calculations of the residual zonal-flow level in tokamaks and stellarators at arbitrary wavelengths against the results obtained from simulations with two gyrokinetic codes: the global code EUTERPE and the radially local version of GENE. The comparisons show a very good agreement. We also show that the CAS3D-K calculations (namely, the semianalytical calculations) can be useful to evaluate fast and accurately the residual level and also to perform benchmarks of gyrokinetic codes, especially in stellarator geometry. The content of this chapter is based on the

paper [P Monreal *et al.* *Plasma Physics and Controlled Fusion* **58**, 045018 (2016), "Residual zonal flows in tokamaks and stellarators at arbitrary wavelengths"].

- **Chapter 5:** We show semianalytical and gyrokinetic calculations of the zonal-flow oscillation frequency. In particular, we show calculations in a series of large aspect ratio tokamaks with different ripple values and in the stellarators W7-X, TJ-II and LHD. These are the first comparisons between a semianalytical method and gyrokinetic simulations. The accuracy of the semianalytical method is checked by comparing its results against those obtained with gyrokinetic simulations. This chapter has been submitted for publication recently and can be found in reference [P Monreal *et al.* Accepted for publication in *Plasma Physics and Controlled Fusion* "Semianalytical calculation of the zonal-flow oscillation frequency in stellarators"].

- **Chapter 6:** In this chapter, we present the first experimental measurements of the zonal-flow oscillation and their comparison with calculations with the numerical methods described in Chapter 5. These comparisons show to be in good agreement, supporting the validity of the theoretical predictions of the zonal-flow frequency. Most of the content of this chapter is contained in the paper [J A Alonso *et al.* Accepted for publication in *Physical Review Letters*, "Observation of oscillatory radial electric field relaxation in a helical plasma"].

- **Chapter 7:** We devote the final chapter to present the conclusions and the main results of this thesis.

Chapter 1

Introduction

The objective of the fusion community is to produce economically viable nuclear fusion power plants. At the present moment, several concepts are under investigation and in magnetic confinement fusion tokamaks and stellarators are the most promising. These concepts have been widely studied using experimental, theoretical and numerical approaches but still today important issues remain unsolved. One of these issues is related to the degradation of the confinement due to anomalous transport of particles and energy which is produced by microinstabilities in the plasma. Therefore, understanding the mechanisms that control these instabilities and the concomitant turbulence is crucial for the development of future fusion reactors.

Zonal flows are believed to play a fundamental role in the reduction of anomalous transport in magnetic confinement fusion devices but the understanding of this process is still incomplete. These flows are associated to electrostatic potential perturbations which are constant on magnetic surfaces and have a radial dependence. In this work, we study important properties regarding the evolution of zonal flows in tokamaks and stellarators.

1.1 Zonal flows in magnetic confinement fusion

The vast majority of devices in magnetic confinement fusion have the topological form of a torus and the magnetic field lines lie on constant pressure surfaces. Charged particles move along these field lines describing a circular gyration and its radius of gyration is known as the gyroradius (or "Larmor radius"). Due to inhomogeneities of the magnetic field and the curvature of field lines, charged particles drift across field lines and cannot be confined unless the field lines are twisted and/or the entire torus is twisted. This line twisting can be expressed as a combination of a toroidal (the long way along the torus) and a poloidal (the short way around the torus) contribution. These helically twisted lines map out surfaces, which are called rational surfaces if the lines are closed and irrational if not. This concept gives rise

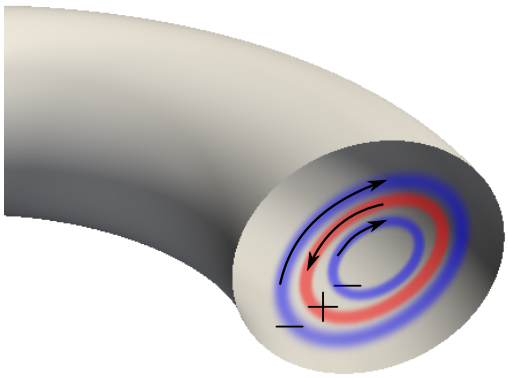

Figure 1.1: A zonal-flow is an electrostatic potential perturbation constant on magnetic surfaces with a radial structure.

to the two most prominent confinement systems, tokamaks and stellarators.

An ideal tokamak is axisymmetric and the toroidal magnetic field is generated by means of external coils, an additional poloidal magnetic field component is created by generating a toroidal current. In contrast, stellarators are non-axisymmetric devices in which the magnetic field is mainly produced by external coils.

Confined plasmas are in general unstable to perturbations that have a wavelength across the magnetic field comparable to, or smaller than the ion gyroradius, but with a wavelength along the magnetic field lines that is comparable with the size of the device. Such instabilities are called microinstabilities. Microinstabilities enhance the transport of particles and energy across the magnetic field lines, which is called turbulent transport, causing losses of particles and energy. The most relevant microinstabilities in toroidal plasmas are associated with drift waves [1], which take the free energy from density and temperature gradients.

As we have already mentioned, a zonal flow is a flow associated to an electrostatic perturbation constant on magnetic surfaces, which varies radially (see Figure 1.1). These flows act to reduce the turbulent transport caused by drift waves [2]. Whereas the reduction of turbulent transport by zonal flows is a widely accepted phenomenon [2, 3], its quantitative understanding is still poor. The determination of the zonal flow amplitude and turbulent transport level are nonlinear questions whose answers require costly gyrokinetic simulations. The cost grows enormously if, by means of parameter scans, one wants to know how those quantities depend on the magnetic geometry or the plasma conditions.

Although the generation process and the dynamics of zonal flows are non-linear phenomena and are influenced by particle collisions, the study of its linear evolution and in the collisionless regime is interesting for several reasons: It is possible to carry out gyrokinetic simulations with adequate

accuracy; from the theory point of view, we can find semianalytical approximations to gain insight into the physical problem and the results from simulations; some quantities associated with the linear problem are experimentally relevant (oscillation frequency, characteristic decay times, ...).

The theory of the linear and collisionless evolution of zonal flows, being more developed in tokamaks [4, 5, 6], is an active research topic in stellarators [7, 8, 9, 10, 11, 12]. The description of the collisionless relaxation of a zonal electrostatic potential perturbation makes use of gyrokinetics, the kinetic theory for strongly magnetized particles that is obtained by systematically averaging the fast quasiperiodic gyromotion of the particles around a magnetic field line to obtain a kinetic equation for the particles' gyrocentres. In tokamaks, Rosenbluth and Hinton [4] found that in the collisionless limit, long wavelength zonal flows are not completely damped, but a non-zero value is reached when $t \to \infty$, the so-called residual zonal-flow. In stellarator research, the interest in this problem was spurred by the suggestion [13] of a direct relation between zonal flow residual value and turbulent transport level. In stellarators [10, 11], unlike in a tokamak, the relaxation process to the residual value shows an oscillation, in general. This oscillation is caused by trapped particles having non-zero bounce averaged radial drift frequency.

The residual zonal-flow was computed in reference [4] for long wavelengths in a large aspect ratio, circular cross section tokamak with adiabatic electrons. An extension of the derivation of [4] was proposed in references [6, 14] to allow for short-wavelength perturbations, and also for kinetic electrons and more complex tokamak geometries. In reference [6], comparisons of analytical calculations with gyrokinetic simulations are shown. The enhancement of tokamak residual zonal flows at short wavelengths was originally found in reference [15] by means of gyrokinetic simulations with the code GS2. But the short-wavelength calculations of [6, 14, 15] do not correspond to an initial zonal value problem because the quasineutrality equation is forced with a source term. At long wavelengths, the initial value problem and the forced system give the same result.

In stellarators, the residual zonal-flow calculation has been done in [7, 10, 11, 12, 16]. In references [10, 11, 12] the emphasis is put on long-wavelength zonal flows. In references [7, 16], the derivation of the equations is valid for long and short-wavelengths but some approximations are used to describe the magnetic geometry.

As advanced above, in stellarators the relaxation process exhibits a characteristic feature: a damped oscillation, see Figure 1.2. In general, this relaxation involves two oscillations with different typical values of the frequency and also different physical origin. On the one hand, a decaying geodesic acoustic mode (GAM) oscillation with frequency Ω_{GAM} [17], mainly caused by the dynamics of passing ions. On the other hand, in [10] it was found that in stellarator geometry an additional oscillation takes place. Its frequency,

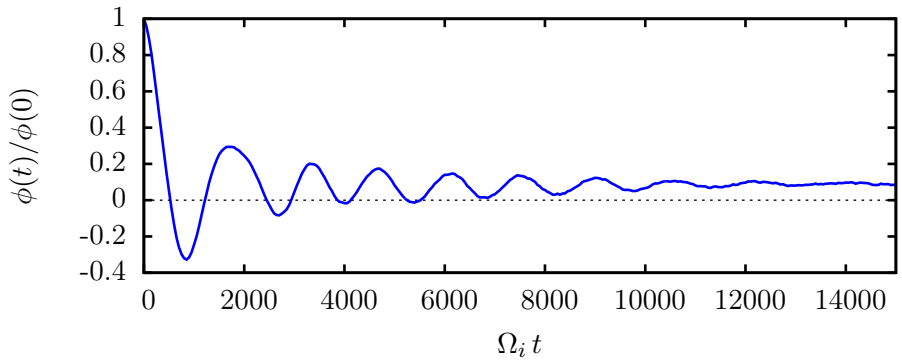

Figure 1.2: Typical time trace of a zonal electrostatic potential normalized to its initial value in a stellarator device.

that we denote by $\Omega_{\rm ZF}$, is significantly smaller than $\Omega_{\rm GAM}$, $\Omega_{\rm ZF} \ll \Omega_{\rm GAM}$. Unlike the GAM oscillation, that happens in tokamaks and stellarators, the slower oscillation is characteristic of stellarator geometries[1] and has been experimentally observed in [18]. From now on, when we refer to a zonal flow oscillation (or simply to an oscillation), and if not stated otherwise, we will understand that we are talking about the low frequency one.

The interest in the computation of $\Omega_{\rm ZF}$ resides in the potential role of the oscillation for the regulation of turbulent transport, pointed out in [12]. Since the residual value of the zonal flow is reached at times longer than the typical saturation time of the turbulence, the oscillatory phase of the zonal flow relaxation is likely to be physically more important than the value achieved when $t \to \infty$. Therefore, its efficient and accurate calculation is important. Although an analytical expression can be derived for the frequency, its numerical evaluation is not simple and has not been exploited systematically so far.

An analytical expression for $\Omega_{\rm ZF}$ was first derived in [10]. The oscillation was further studied, including its damping, in [11]. In reference [11], it was pointed out that it was unclear whether or not the analytical expression for the frequency is quantitatively accurate in actual devices. Anyway, the accuracy of the analytical expression has not been systematically checked so far, mainly because its evaluation is non-trivial: it involves phase-space averages that cannot be computed analytically in stellarator geometry, and therefore the evaluation must be carried out numerically.

[1] It is more precise to say that the oscillation with frequency $\Omega_{\rm ZF}$ exists only in non-omnigeneous devices. In particular, it can also manifest in rippled tokamaks (*i.e.* tokamaks with small variations on the magnetic field).

1.2 This thesis

In this thesis, we develop further the theory of the linear and collisionless evolution of zonal flows in tokamaks and stellarators. In particular, we derive an expression for the residual zonal-flow level in stellarator geometry for arbitrary wavelengths. We also recall the derivation of the expression of the zonal-flow frequency in stellarators. In general, the evaluation of these expressions involves certain averages over the trajectories of particles that cannot be performed analytically. For this purpose, we extend further the code CAS3D-K to include the precise evaluation of such expressions. We use this semianalytical method to evaluate the residual level in tokamaks and stellarators and we compare our calculations with analytical results and the results from two independent gyrokinetic codes, EUTERPE and GENE. Throughout this thesis, we will use "extension to CAS3D-K" and "semianalytical method" with the same meaning (for brevity, sometimes we will simply refer to the extended version of CAS3D-K as "CAS3D-K"). We also provide calculations of the zonal-flow oscillation frequency in a great variety of stellarator devices. In all the calculations, we note that the semianalytical method is much faster than gyrokinetic simulations with differences that can be of several orders of magnitude in computing time. In this thesis, we also report on the first experimental evidence of the zonal-flow oscillation, which has been measured in the TJ-II stellarator. We will see that these measurements are consistent with our theoretical predictions and numerical calculations.

This thesis is organized as follows. In Chapter 2 we derive the expressions for the residual zonal-flow level in tokamak and stellarator geometries and for arbitrary wavelengths. We also derive the expression of the zonal-flow oscillation frequency in stellarators. In Chapter 3 we give an overview of the numerical methods used throughout the following chapters. Emphasis is put on the code developments in CAS3D-K for the implementation of the required averaging operations. In Chapter 4 we compare semianalytical calculations of the residual zonal-flow level in tokamaks and stellarators at arbitrary wavelengths against the results obtained from gyrokinetic simulations. Chapter 4 is based on [19] [P Monreal *et al. Plasma Physics and Controlled Fusion* **58**, 045018 (2016), "Residual zonal flows in tokamaks and stellarators at arbitrary wavelengths"]. Semianalytical and gyrokinetic calculations of the zonal-flow oscillation frequency in stellarators are shown in Chapter 5 for several stellarator devices. The content of this chapter has been submitted for publication recently and can be found in Reference [20] [P Monreal *et al.* Accepted for publication in *Plasma Physics and Controlled Fusion* "Semianalytical calculation of the zonal-flow oscillation frequency in stellarators"]. In Chapter 6, we present the first experimental measurements of the zonal-flow oscillation and their comparison with the methods described

in Chapter 5. Most of the content of this chapter is contained in the paper [18] [J A Alonso *et al.* Accepted for publication in *Physical Review Letters*, "Observation of oscillatory radial electric field relaxation in a helical plasma"] that has been recently accepted for publication. Finally, the conclusions are presented in Chapter 7.

The work presented in this thesis has contributed to the following publications in scientific journals:

- "**Dynamics of flows and confinement in the TJ-II stellarator**". J Sánchez *et al. Nuclear Fusion* **53** 104016 (2013). [21]

- "**Collisionless damping of flows in the TJ-II stellarator**". E Sánchez, R Kleiber, R Hatzky, M Borchardt, P Monreal, F Castejón, A López-Fraguas, X Sáez, J L Velasco, I Calvo, A Alonso, D López-Bruna. *Plasma Physics and Controlled Fusion* **55**, 014015 (2013). [22]

- "**Transport, Stability and Plasma Control Studies in the TJ-II stellarator**". J Sánchez *et al. Nuclear Fusion* **55**, 104014 (2015). [23]

- "**Residual zonal flows in tokamaks and stellarators at arbitrary wavelengths**". P Monreal, I Calvo, E Sánchez, F I Parra, A Bustos, A Könies, R Kleiber, T Görler. *Plasma Physics and Controlled Fusion* **58**, 045018 (2016). [19]

- "**Observation of oscillatory radial electric field relaxation in a helical plasma**". J A Alonso, E Sánchez, I Calvo, J L Velasco, S Perfilov, A Chmyga, L G Eliseev, L I Krupnik, T Estrada, R Kleiber, K J McCarthy, A V Melnikov, P Monreal, F I Parra, I Zhezhera and the TJ-II Team. *Accepted for publication in Physical Review Letters.* [18]

- "**Semianalytical calculation of the zonal-flow oscillation frequency in stellarators**". P Monreal, E Sánchez, I Calvo, A Bustos, F I Parra, A Mishchenko, A Könies, R Kleiber. *Accepted for publication in Plasma Physics and Controlled Fusion.* [20]

and to the following contributions in conferences:

- "**Simulaciones girocinéticas de turbulencia en plasmas de fusión con geometría tridimensional**". E Sánchez, R Kleiber, R Hatzky, M Borchardt, P Monreal, F Castejón, A Soba, X Sáez, J M Cela. 33rd Biennial meeting of the Real Spanish Society of Physics & 21st Iberian Meeting of Physics Education, Santander (Spain). September 2011. Poster contribution.

- "**Non-collisional damping of flows in the TJ-II 3D geometry**". E Sánchez, R Kleiber, R Hatzky, M Borchardt, P Monreal, F Castejón, A López-Fraguas, X Sáez, J L Velasco, D López-Bruna, I Calvo, A Alonso. 19th European Fusion Physics Workshop (EFPW), Heringsdorf (Germany). December 2011. Oral contribution.

- "**Collisionless damping of flows in the TJ-II stellarator**". E Sánchez, R Kleiber, R Hatzky, M Borchardt, P Monreal, F Castejón, A López-Fraguas, X Sáez. 18th International Stellarator/Heliotron Workshop and 10th Asia Pacific Plasma Theory Conference, Australian National University, Canberra (Australia). January 2012. Oral contribution.

- "**Simulation of zonal flow relaxation in the TJ-II stellarator**". E Sánchez, R Kleiber, R Hatzky, M Borchardt, P Monreal, F Castejón, A López-Fraguas, X Sáez, J L Velasco, I Calvo, A Alonso and D López-Bruna. Gyrokinetic Theory Working Group Meeting 2012, Madrid (Spain). June 2012. Oral contribution.

- "**Residual zonal flow level in toroidally confined plasmas for arbitrary wavelengths**". P Monreal, I Calvo, E Sánchez, A Könies and R Kleiber. CSC 2013, International Conference on Scientific Computing 2013, Paphos (Cyprus). December 2013. Poster contribution.

- "**Residual zonal flow level in stellarators for arbitrary wavelengths**". P Monreal, I Calvo, E Sánchez, A Könies and R Kleiber. 41th European Physical Society Conference on Plasma Physics, Berlin (Germany). June 2014. Poster contribution.

- "**Influence of electric fields on zonal flows in stellarators**". E Sánchez, I Calvo, P Monreal, J L Velasco, A Alonso and R Kleiber. EFTSOMP: Electric Fields, Turbulence and Self-Organisation in Magnetized Plasmas, Lisbon (Portugal). June 2015. Oral contribution.

- "**Relaxation of zonal flows in stellarators: influence of the magnetic configuration"**. E Sánchez, P. Monreal, I. Calvo, R. Kleiber. 42nd European Physical Society Conference on Plasma Physics, Lisbon (Portugal). July 2015. Poster contribution.

Chapter 2

Linear and collisionless evolution of zonal flows at long times

In this chapter, we present the equations that describe the long-time and collisionless evolution of an initial zonal-flow perturbation in tokamak and stellarator geometries and for arbitrary wavelengths. Then, we derive expressions for the residual zonal-flow level (2.57) and the zonal-flow oscillation frequency (2.66). In the following chapters, we prove the validity of these expressions by comparing their numerical evaluation against gyrokinetic calculations. More details about the derivations described in this chapter can be found in References [19] and [20].

2.1 Magnetic coordinates

We introduce straight field line coordinates $\{\psi, \theta, \zeta\}$, where $\psi \in [0, 1]$ is the radial coordinate defined as the normalized toroidal flux $\psi = \Psi_t/\Psi_t^{\text{edge}}$, θ is a poloidal angle and ζ is a toroidal angle, with $\theta, \zeta \in [0, 1)$. The magnetic field in these coordinates is written in contravariant form as

$$\mathbf{B} = -\Psi_p'(\psi)\nabla\psi \times \nabla(\zeta - q(\psi)\theta), \tag{2.1}$$

where $q(\psi) = \Psi_t'(\psi)/\Psi_p'(\psi)$ is the safety factor, and $\Psi_p'(\psi)$ and $\Psi_t'(\psi)$ are the derivatives of the poloidal and toroidal fluxes with respect to ψ. If $\{\psi, \theta, \zeta\}$ are Boozer coordinates, then, the covariant form can be written as

$$\mathbf{B} = I_t\nabla\theta - I_p\nabla\zeta + \widetilde{\beta}\,(\psi, \theta, \zeta)\,\nabla\psi, \tag{2.2}$$

where $\widetilde{\beta}$ is a periodic function in θ and ζ. Here, $I_t = I_t(\psi)$ and $I_p = I_p(\psi)$ are the toroidal and poloidal currents, respectively. From (2.1) and (2.2) it

is clear that the expression for the square root of the metric determinant, $\sqrt{g} = [(\nabla\psi \times \nabla\theta) \cdot \nabla\zeta]^{-1}$, is then given by

$$\sqrt{g} = \frac{I_t \Psi_p' - I_p \Psi_t'}{B^2}. \tag{2.3}$$

In these coordinates, the flux surface average is defined by

$$\langle G \rangle_\psi = V'(\psi)^{-1} \int_0^1 \mathrm{d}\theta \int_0^1 \mathrm{d}\zeta \, \sqrt{g}\, G(\psi, \theta, \zeta), \tag{2.4}$$

for any given function $G(\psi, \theta, \zeta)$. Here,

$$V'(\psi) = \int_0^1 \mathrm{d}\theta \int_0^1 \mathrm{d}\zeta \, \sqrt{g} \tag{2.5}$$

is the derivative of the volume enclosed by the flux surface labeled by ψ.

It will be convenient to define the coordinate $\alpha := \zeta - q(\psi)\theta$, that labels magnetic field lines on each flux surface. Unless otherwise stated, we use $\{\psi, \theta, \alpha\}$ as the set of independent spatial coordinates. In these coordinates, the contravariant form of the magnetic field reads

$$\mathbf{B} = -\Psi_p'(\psi) \nabla\psi \times \nabla\alpha, \tag{2.6}$$

and the covariant form is given by

$$\mathbf{B} = (I_t - q I_p) \nabla\theta - I_p \nabla\alpha + \widetilde{\eta}\,(\psi, \theta, \alpha)\, \nabla\psi. \tag{2.7}$$

From (2.6) and (2.7), it is easy to see that the square root of the metric determinant in $\{\psi, \theta, \alpha\}$ coordinates has the same expression as in (2.3). Note that $\mathbf{B} \cdot \nabla\psi = 0$ and $\mathbf{B} \cdot \nabla\alpha = 0$. We employ θ as the coordinate along a field line.

2.2 Equations that describe the linear and collisionless evolution of a zonal perturbation at long times

In strongly magnetized plasmas, one employs the smallness of $\rho_{ts\star} = \rho_{ts}/L$ to average over the gyromotion. Here, L is the characteristic length of variation of the magnitude of the magnetic field[1] B, $\rho_{ts} = v_{ts}/\Omega_s$ is the thermal gyroradius, $v_{ts} = \sqrt{T_s/m_s}$ is the thermal speed, $\Omega_s = Z_s e B/m_s$ is the gyrofrequency, T_s is the equilibrium temperature, m_s is the mass, and $Z_s e$ is the charge of species s, where e is the proton charge. Gyrokinetic theory

[1] Typically, $L \sim R$, the major radius of the torus.

[24, 25, 26, 27, 28, 29] gives a procedure to rigorously derive the gyroaveraged kinetic equations order by order in $\rho_{ts\star} \ll 1$. The averaging operation is conveniently expressed in a new set of phase-space coordinates, called gyrokinetic coordinates. Denote by $\{\mathbf{r}, \mathbf{v}\}$ the particle position and velocity. The coordinate transformation, to lowest order in $\rho_{ts\star}$, is given by

$$\begin{aligned} \mathbf{r} &= \mathbf{R} + \boldsymbol{\rho}_s\left(\mathbf{R}, v, \lambda, \gamma\right) + O(\rho_{ts\star}^2 L), \\ \mathbf{v} &= v_\parallel\left(\mathbf{R}, v, \lambda, \sigma\right)\hat{\mathbf{b}}\left(\mathbf{R}\right) + \Omega_s \boldsymbol{\rho}_s\left(\mathbf{R}, v, \lambda, \gamma\right) \times \hat{\mathbf{b}}\left(\mathbf{R}\right) + O(\rho_{ts\star} v_{ts}). \end{aligned} \tag{2.8}$$

In equation (2.8), $\mathbf{R}$ is the gyrocenter position, v is the magnitude of $\mathbf{v}$, $\lambda = v_\perp^2/(Bv^2)$ is the pitch angle, $\sigma = v_\parallel/|v_\parallel|$ is the sign of the parallel velocity

$$v_\parallel\left(\mathbf{R}, v, \lambda, \sigma\right) = \sigma v\sqrt{1 - \lambda B(\mathbf{R})}, \tag{2.9}$$

$\hat{\mathbf{b}}$ is the unit vector in the direction of the magnetic field $\mathbf{B}$, $v_\perp$ is the component of the velocity perpendicular to $\mathbf{B}$, and $\boldsymbol{\rho}_s$ is the gyroradius vector, defined as

$$\boldsymbol{\rho}_s\left(\mathbf{R}, v, \lambda, \gamma\right) = \frac{m_s v}{Z_s e}\sqrt{\frac{\lambda}{B(\mathbf{R})}}\left[\hat{\mathbf{e}}_2(\mathbf{R})\cos\gamma - \hat{\mathbf{e}}_1(\mathbf{R})\sin\gamma\right]. \tag{2.10}$$

Here, $\hat{\mathbf{e}}_1(\mathbf{R})$ and $\hat{\mathbf{e}}_2(\mathbf{R})$ are unit vector fields orthogonal to each other which satisfy $\hat{\mathbf{e}}_1 \times \hat{\mathbf{e}}_2 = \hat{\mathbf{b}}$ at every point. Finally, the gyrophase γ is

$$\gamma = \arctan\left(\frac{\mathbf{v}\cdot\hat{\mathbf{e}}_2}{\mathbf{v}\cdot\hat{\mathbf{e}}_1}\right), \tag{2.11}$$

and the gyroaverage operation acting on any given function $Q(\mathbf{R}, v, \lambda, \sigma, \gamma, t)$ is defined as

$$\langle Q\rangle\left(\mathbf{R}, v, \lambda, \sigma, t\right) := \frac{1}{2\pi}\int_0^{2\pi} Q\left(\mathbf{R}, v, \lambda, \sigma, \gamma, t\right)\mathrm{d}\gamma. \tag{2.12}$$

The distribution function of particles using gyrokinetic coordinates, $F_s = F_s(\psi, \theta, \alpha, v, \lambda, \sigma, \gamma, t)$, can be written as

$$F_s(\mathbf{R}, v, \lambda, \sigma, \gamma, t) = F_{s0}(\mathbf{R}, v) + F_{s1}(\mathbf{R}, v, \lambda, \sigma, t) + O(\rho_{ts\star}^2 F_{s0}), \tag{2.13}$$

where $F_{s1} = O(\rho_{ts\star}F_{s0})$ and F_{s0} is a Maxwellian distribution whose density n_s and temperature $T_s = m_s v_{ts}^2$ are flux functions,

$$F_{s0}(\mathbf{R}, v) := \frac{n_s(\psi(\mathbf{R}))}{(\sqrt{2\pi}v_{ts}(\psi(\mathbf{R})))^3}\exp\left(-\frac{v^2}{2v_{ts}^2(\psi(\mathbf{R}))}\right). \tag{2.14}$$

The lowest-order quasineutrality condition implies $\sum_s Z_s e n_s(\psi) = 0$. Note that to $O(\rho_{ts\star}F_{s0})$ the distribution function is independent of the gyrophase.

The linear and collisionless time evolution of F_{s1} is given by [29, 30]

$$\begin{aligned}\partial_t H_{s1} + (v_\parallel \hat{\mathbf{b}} + \mathbf{v}_{ds}) \cdot \nabla H_{s1} = \frac{Z_s e}{T_s} \partial_t \langle\varphi\rangle F_{s0} \\ + \frac{1}{B}\left(\nabla\langle\varphi\rangle \times \hat{\mathbf{b}}\right) \cdot \nabla\psi \left[\frac{n_s'}{n_s} + \left(\frac{m_s v^2}{2T_s} + \frac{3}{2}\right)\frac{T_s'}{T_s}\right] F_{s0},\end{aligned} \tag{2.15}$$

where primes denote differentiation with respect to ψ, the function H_{s1} is defined by

$$H_{s1} = F_{s1} + \frac{Z_s e}{T_s}\langle\varphi\rangle F_{s0}, \tag{2.16}$$

the gyroaveraged electrostatic potential is

$$\langle\varphi\rangle(\mathbf{R}, v, \lambda, t) := \frac{1}{2\pi}\int_0^{2\pi} \varphi\left(\mathbf{R} + \boldsymbol{\rho}_s(\mathbf{R}, v, \lambda, \gamma), t\right) \mathrm{d}\gamma \tag{2.17}$$

and the magnetic drift velocity reads

$$\mathbf{v}_{ds} = \frac{v^2}{\Omega_s}\hat{\mathbf{b}} \times \left[(1 - \lambda B)\hat{\mathbf{b}} \cdot \nabla\hat{\mathbf{b}} + \frac{\lambda}{2}\nabla B\right]. \tag{2.18}$$

The orderings in gyrokinetic theory allow to separate the variations of the fields on the small and large scales, and decompose in Fourier modes with respect to the former. Since we are interested in studying the evolution of an electrostatic potential perturbation that depends only on ψ and the problem is linear, we can take a single mode of the form

$$\varphi(\mathbf{r}, t) = \varphi_k\left(\psi(\mathbf{r}), t\right) \exp(\mathrm{i}k_\psi \psi(\mathbf{r})). \tag{2.19}$$

Here,

$$\frac{1}{L} \ll k_\perp \lesssim \frac{1}{\rho_{ts}} \tag{2.20}$$

with $k_\perp(\mathbf{R}) = k_\psi |\nabla\psi(\mathbf{R})|$, and φ_k varies on the macroscopic scale L. Observe that, due to the effects of magnetic geometry, the dependence of φ_k on ψ cannot be avoided even for flat density and temperature profiles. A recent explanation of scale separation, as well as a proof of the equivalence between the local and global approaches to gyrokinetic theory can be found in [31].

To lowest order, the gyroaveraged electrostatic potential is

$$\langle\varphi\rangle(\mathbf{R}, v, \lambda, t) = \varphi_k(\psi(\mathbf{R}), t)\, J_0(k_\perp \rho_s) \exp(\mathrm{i}k_\psi \psi(\mathbf{R})), \tag{2.21}$$

where the magnitude of the gyroradius vector is

$$\rho_s(\mathbf{R}, v, \lambda) = \frac{m_s v}{Z_s e}\sqrt{\frac{\lambda}{B(\mathbf{R})}} \tag{2.22}$$

and J_0 is the zeroth-order Bessel function of the first kind,

$$J_0(x) = \frac{1}{2\pi}\int_0^{2\pi} \exp\left(\mathrm{i}x\sin\gamma\right)\mathrm{d}\gamma. \tag{2.23}$$

If the electrostatic potential has the form (2.19), then the distribution function can be written as

$$F_{s1}(\mathbf{R},v,\lambda,\sigma,t) = f_s(\psi(\mathbf{R}),\theta(\mathbf{R}),\alpha(\mathbf{R}),v,\lambda,\sigma,t)\,\exp(\mathrm{i}k_\psi\psi(\mathbf{R})) \tag{2.24}$$

and consequently

$$H_{s1}(\mathbf{R},v,\lambda,\sigma,t) = h_s(\psi(\mathbf{R}),\theta(\mathbf{R}),\alpha(\mathbf{R}),v,\lambda,\sigma,t)\,\exp(\mathrm{i}k_\psi\psi(\mathbf{R})), \tag{2.25}$$

where f_s and h_s vary on the scale L. Then, equation (2.15) becomes

$$\left(\partial_t + v_\parallel\,\hat{\mathbf{b}}\cdot\nabla + \mathrm{i}k_\psi\omega_s\right) h_s = \frac{Z_s e}{T_s}\,\partial_t\varphi_k J_{0s} F_{s0}, \tag{2.26}$$

where we have used the notation $\omega_s := \mathbf{v}_{ds}\cdot\nabla\psi$ for the radial magnetic drift frequency and $J_{0s}\equiv J_0(k_\perp\rho_s)$. From now on, and for brevity, we omit the dependence of φ_k on ψ; that is, we write $\varphi_k(t)$ instead of $\varphi_k(\psi,t)$.

Denote by ω the frequency associated to the time derivative in (2.26). The objective is to expand (2.26) in powers of $\omega/(v_{ts}L^{-1}) \ll 1$ and solve the lowest order equations to determine $\varphi_k(t)$. The $\omega/(v_{ts}L^{-1}) \ll 1$ expansion means, in particular, that we average over the lowest order particle trajectories and solve for time scales much longer than a typical orbit time, which is $O(L/v_{ts})$. We define the orbit average for a phase-space function $Q(\psi,\theta,\alpha,v,\lambda,\sigma,t)$ as

$$\overline{Q} := \begin{cases} \langle B\,Q/|v_\parallel|\rangle_\psi / \langle B/|v_\parallel|\rangle_\psi & \text{for passing particles} \\ \omega_b \oint \mathrm{d}\theta\, Q/(v_\parallel\,\hat{\mathbf{b}}\cdot\nabla\theta) & \text{for trapped particles,} \end{cases} \tag{2.27}$$

where $\omega_b := [\oint \mathrm{d}\theta/(v_\parallel\,\hat{\mathbf{b}}\cdot\nabla\theta)]^{-1}$ is the bounce frequency. The symbol $\oint$ stands for integration over the trapped trajectory, where the bounce points θ_b are the solutions of $1-\lambda B(\psi,\theta_b,\alpha)=0$ for given values of ψ and α, and given an initial condition for the particle trajectory.

Observe that the orbit average operation has the property

$$\overline{v_\parallel\hat{\mathbf{b}}\cdot\nabla Q} = 0 \tag{2.28}$$

for any single-valued function Q. We write the radial magnetic drift frequency as a sum of its orbit averaged and fluctuating parts

$$\omega_s = \overline{\omega_s} + v_\parallel\,\hat{\mathbf{b}}\cdot\nabla\delta_s, \tag{2.29}$$

where $\delta_s = \delta_s(\psi,\theta,\alpha,v,\lambda,\sigma)$, that we choose to be odd in σ, is the radial displacement of the particle's gyrocenter from its mean flux surface. Note that

in axisymmetric tokamaks and in omnigenous stellarators $\overline{\omega_s} = 0$ holds for all trajectories; in tokamaks with ripple and in non-omnigenous stellarators, one can only guarantee $\overline{\omega_s} = 0$ for passing particles.

A detailed derivation of the solution of the magnetic differential equation (2.29) that determines δ_s for passing and trapped particles is given in Appendix A and a discussion on its numerical evaluation is given in Section 3.2.3. In general, the solution to this equation can be written as

$$\delta_s = -\frac{I_p}{\Psi_p'}\rho_{\parallel s} + \widetilde{\delta_s}, \tag{2.30}$$

where the first term on the right hand side is the solution in axisymmetric devices and the term $\widetilde{\delta_s}$ represents the non-axisymmetric contribution. Here, the parallel gyroradius is defined as $\rho_{\parallel s} := v_\parallel/\Omega_s$. For passing particles, the solution to the magnetic differential equation is given by (A.7) and is found by using a Fourier transform in the periodic coordinates $\{\theta, \zeta\}$. For trapped particles, we obtain two equivalent solutions to the magnetic differential equation: an integral solution (A.14) and a solution using an expansion in bounce harmonics (A.17). As we will see in Section 3.2.3, the same accuracy can be achieved with both methods but the integral method has the advantage of being faster and less expensive in terms of computational resources.

Defining $\underline{h_s} := h_s \exp(\mathrm{i}k_\psi \delta_s)$ and $\underline{\varphi_k} := \varphi_k \exp(\mathrm{i}k_\psi \delta_s)$, equation (2.26) yields

$$\left(\partial_t + v_\parallel \hat{\mathbf{b}} \cdot \nabla + \mathrm{i}k_\psi \overline{\omega_s}\right) \underline{h_s} = \frac{Z_s e}{T_s} \partial_t \underline{\varphi_k} J_{0s} F_{s0}. \tag{2.31}$$

It is worth noting that the expansion in $\omega/(v_{ts}L^{-1})$ only makes sense if

$$\frac{k_\psi \overline{\omega_s}}{v_{ts}L^{-1}} \sim \frac{\omega}{v_{ts}L^{-1}} \ll 1. \tag{2.32}$$

For $k_\perp \rho_{ts} \sim 1$, this implies

$$\frac{\overline{\omega_s}}{\omega_s} \sim \frac{\omega}{v_{ts}L^{-1}} \ll 1. \tag{2.33}$$

This trivially holds in a tokamak because $\overline{\omega_s} = 0$ for all trajectories. In a generic stellarator, $\overline{\omega_s} = 0$ only for passing particles. Then, condition (2.33) requires that the secular radial drifts of trapped particles be sufficiently small. We assume that this is the case and carry out the expansion in $\omega/(v_{ts}L^{-1})$.

We write

$$\underline{h_s} = \underline{h_s^{(0)}} + \underline{h_s^{(1)}} + \underline{h_s^{(2)}} + \ldots, \tag{2.34}$$

with $\underline{h_s^{(j+1)}}/\underline{h_s^{(j)}} \sim \omega/(v_{ts}L^{-1})$. Then, we expand equation (2.31). To lowest order, one obtains

$$v_\parallel \hat{\mathbf{b}} \cdot \nabla \underline{h_s^{(0)}} = 0, \tag{2.35}$$

implying that $\underline{h_s^{(0)}}$ is constant along the lowest order trajectories; *i.e.*

$$\underline{h_s^{(0)}} = \overline{\underline{h_s^{(0)}}}. \tag{2.36}$$

To next order, we have

$$(\partial_t + \mathrm{i}k_\psi \overline{\omega_s})\, \underline{h_s^{(0)}} + v_\parallel \hat{\mathbf{b}} \cdot \nabla \underline{h_s^{(1)}} = \frac{Z_s e}{T_s} \partial_t \underline{\varphi_k} J_{0s} F_{s0}. \tag{2.37}$$

We do not write $\underline{\varphi_k^{(0)}}$ to ease the notation. The orbit average of (2.37) annihilates the term $v_\parallel \hat{\mathbf{b}} \cdot \nabla \underline{h_s^{(1)}}$, and we find

$$(\partial_t + \mathrm{i}k_\psi \overline{\omega_s})\, \underline{h_s^{(0)}} = \frac{Z_s e}{T_s}\, \overline{\partial_t \underline{\varphi_k}\, J_{0s}}\, F_{s0}. \tag{2.38}$$

It is useful to work in Laplace space in order to solve this equation. The Laplace transform of a function $Q(t)$ is defined as

$$\widehat{Q}(p) = \int_0^\infty Q(t)\, \mathrm{e}^{-pt} \mathrm{d}t, \tag{2.39}$$

where p denotes the variable in Laplace space. We apply it to (2.38) and obtain

$$(p + \mathrm{i}k_\psi \overline{\omega_s})\, \underline{\widehat{h}_s^{(0)}} = \frac{Z_s e}{T_s}\, p\, \overline{\underline{\widehat{\varphi}_k} J_{0s}}\, F_{s0} + \underline{f_s}(0). \tag{2.40}$$

Here, $\underline{f_s}(0) := f_s(0) \exp(\mathrm{i}k_\psi \delta_s)$ and $f_s(0)$ is the initial condition for f_s; *i.e.* $f_s(0) \equiv f_s(\psi, \theta, \alpha, v, \lambda, \sigma, 0)$. The solution of (2.40) yields

$$\widehat{h}_s^{(0)} = \frac{\mathrm{e}^{-\mathrm{i}k_\psi \delta_s}}{p + \mathrm{i}k_\psi \overline{\omega_s}} \left(\frac{Z_s e}{T_s} p\, \widehat{\varphi}_k\, \overline{\mathrm{e}^{\mathrm{i}k_\psi \delta_s} J_{0s}} F_{s0} + \overline{\mathrm{e}^{\mathrm{i}k_\psi \delta_s} f_s(0)} \right). \tag{2.41}$$

In order to have a closed system of equations we employ the gyrokinetic quasineutrality equation (see, for example, references [29, 30]),

$$\sum_s \frac{Z_s^2 e}{T_s} n_s\, \varphi(\mathbf{R}, t) = \sum_s Z_s \int H_s(\mathbf{R} - \boldsymbol{\rho}_s(\mathbf{R}, v, \lambda, \gamma), v, \lambda, \sigma, t) \mathrm{d}^3 v. \tag{2.42}$$

Here, we have used the short-hand notation $\int Q\, \mathrm{d}^3 v$ which means, for any given function $Q(\psi, \theta, \alpha, v, \lambda, \sigma, \gamma)$,

$$\int Q\, \mathrm{d}^3 v = \sum_{\sigma=-1}^{1} \int_0^{2\pi} \mathrm{d}\gamma \int_0^\infty \mathrm{d}v \int_0^{1/B} \mathrm{d}\lambda\, \frac{v^2 B}{2\sqrt{1 - \lambda B}} Q(\psi, \theta, \alpha, v, \lambda, \sigma, \gamma). \tag{2.43}$$

Using (2.19) and (2.25), and flux-surface averaging, we get

$$\sum_s \frac{Z_s^2 e}{T_s} n_s \, \varphi_k = \left\langle \sum_s Z_s \int J_{0s} h_s \mathrm{d}^3 v \right\rangle_\psi . \tag{2.44}$$

To lowest order in $\omega/(v_{ts}L^{-1}) \ll 1$, and after transforming to Laplace space, equation (2.44) gives

$$\sum_s \frac{Z_s^2 e}{T_s} n_s \, \widehat{\varphi}_k = \left\langle \sum_s Z_s \int J_{0s} \widehat{h}_s^{(0)} \mathrm{d}^3 v \right\rangle_\psi . \tag{2.45}$$

We employ (2.41) to write the right side of (2.45) in terms of the electrostatic potential and the initial condition, and solve for $\widehat{\varphi}_k$. The result is

$$\widehat{\varphi}_k(p) = \frac{\sum_s Z_s \left\{ \frac{1}{p + \mathrm{i} k_\psi \overline{\omega_s}} \mathrm{e}^{-\mathrm{i} k_\psi \delta_s} J_{0s} \overline{\mathrm{e}^{\mathrm{i} k_\psi \delta_s} f_s(0)} / F_{s0} \right\}_s}{\sum_s \frac{Z_s^2 e}{T_s} \left\{ 1 - \frac{p}{p + \mathrm{i} k_\psi \overline{\omega_s}} \mathrm{e}^{-\mathrm{i} k_\psi \delta_s} J_{0s} \overline{\mathrm{e}^{\mathrm{i} k_\psi \delta_s} J_{0s}} \right\}_s}, \tag{2.46}$$

where we have simplified the notation by defining

$$\{Q\}_s := \left\langle \sum_{\sigma=-1}^{1} \int_0^\infty \mathrm{d}v \int_0^{1/B} \mathrm{d}\lambda \, \frac{\pi v^2 B}{\sqrt{1 - \lambda B}} Q(\psi, \theta, \alpha, v, \lambda, \sigma) \, F_{s0} \right\rangle_\psi \tag{2.47}$$

for gyrophase independent functions on phase-space.

It is also convenient to give the expressions corresponding to the approximation of adiabatic electrons. Using this approximation, equation (2.44) can be written as

$$\sum_{s \neq e} \frac{Z_s^2 e}{T_s} n_s \, \varphi_k = \left\langle \sum_{s \neq e} Z_s \int J_{0s} h_s \, \mathrm{d}^3 v \right\rangle_\psi . \tag{2.48}$$

Therefore, the sum over species is then limited to just that of the ion species, $s \neq e$. Proceeding as shown previously for the fully kinetic case, we find that the expression for $\widehat{\varphi}_k(p)$ reads

$$\widehat{\varphi}_k(p) = \frac{\sum_{s \neq e} Z_s \left\{ \frac{1}{p + \mathrm{i} k_\psi \overline{\omega_s}} \mathrm{e}^{-\mathrm{i} k_\psi \delta_s} J_{0s} \overline{\mathrm{e}^{\mathrm{i} k_\psi \delta_s} f_s(0)} / F_{s0} \right\}_s}{\sum_{s \neq e} \frac{Z_s^2 e}{T_s} \left\{ 1 - \frac{p}{p + \mathrm{i} k_\psi \overline{\omega_s}} \mathrm{e}^{-\mathrm{i} k_\psi \delta_s} J_{0s} \overline{\mathrm{e}^{\mathrm{i} k_\psi \delta_s} J_{0s}} \right\}_s}. \tag{2.49}$$

2.3 Expression for the residual zonal-flow level

The residual zonal-flow level is found from the well-known property of the Laplace transform

$$\lim_{t \to \infty} \varphi_k(t) = \lim_{p \to 0} p \, \widehat{\varphi}_k(p). \tag{2.50}$$

Using this property in equation (2.46), we find that

$$\varphi_k(\infty) = \frac{\sum_s Z_s \left\{ \mathrm{e}^{-\mathrm{i}k_\psi \delta_s} J_{0s} \overline{\mathrm{e}^{\mathrm{i}k_\psi \delta_s} f_s(0)} / F_{s0} \right\}_s^{\overline{\omega_s}=0}}{\sum_s \frac{Z_s^2 e}{T_s} \left[\{1\}_s - \left\{ \mathrm{e}^{-\mathrm{i}k_\psi \delta_s} J_{0s} \overline{\mathrm{e}^{\mathrm{i}k_\psi \delta_s} J_{0s}} \right\}_s^{\overline{\omega_s}=0} \right]}, \tag{2.51}$$

where $\varphi_k(\infty) \equiv \lim_{t\to\infty} \varphi_k(t)$. The superscript $\overline{\omega_s} = 0$ means that the integration is performed only for particles whose trajectory satisfies $\overline{\omega_s} = 0$. In tokamaks, this property holds true for both trapped and passing particles, and therefore the integrals in (2.51) are performed over the whole phase-space. In stellarators, $\overline{\omega_s} = 0$ is satisfied exclusively for passing particles. Only in perfectly omnigenous stellarators [32, 33, 34] have trapped particles vanishing average radial magnetic drift. Hence, in a generic stellarator, the integrals in (2.51) with superscript $\overline{\omega_s} = 0$ are performed only over the passing region of phase-space.

The residual level is usually defined as the normalized value $\varphi_k(\infty)/\varphi_k(0)$, once an initial condition $f_s(0)$ has been specified. The relation between $f_s(0)$ and $\varphi_k(0)$ is given by the flux-surface averaged quasineutrality equation (2.44) at $t = 0$. Namely,

$$\sum_s \frac{Z_s^2 e}{T_s} n_s \left\langle 1 - \Gamma_0 \left(k_\perp^2 \rho_{ts}^2 \right) \right\rangle_\psi \varphi_k(0) = \left\langle \sum_s Z_s \int J_{0s} f_s(0) \mathrm{d}^3 v \right\rangle_\psi , \tag{2.52}$$

where we have used that

$$h_s(0) = f_s(0) + \frac{Z_s e}{T_s} \varphi_k(0) J_0(k_\perp \rho_s). \tag{2.53}$$

In equation (2.52) we have employed the identity

$$\int J_0^2 \left(k_\perp \rho_s \right) F_{s0} \mathrm{d}^3 v = n_s \Gamma_0 \left(k_\perp^2 \rho_{ts}^2 \right), \tag{2.54}$$

where the function $\Gamma_0 \left(k_\perp^2 \rho_{ts}^2 \right)$ is defined as

$$\Gamma_0 \left(k_\perp^2 \rho_{ts}^2 \right) := \exp \left(-k_\perp^2 \rho_{ts}^2 \right) \, I_0 \left(k_\perp^2 \rho_{ts}^2 \right). \tag{2.55}$$

Here, $I_0(x)$ is the zeroth-order modified Bessel function of the first kind. To simplify the notation, we use $\Gamma_{0s} \equiv \Gamma_0 \left(k_\perp^2 \rho_{ts}^2 \right)$.

An initial condition fulfilling equation (2.52) is

$$f_s(0) = \frac{Z_s e}{T_s} \frac{\langle 1 - \Gamma_{0s} \rangle_\psi}{\Gamma_{0s}} J_{0s} F_{s0} \, \varphi_k(0). \tag{2.56}$$

Using this initial condition, the residual zonal-flow level can be written as

$$\frac{\varphi_k(\infty)}{\varphi_k(0)} = \frac{\sum_s \frac{Z_s^2}{T_s} \left\{ \mathrm{e}^{-\mathrm{i}k_\psi \delta_s} J_{0s} \overline{\mathrm{e}^{\mathrm{i}k_\psi \delta_s} J_{0s} \left\langle 1 - \Gamma_{0s} \right\rangle_\psi / \Gamma_{0s}} \right\}_s^{\overline{\omega_s}=0}}{\sum_s \frac{Z_s^2}{T_s} \left[\{1\}_s - \left\{ \mathrm{e}^{-\mathrm{i}k_\psi \delta_s} J_{0s} \overline{\mathrm{e}^{\mathrm{i}k_\psi \delta_s} J_{0s}} \right\}_s^{\overline{\omega_s}=0} \right]}. \tag{2.57}$$

For later comparison with gyrokinetic simulations, it will be useful to have at hand the expression corresponding to the approximation of adiabatic electrons. This can be obtained as for the fully kinetic case from (2.49). We find that the expression for $\varphi_k(\infty)$ reads

$$\varphi_k(\infty) = \frac{\sum_{s\neq e} Z_s \left\{ \mathrm{e}^{-\mathrm{i}k_\psi \delta_s} J_{0s} \overline{\mathrm{e}^{\mathrm{i}k_\psi \delta_s} f_s(0)}/F_{s0} \right\}_s^{\overline{\omega_s}=0}}{\sum_{s\neq e} \frac{Z_s^2 e}{T_s} \left[\{1\}_s - \left\{ \mathrm{e}^{-\mathrm{i}k_\psi \delta_s} J_{0s} \overline{\mathrm{e}^{\mathrm{i}k_\psi \delta_s} J_{0s}} \right\}_s^{\overline{\omega_s}=0} \right]}. \tag{2.58}$$

Finally, using the initial condition (2.56), we can write the residual zonal-flow level with the approximation of adiabatic electrons as

$$\frac{\varphi_k(\infty)}{\varphi_k(0)} = \frac{\sum_{s\neq e} \frac{Z_s^2}{T_s} \left\{ \mathrm{e}^{-\mathrm{i}k_\psi \delta_s} J_{0s} \overline{\mathrm{e}^{\mathrm{i}k_\psi \delta_s} J_{0s} \langle 1 - \Gamma_{0s} \rangle_\psi / \Gamma_{0s}} \right\}_s^{\overline{\omega_s}=0}}{\sum_{s\neq e} \frac{Z_s^2}{T_s} \left[\{1\}_s - \left\{ \mathrm{e}^{-\mathrm{i}k_\psi \delta_s} J_{0s} \overline{\mathrm{e}^{\mathrm{i}k_\psi \delta_s} J_{0s}} \right\}_s^{\overline{\omega_s}=0} \right]}. \tag{2.59}$$

In Chapter 4, we calculate the residual level with fully kinetic species (2.57) and when using the adiabatic electron approximation (2.59) in tokamak and stellarator geometries at arbitrary wavelengths. The semianalytical method, described in Chapter 3, is compared against the results from two independent gyrokinetic codes, a global and a local code. Benchmarks of the semianalytical method against analytical results and other numerical calculations available in the literature are also given. In Chapter 4, we also discuss the validity of the residual zonal-flow equations and the computational cost required to obtain its value with the different numerical methods.

2.4 Expression for the zonal-flow oscillation frequency

In this section, our goal is to derive an expression for the zonal-flow oscillation frequency, Ω_{ZF}. This can be obtained from equation (2.46) with the initial condition (2.56), which reads

$$\frac{\widehat{\varphi}_k(p)}{\varphi_k(0)} = \frac{\sum_s \frac{Z_s^2}{T_s} \left\{ \frac{1}{p+\mathrm{i}k_\psi \overline{\omega_s}} \mathrm{e}^{-\mathrm{i}k_\psi \delta_s} J_{0s} \overline{\mathrm{e}^{\mathrm{i}k_\psi \delta_s} J_{0s} \langle 1 - \Gamma_{0s} \rangle_\psi / \Gamma_{0s}} \right\}_s}{\sum_s \frac{Z_s^2}{T_s} \left\{ 1 - \frac{p}{p+\mathrm{i}k_\psi \overline{\omega_s}} \mathrm{e}^{-\mathrm{i}k_\psi \delta_s} J_{0s} \overline{\mathrm{e}^{\mathrm{i}k_\psi \delta_s} J_{0s}} \right\}_s}, \tag{2.60}$$

and expanding in powers of $k_\psi \overline{\omega_s}/p \ll 1$, and keeping the lowest order terms in $k_\perp \rho_{ts} \sim k_\psi \delta_s \ll 1$ (see Appendix B for details on the power series expansions of the functions involved). A direct check shows that, with these approximations, we can write

$$\frac{\widehat{\varphi}_k(p)}{\varphi_k(0)} = \frac{1}{p\,(1 + A_1/A_0) + p^{-1} A_2/A_0}, \tag{2.61}$$

where

$$A_0 = \sum_s n_s \frac{Z_s^2}{T_s} \left\langle |\nabla\psi|^2 \rho_{ts}^2 \right\rangle_\psi , \tag{2.62}$$

$$A_1 = \sum_s \frac{Z_s^2}{T_s} \left\{ \overline{\delta_s^2} - \overline{\delta_s}^2 \right\}_s \tag{2.63}$$

and

$$A_2 = \sum_s \frac{Z_s^2}{T_s} \left\{ \overline{\omega_s}^2 \right\}_s . \tag{2.64}$$

Taking the inverse Laplace transform of equation (2.61), we obtain the same result as in references [10, 11], namely

$$\frac{\varphi_k(t)}{\varphi_k(0)} = \frac{1}{1 + A_1/A_0} \cos\left(\Omega_{\mathrm{ZF}} t\right), \tag{2.65}$$

where the zonal-flow oscillation frequency is given by

$$\Omega_{\mathrm{ZF}} = \sqrt{\frac{A_2/A_0}{1 + A_1/A_0}}, \tag{2.66}$$

and the amplitude of this oscillation can be written as

$$A_{\mathrm{ZF}} = \frac{1}{1 + A_1/A_0}. \tag{2.67}$$

Note that the expressions for the zonal-flow frequency and its amplitude do not depend on the radial wavenumber k_ψ, and that A_{ZF} is independent of the temperatures and the masses of the species.

Whereas the frequency is a quantity that can be meaningfully compared with gyrokinetic simulations, the situation is different regarding the amplitude of the oscillation. The problem is that in practice the amplitude is damped [11], and in the analytical calculation above we have not considered the damping. For this reason, and due to the fact that Ω_{ZF} seems to be more physically relevant, we focus on it in what follows.

The zonal-flow frequency (2.66) and the amplitude (2.67) were first derived in [10] and the problem was analyzed in more detail in [11], where it was pointed out that the ordering (2.20) might be difficult to satisfy in actual devices, and therefore the usefulness of (2.66) was unclear in quantitative terms. The validity of the derived expression for Ω_{ZF} is consistent with the orderings enumerated just before (2.61) because

$$\frac{k_\psi \overline{\omega_s}}{\Omega_{\mathrm{ZF}}} \sim k_\perp \rho_{ts} \ll 1. \tag{2.68}$$

If we recall (2.20), we deduce that (2.66) is correct as long as

$$\frac{1}{L} \ll k_\perp \ll \frac{1}{\rho_{ts}} \tag{2.69}$$

is satisfied. In Chapter 5, we address a systematic comparison of the right side of (2.66) with the value of Ω_{ZF} obtained through gyrokinetic simulations. It turns out that (2.66) is accurate (although there are a number of nuances about the assessment of the accuracy, depending on the device and associated to both the analytical calculation and the fitting of the frequency from gyrokinetic simulations, that are pointed out in the following sections of that chapter) and that the numerical methods that we present to evaluate the right side of (2.66) are faster than the determination of the frequency from gyrokinetic codes.

Chapter 3

Numerical codes employed in this thesis

In the previous chapter, we derived expressions for the residual zonal-flow level (2.57) and the zonal-flow oscillation frequency (2.66), among other quantities. These expressions involve averages over the lowest order trajectories of particles that typically cannot be evaluated analytically. In order to compute these averages, we use the framework of the code CAS3D-K [35, 36] and include the relevant finite Larmor radius effects, the finite orbit-width effects obtained as the solution to the magnetic differential equation (2.30) (described in Appendix A) and the integration over the velocity coordinates v and σ. Throughout this thesis, we will use the terminology "CAS3D-K", "extension to CAS3D-K" and "semianalytical method" indistinctly. A basic description of CAS3D-K is given in Section 3.1 and the modifications included in the code are explained in detail in Section 3.2. In the following chapters, we compare semianalytical calculations with two independent gyrokinetic codes, EUTERPE [37, 38] and GENE [15, 39, 40, 41], with different numerical schemes. A description of these codes is also given in Sections 3.3 and 3.4.

3.1 Overview of the CAS3D-K code

The code CAS3D-K was originally developed from the three-dimensional ideal MHD stability code package CAS3D [42, 43, 44] to include a numerical solution of the drift-kinetic equation. CAS3D-K has been used extensively to study several kinetic properties of Alfvén modes in tokamaks and stellarators and has been fully benchmarked against analytical results, gyrokinetic codes and other kinetic-MHD codes [45, 46, 47, 48]. CAS3D-K uses no approximations in the magnetic field but neglects finite Larmor radius and finite orbit-width effects. The code is written in C, C++ and FORTRAN and is parallelized with MPI.

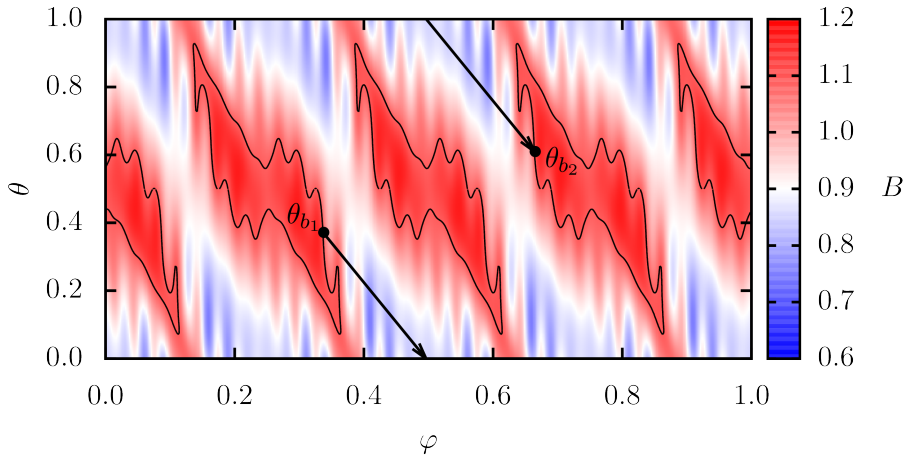

Figure 3.1: Plot of the magnetic field of the TJ-II stellarator standard configuration at a radial position of $\psi = 0.5$, showing a contour line with $\lambda = 0.917$. An example of a trapped trajectory for this value of λ, and its bounce points θ_{b_1} and θ_{b_2}, is also shown.

CAS3D-K is well suited to perform the bounce average operation (2.27) in arbitrary tokamak or stellarator geometries. This operation is performed over the lowest order trajectories of particles and requires a precise description of the magnetic field. Since CAS3D-K uses no approximations in the geometry, we found its original framework as a convenient starting point for our purposes.

CAS3D-K requires the magnetic equilibrium quantities and the density and temperature radial profiles of the considered species as input. The magnetic equilibrium is obtained from the 3D MHD equilibrium code VMEC [49] (Variational Moments Equilibrium Code) which is able to get the MHD equilibrium magnetic field. VMEC assumes the existence of nested flux surfaces and that the quantities can be expanded in Fourier series in the poloidal and toroidal coordinates. The equilibrium obtained from VMEC is then transformed to Boozer coordinates with the code MC3D and the equilibrium quantities for the CAS3D-K input are mapped into a grid or expressed as Fourier mode amplitudes.

For the description of the magnetic field, CAS3D-K uses Boozer coordinates and pitch-angle variables for the velocity space. The Boozer coordinates in CAS3D-K can be written as $\{\psi, \theta, \zeta\}$, where the radial coordinate ψ is defined as the normalized toroidal flux $\psi := \Psi_t/\Psi_t^{\text{edge}}$, $\theta \in [0, 1)$ is the normalized poloidal angle and $\zeta \in [0, 1)$ is the normalized toroidal angle.

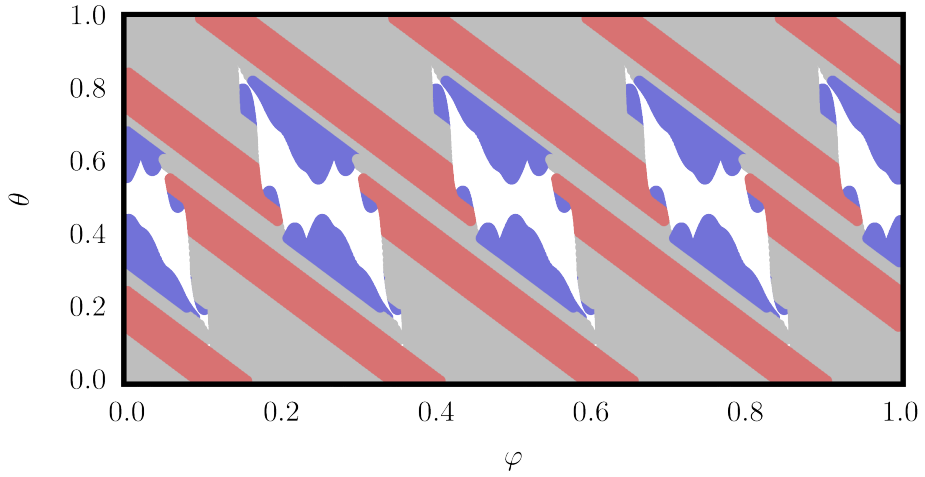

Figure 3.2: Groups of trajectories of particles and bounce points in Boozer coordinates for $\lambda = 0.917$ and $\psi = 0.5$ in the standard configuration of the TJ-II stellarator. The groups number the periods that particles cross between the bounce points; blue means one period; gray two periods; and red three periods.

The magnetic field is described by equations (2.1) and (2.2). Note that, the lowest order trajectories of particles are straight in these coordinates. For the independent velocity coordinates the code uses $\{v, \lambda, \sigma\}$, where v is the total velocity, the pitch angle variable is defined as $\lambda := v_\perp^2/(Bv^2)$ and $\sigma := v_\parallel/|v_\parallel|$ is the sign of the parallel velocity. Note that, these phase-space coordinates are the same as those described in Chapter 2.

Since the lowest order particle trajectories lie entirely on flux surfaces, all the calculations are local, thus permitting a parallelization by flux surface using MPI (Message-Passing interface). On a given flux surface, the pitch angle λ distinguishes between passing and trapped trajectories. The passing-trapped boundary is given by $\lambda_c = 1/B^{\max}$, where $B^{\max}$ is the maximum of B on the flux surface. Passing particles have λ values with $0 < \lambda < \lambda_c$ and trapped particles are those with $\lambda_c < \lambda < 1/B^{\min}$, where $B^{\min}$ is the minimum of B on the flux surface. Trapped particles can live inside one or several magnetic field periods. In CAS3D-K, the trapped particles are grouped by the number of periods they go through. The groups are obtained by setting a large number of initial conditions for the trajectories covering the whole flux surface, and finding the bounce points θ_b from the bounce condition $1 - \lambda B(\psi, \theta_b, \alpha) = 0$ for constant ψ and α, for each trajectory. An example of a trapped trajectory covering two periods and its bounce points is shown in Figure 3.1. From this root finding procedure, the boundaries of each group are found and the numerical integration for a given group is performed

by covering the region they define with new trajectories. The corresponding groups of trajectories covering one, two and three magnetic field periods are given in Figure 3.2. Note that each group requires different numerical resolution. Some trapped trajectories close to the passing-trapped boundary may require a large number of periods until the bounce points are found. If this number is sufficiently large, typically larger than 500 periods, the trajectories are then considered as passing. A Gauss-Legendre quadrature scheme is used for the integration in θ, α and λ, which avoids the numerical problems that may appear at points where $1 - \lambda B = 0$.

In this work, we take the framework of CAS3D-K and include the required modifications to calculate the quantities derived in the previous chapter. These modifications are described in the following section.

3.2 Improvements included in CAS3D-K

In this work, we are interested in the evaluation of the expressions derived in Chapter 2 for the residual zonal-flow level (2.57) and the zonal-flow oscillation frequency (2.66), among others. In general, these expressions require the numerical evaluation of phase-space integrations with the general form

$$\left\{P\,\overline{Q}\right\}_s := \left\langle \sum_{\sigma=-1}^{1} \int_0^\infty \mathrm{d}v \int_0^{1/B} \mathrm{d}\lambda \, \frac{\pi v^2 B}{\sqrt{1-\lambda B}}\, P\,\overline{Q}\, F_{s0} \right\rangle_\psi , \tag{3.1}$$

for any given functions $P = P(\psi, \theta, \alpha, v, \lambda, \sigma)$ and $Q = Q(\psi, \theta, \alpha, v, \lambda, \sigma)$. To perform these averages, we have included in CAS3D-K the required modifications to calculate the expression (3.1) in arbitrary toroidal geometry. In particular, we have implemented the numerical integration over the velocity coordinates v and σ, the finite Larmor radius and finite orbit-width effects and the solution of the magnetic differential equations that describe the expression of δ_s (2.29) both for passing and trapped particles and with no approximations. A description of these modifications is given next.

3.2.1 Bounce averaged radial drift frequency

As described in Chapter 2, the bounce averaged radial drift frequency, $\overline{\omega_s}$, vanishes for all trajectories in axisymmetric tokamaks and in omnigenous stellarators. In tokamaks with ripple and non-omnigenous stellarators $\overline{\omega_s} = 0$ holds true only for passing particles. For trapped particles, this quantity is reduced to

$$\overline{\omega_s} = \frac{m_s v^2}{Z_s e} \overline{\frac{(2-\lambda B)}{2B\Psi_p'} \partial_\alpha B}. \tag{3.2}$$

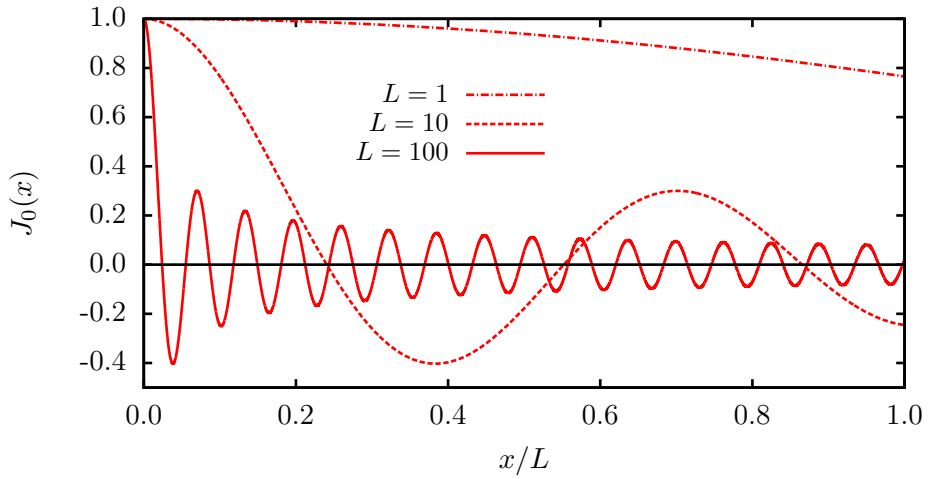

Figure 3.3: Plot of $J_0(x)$, the zeroth-order Bessel function of the first kind, for several values of the argument x.

The calculation of this quantity is crucial for the understanding of the zonal-flow oscillation frequency (2.66). In this equation, $\overline{\omega_s}$ enters throughout the term A_2 which is given by equation (2.64).

The evaluation of expression (3.2) requires the calculation of the α-derivatives of the magnetic field. To perform these derivatives at any given particle's position along a trapped trajectory, a linear five-point stencil in one dimension has been implemented in CAS3D-K. This method, which ensures enough precision in the evaluation of the α-derivatives, is given by

$$\begin{aligned}\frac{\partial B(\theta,\alpha)}{\partial \alpha} =& \frac{B(\theta,\alpha-2\Delta\alpha)-B(\theta,\alpha+2\Delta\alpha)}{12\Delta\alpha}+ \\ & \frac{2B(\theta,\alpha+\Delta\alpha)-2B(\theta,\alpha-\Delta\alpha)}{3\Delta\alpha}+O\left((\Delta\alpha)^4\right),\end{aligned} \tag{3.3}$$

where $\Delta\alpha$ is the differential step in the α-direction and the estimated error is of $O\left((\Delta\alpha)^4\right)$. In general, we take a value of $\Delta\alpha = 1/512$ which guaranties enough accuracy in the calculations shown in this work.

Due to the highly oscillatory behavior of ω_s, its bounce average requires extraordinary large precision and resolution in the spatial coordinates. For the implementation of the bounce-average operation $\overline{\omega_s}$ in CAS3D-K, we use a Gauss-Legendre quadrature scheme.

3.2.2 Finite Larmor radius effects

As described in Chapter 2, the finite Larmor radius effects are related to terms including ρ_s, the Larmor radius, or ρ_{ts}, the thermal Larmor radius. In the equation that describes the residual zonal-flow level (2.57), these effects

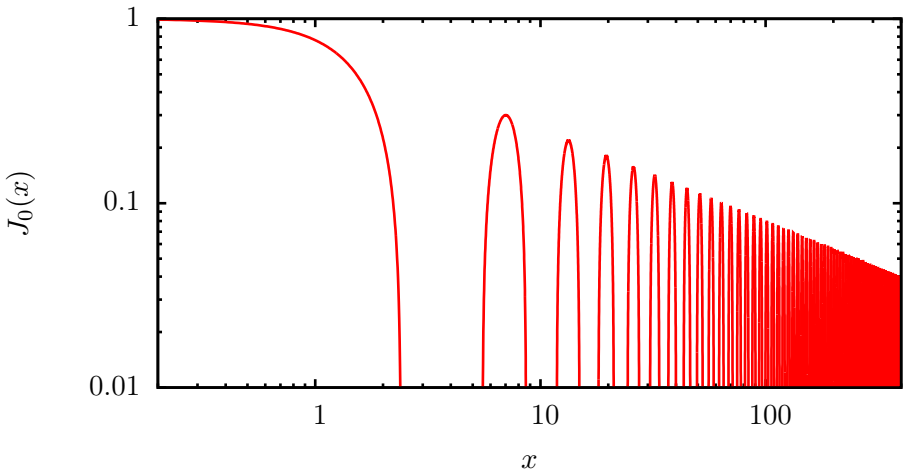

Figure 3.4: Logarithmic plot of $J_0(x)$, the zeroth-order Bessel function of the first kind, showing a power-law decay proportional to $1/\sqrt{x}$ for large values of the argument.

are encoded in the functions $J_0(k_\perp \rho_s)$ and $\Gamma_0\left(k_\perp^2 \rho_{ts}^2\right)$. Here, $J_0(x)$ is the zeroth-order Bessel function of the first kind and $\Gamma_0(x) := \exp(-x) I_0(x)$, where $I_0(x)$ is the zeroth-order modified Bessel function. The finite Larmor radius effects are also present in the term A_0 of the zonal-flow frequency equation (2.66). Here, we comment on the implementation of these effects in CAS3D-K.

First, let us discuss some properties of the Bessel function $J_0(x)$. In figure 3.3, we show a plot of this function for different ranges of the argument. As can be seen in this figure, $J_0(x)$ shows a strong oscillatory behavior for large values of the argument. It is then clear that large numerical resolutions would be required to correctly integrate this function under these conditions. One interesting property of $J_0(x)$ is that it shows an amplitude decay which is proportional to $1/\sqrt{x}$. In particular, for large values of the argument x, the Bessel function can be approximated by

$$J_0(x) \sim \sqrt{\frac{2}{\pi x}} \cos\left(x - \frac{\pi}{4}\right). \tag{3.4}$$

This power-law decay can be seen more clearly in the log-log plot given in figure 3.4. Another interesting property is that the roots of $J_0(x)$ are not periodic, except asymptotically for large values of the argument, and the distance between zeroes reaches its maximum value, π, in the limit $x \to \infty$. From these properties, we can estimate the resolution required in the numerical integration of functions containing $J_0(x)$. See Appendix B for information about the power series expansions of the $J_0(x)$ Bessel function and the Gamma function $\Gamma_0(x)$.

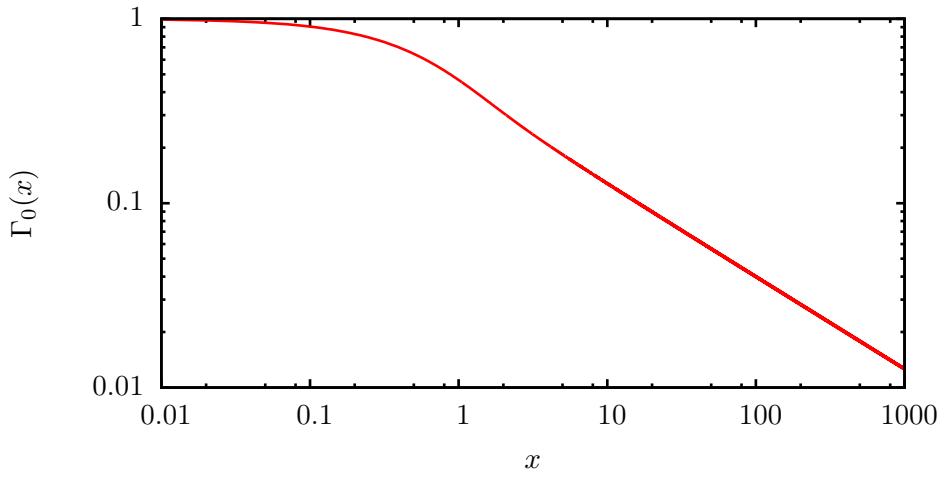

Figure 3.5: Logarithmic plot of $\Gamma_0(x) := \exp(-x)I_0(x)$, where $I_0(x)$ is the zeroth-order Bessel function of the first kind, showing a decay proportional to $1/\sqrt{x}$ for large values of the argument.

Due to the oscillatory behavior of the Bessel function $J_0(x)$, the bounce average operation acting on functions of $J_0(x)$ requires large resolutions in the coordinate along the trajectories of particles for large values of the argument. Writing explicitly

$$k_\perp \rho_s(\psi,\theta,\alpha,v,\lambda) = k_\psi |\nabla\psi| \frac{m_s v}{Z_s e} \sqrt{\frac{\lambda}{B(\psi,\theta,\alpha)}}, \tag{3.5}$$

it is clear that arbitrarily large values of the argument can be reached, especially for short wavelengths. This is because the integration over the total velocity v is defined in the range between 0 and ∞. Fortunately enough, this integration is weighted by a Maxwellian distribution function and, as we will see in the following subsections, these integrations converge in practice for values of v between 0 and $4\pi v_{ts}$. Note that, in equation (3.5), $k_\perp = k_\psi|\nabla\psi|$ where k_ψ is an input parameter and the quantity $|\nabla\psi| = |\nabla\psi|(\theta,\alpha)$ is obtained from the magnetic equilibrium.

In figure 3.5, we show a plot of the $\Gamma_0(x)$ function using logarithmic scales. As can be deduced from this figure, the integration of $\Gamma_0(x)$ (or combinations containing it) over the trajectories of particles is much less demanding than in the case of $J_0(x)$. This is because the $\Gamma_0(x)$ function does not show an oscillatory behavior. Note that, this function also exhibits a decay proportional to $1/\sqrt{x}$ at short wavelengths. In this case, the argument of the $\Gamma_0(x)$ function is given explicitly by

$$k_\perp^2 \rho_{ts}^2(\psi,\theta,\alpha) = k_\psi^2 |\nabla\psi|^2 \frac{m_s T_s(\psi)}{Z_s^2 e^2 B^2(\psi,\theta,\alpha)}. \tag{3.6}$$

For the implementation of the Bessel functions in CAS3D-K, we have used the numerical library GSL [50, 51] (GNU Scientific Library). In particular, for $J_0(x)$ we have used the function `gsl_sf_bessel_J0` with real argument and for $\Gamma_0(x)$ we have made use of the function `gsl_sf_bessel_I0_scaled`, also with real argument.

3.2.3 Finite orbit-width effects

The finite orbit-width effects are encoded in $\delta_s = \delta_s(\psi, \theta, \alpha, v, \lambda, \sigma)$. These effects account for the radial displacement of the particle's gyrocenter from their mean flux surface. In the equation for the residual level (2.57) these are contained in the complex exponentials $\exp(\pm i k_\psi \delta_s)$ and in the zonal-flow frequency (2.66) these are present in the term A_1. The expansion in power series of these complex exponentials can be found in Appendix B.

As already described in the previous chapter, the expression of δ_s is obtained as the solution of the magnetic differential equation (2.29). In general, this solution can be written as

$$\delta_s = -\frac{I_p}{\Psi_p'}\rho_{\|s} + \widetilde{\delta_s}, \tag{3.7}$$

where the first term on the right-hand side of this equation is the solution in axisymmetric devices and the second term is the non-axisymmetric contribution. Here, the parallel gyroradius is defined as $\rho_{\|s} := v_\|/\Omega_s$, or explicitly

$$\rho_\|(\psi, \theta, \alpha, v, \lambda, \sigma) = \frac{m_s v \sigma}{Z_s e}\frac{\sqrt{1 - \lambda B(\psi, \theta, \alpha)}}{B(\psi, \theta, \alpha)}. \tag{3.8}$$

A detailed derivation of the solution δ_s for both passing and trapped particles is given in Appendix A. The solution for passing particles is obtained throughout a Fourier method. For trapped particles, we describe two different methods; an integral method, and a solution in bounce harmonics. Although both methods give the same results, the integral method has proven to be much faster. We have implemented in CAS3D-K the full description of these expressions both for passing and trapped particles. These are explained next.

It is worth mentioning that due to the fact that δ_s is odd in $v_\|$, for trapped particles one obtains that $\overline{\delta_s} = 0$. Therefore, in the evaluation of the zonal-flow frequency (2.66), the term A_1 (see equation (2.63)) can be written as

$$A_1 = \sum_s \frac{Z_s^2}{T_s}\left[\left\{\overline{\delta_s^2} - \overline{\delta_s}^2\right\}_s^{\text{pass}} + \left\{\overline{\delta_s^2}\right\}_s^{\text{trap}}\right], \tag{3.9}$$

where the subscript "pass" and "trap" means that the integration is performed only for passing and trapped particles, respectively.

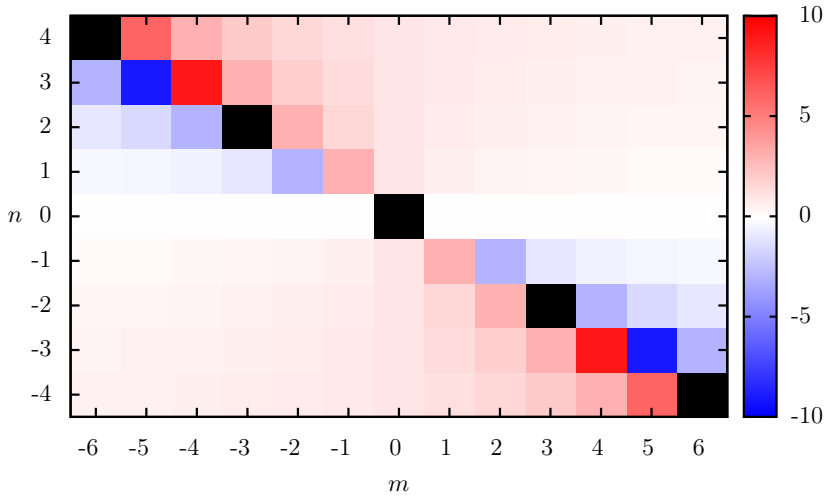

Figure 3.6: Plot of the term $qn/(m+qn)$ for a rational value $q = 3/2$ and modes $-6 < m < 6$ and $-4 < n < 4$. Note that the denominator vanishes for the modes satisfying $m/n = -q$. These cells are marked in black.

Passing particles

For passing particles, the non-axisymmetric contribution of δ_s can be written as (see Appendix A.1 for a detailed derivation)

$$\widetilde{\delta_s} = \left(\frac{I_p}{\Psi_p'} - \frac{I_t}{\Psi_t'}\right) \sum_{m,n\neq 0} \left(\frac{qn}{m+qn}\right) (\rho_{\|s})_{mn} \mathrm{e}^{2\pi \mathrm{i}(m\theta+n\zeta)}, \tag{3.10}$$

where we have used the expansion in Fourier series

$$\rho_{\|s} = \sum_{m,n} (\rho_{\|s})_{mn} \mathrm{e}^{2\pi \mathrm{i}(m\theta+n\zeta)}. \tag{3.11}$$

Here, n and m are the toroidal and poloidal mode numbers, respectively. Note that in equation (3.10), the mode $(m,n) = (0,0)$ is not included in the sum.

For the implementation in CAS3D-K of the full expression of $\widetilde{\delta_s}$, we calculate the Fourier amplitudes $(\rho_{\|s})_{mn}$ for $-N \leq n \leq N$ and $-M \leq m \leq M$, where N and M are the largest toroidal and poloidal mode numbers used to generate the equilibrium. These Fourier amplitudes are obtained as

$$(\rho_{\|s})_{m,n} = \int_0^1 \mathrm{d}\theta \int_0^1 \mathrm{d}\zeta \, \rho_{\|s} \, \mathrm{e}^{-2\pi \mathrm{i}(m\theta+n\zeta)}. \tag{3.12}$$

In the evaluation of equation (3.10), special care must be taken when calculating near rational surfaces where the required resolution is large. On rational surfaces the denominator of equation (3.11) vanishes. This occurs for m and n satisfying the condition $q = -m/n$, see for example figure 3.6, where the evaluation of the term $qn/(m + qn)$ on a rational surface with $q = 3/2$ is shown.

Trapped particles: Integral method

For trapped particles, the expression of δ_s using an integral method is given by equation (A.14). In that expression, $\widetilde{\delta}_s$ reads

$$\widetilde{\delta}_s = \int_0^{\tau} \widetilde{\omega}_{s\alpha} \mathrm{d}\tau', \tag{3.13}$$

where $\widetilde{\omega}_{s\alpha}$ is defined as

$$\widetilde{\omega}_{s\alpha} := \frac{qI_p - I_t}{\Psi_p'} \left[\tau_b^{-1} \partial_\alpha \rho_{\|s} - \overline{\tau_b^{-1} \partial_\alpha \rho_{\|s}} \right]. \tag{3.14}$$

Here, we have used that

$$\tau_b := \frac{B\sqrt{g}}{v_\| \Psi_p'}, \tag{3.15}$$

and the coordinate τ is given by

$$\tau := \begin{cases} \int_{\theta_{b_1}}^{\theta} |\tau_b| \, \mathrm{d}\theta' & \text{when} \quad \sigma > 0 \\ \int_{\theta_{b_1}}^{\theta_{b_2}} |\tau_b| \, \mathrm{d}\theta - \int_{\theta_{b_2}}^{\theta} |\tau_b| \, \mathrm{d}\theta' & \text{when} \quad \sigma < 0, \end{cases} \tag{3.16}$$

which is monotonic over the orbit, and θ_{b_1} and θ_{b_2} are the bounce points of the orbit; that is, the solutions for θ of the equation $1 - \lambda B(\psi, \theta, \alpha) = 0$.

For the calculation of equation (3.13) in CAS3D-K we have used the explicit form

$$\partial_\alpha \rho_{\|s} = \frac{m_s v \sigma}{Z_s e} \frac{(\lambda B - 2)}{2B^2 \sqrt{1 - \lambda B}} \partial_\alpha B. \tag{3.17}$$

This form requires the evaluation of the α-derivatives of the magnetic field. To perform these derivatives we use the method described in Section 3.2.1 for the linear five-point stencil in one dimension that we have implemented in CAS3D-K. Note that, as the derivative $\partial_\alpha B$ only depends on the spatial coordinates (θ, α), its evaluation is done only once for a given radial position. This represents a significant simplification in the evaluation of $\widetilde{\delta}_s$ compared to the method using bounce harmonics where its evaluation must be performed on every trajectory.

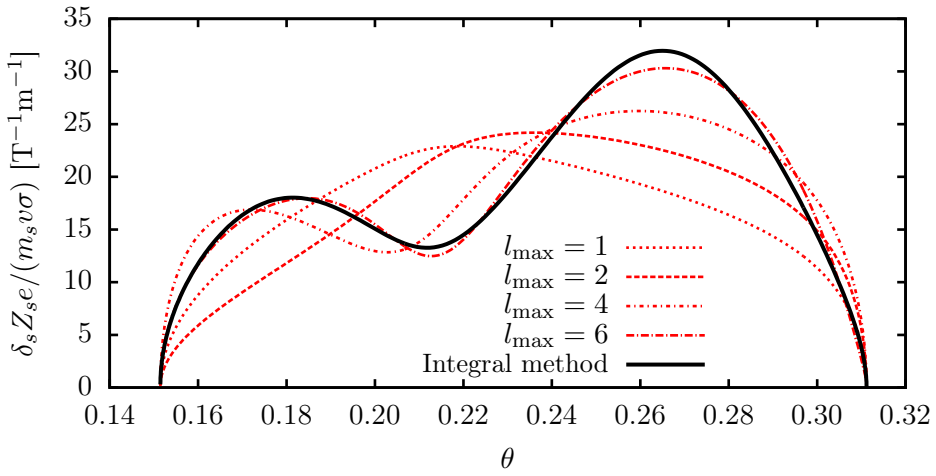

Figure 3.7: Example of δ_s (3.7) calculated in the standard configuration of the TJ-II stellarator for a trajectory with $\lambda = 1.012$ and $q = 0.628$ at a radial position $\psi = 0.5$ using two different methods; the integral method (3.13); and the one using expansions in bounce harmonics (3.18) for mode numbers up to $l_{\max} = 1$, 2, 4 and 6.

Trapped particles: Bounce harmonics method

For trapped particles, the solution using an expansion in bounce harmonics is described in Appendix A.2. This is given by equation (A.17), where

$$\widetilde{\delta_s} = 2 \sum_{l>0} \frac{(\omega_{s\alpha})_l}{l\,\widehat{\omega}_b} \sin\left(l\,\widehat{\omega}_b \tau\right). \tag{3.18}$$

Here, the amplitude of the bounce harmonics is given by

$$(\omega_{s\alpha})_l = (\widehat{\tau}_b/2)^{-1} \int_0^{\widehat{\tau}_b/2} \omega_{s\alpha}(\tau) \cos\left(l\widehat{\omega}_b \tau\right) \mathrm{d}\tau, \tag{3.19}$$

where

$$\omega_{s\alpha} = \frac{qI_p - I_t}{\tau_b \Psi_p'}\, \partial_\alpha \rho_{\|s}, \tag{3.20}$$

and we have used the definition $\widehat{\omega}_b := 2\pi/\widehat{\tau}_b$ with

$$\widehat{\tau}_b = 2 \int_{\theta_{b_1}}^{\theta_{b_2}} |\tau_b|\, \mathrm{d}\theta. \tag{3.21}$$

The implementation of equation (3.18) in CAS3D-K is done in several steps; first, we calculate $\widehat{\tau}_b$ on every trajectory; then, $(\omega_{s\alpha})_l$ is evaluated for

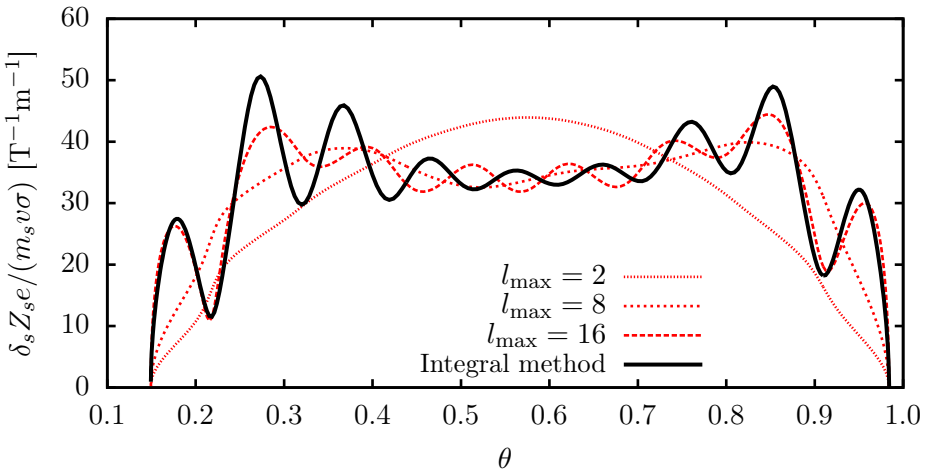

Figure 3.8: Plot of δ_s (3.7) calculated in the standard configuration of the TJ-II stellarator for a trajectory with $\lambda = 1.012$ and $q = 0.628$ at a radial position $\psi = 0.5$ using two different methods; the integral method (3.13); and the one using expansions in bounce harmonics (3.18) for mode numbers up to $l_{\max} = 2$, 8 and 16.

any given mode number l and τ along the trajectory; and, finally, we sum the terms given in (3.18) for the different values of l. The evaluation of $\widetilde{\delta_s}$ using this method requires several steps and these must be calculated for each trajectory, at every particle position and point in velocity space.

Although the integral method and the one using bounce harmonics give exactly the same results, the first method is preferred as it requires much less computational resources, is much simple to implement and less numerical errors are expected. The convergence in the calculation of δ_s using the bounce harmonics depends on the ripple of the device and on the length of a given trajectory. In general, devices with large ripple and long trajectories require larger mode numbers and consequently more resolution and computational resources. An example of the calculation of δ_s using bounce harmonics in a short trajectory, one that lives inside a field period, in the standard configuration of the TJ-II stellarator is given in Figure 3.7. In this case, the bounce harmonics method converges to the integral one for values of the mode number l calculated up to $l_{\max} = 8$. The convergence in longer trajectories requires larger mode numbers. This is clear from Figure 3.8 where the evaluation of δ_s in a trajectory of a trapped particle covering two magnetic field periods converges for mode numbers up to $l_{\max} \sim 24$.

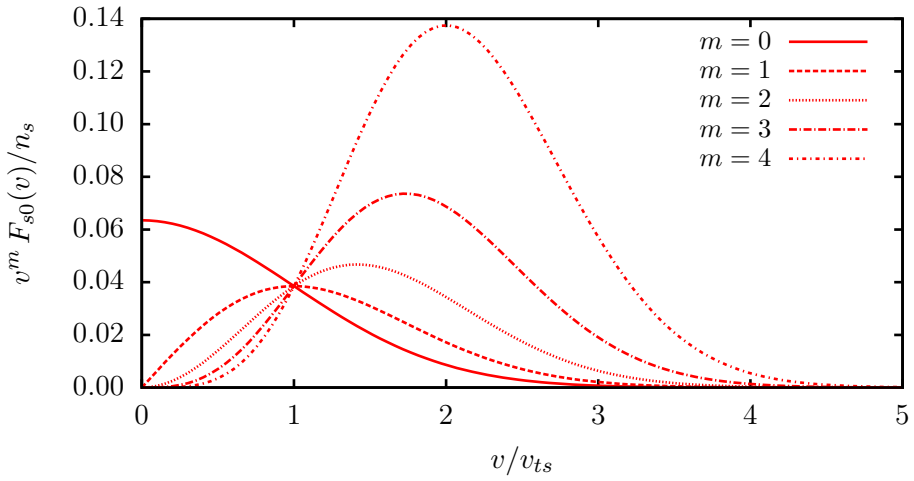

Figure 3.9: Integrand of the moments of the Maxwellian distribution function $F_{s0}(v)$ for several values of the exponent m.

3.2.4 Velocity space integrations

We have implemented in CAS3D-K the integration over the velocity coordinates v and $\sigma = \pm 1$, as given in equation 3.1. This equation can also be written in the simplified form

$$\left\{P\,\overline{Q}\right\}_s = \sum_{\sigma=-1}^{1} \int_0^{\infty} K(\psi, v, \sigma)\, F_{s0}(\psi, v)\, \mathrm{d}v, \tag{3.22}$$

where

$$K(\psi, v, \sigma) = \left\langle \int_0^{1/B} \mathrm{d}\lambda\, \frac{\pi v^2 B}{\sqrt{1-\lambda B}}\, P\,\overline{Q} \right\rangle_{\psi} \tag{3.23}$$

and the Maxwellian distribution reads

$$F_{s0}(\psi, v) = \frac{n_s(\psi)}{\left(\sqrt{2\pi} v_{ts}(\psi)\right)^3} \exp\left(-\frac{v^2}{2 v_{ts}^2(\psi)}\right). \tag{3.24}$$

For the integration over v, we use a linear scheme and we calculate for values in the range $0 \leq v \leq 4\pi v_{ts}$. This scheme allows the computation of any moment of the Maxwellian distribution function and the given range ensures enough accuracy in all the calculations shown in this thesis. For the resolution in v, we use values of $n_v = 64$ integration points and in some calculations this value can be increased up to 128.

In the evaluation of certain quantities, the integration over the total velocity can be performed analytically. For example in the evaluation of the

zonal-flow frequency, given by equation (2.66), where the integration of the terms (2.63) and (2.64) is simplified by using the moments of the distribution function

$$\int_0^\infty F_{s0}(\psi, v)\, v^2\, \mathrm{d}v = \frac{1}{4\pi} n_s, \tag{3.25}$$

$$\int_0^\infty F_{s0}(\psi, v)\, v^4\, \mathrm{d}v = \frac{3}{4\pi} n_s v_{ts}^2 \tag{3.26}$$

and

$$\int_0^\infty F_{s0}(\psi, v)\, v^6\, \mathrm{d}v = \frac{15}{4\pi} n_s v_{ts}^4. \tag{3.27}$$

We use the numerical evaluation of the first moments of the distribution function to check the accuracy of the numerical method implemented in CAS3D-K. Some of the arguments of these moments are shown in figure 3.9.

In general, the integration over σ must be computed numerically but an important simplification can be applied in the evaluation of equation 3.22 by knowing the symmetry properties of $K(\psi, v, \sigma)$ with respect to σ. Using these properties, it is easy to see that equation 3.22 vanishes if $K(\psi, v, \sigma) = -K(\psi, v, -\sigma)$ or it gives twice the value obtained when calculated with $\sigma = 1$ in case that $K(\psi, v, \sigma) = K(\psi, v, -\sigma)$.

3.2.5 Validation of the CAS3D-K calculations

In the following chapters we will use extensively the modifications included in CAS3D-K described in this chapter to accurately calculate quantities such as the residual zonal-flow level and the oscillation frequency in stellarators. The majority of the CAS3D-K calculations shown in this work are compared against analytical results, other numerical calculations available in the literature and the results obtained from independent calculations with two gyrokinetic codes, EUTERPE and GENE. We remind the reader that we will use the terminology "CAS3D-K", "extension to CAS3D-K" and "semianalytical method" interchangeably.

3.3 The EUTERPE code

EUTERPE [37, 38] is a global Particle-In-Cell (PIC) code for the simulation of plasmas in 3D geometry.

The code solves the gyroaveraged Vlasov equation for the gyrocentre distribution function $F_s = F_s(\mathbf{R}, v_\parallel, \mu, t)$ of up to three kinetic species (ions, electrons and/or a third species)

$$\frac{\partial F_s}{\partial t} + \frac{\mathrm{d}\mu}{\mathrm{d}t}\frac{\partial F_s}{\partial \mu} + \frac{\mathrm{d}v_\parallel}{\mathrm{d}t}\frac{\partial F_s}{\partial v_\parallel} + \frac{\mathrm{d}\mathbf{R}}{\mathrm{d}t}\cdot\frac{\partial F_s}{\partial \mathbf{R}} = C(F_s), \tag{3.28}$$

where $\mathbf{R}$ is the gyrocenter position, $v_\parallel$ is the parallel velocity, $\mu = v_\perp^2/(2B)$ is the magnetic moment and $C(F_s)$ is the collision operator. The gyrokinetic simulations considered in this thesis are collisionless, therefore we take $C(F_s) = 0$. Although the code can solve for electromagnetic perturbations, in this thesis we only deal with electrostatic perturbations. In this case, the equations of motion are

$$\begin{aligned}
\frac{\mathrm{d}\mathbf{R}}{\mathrm{d}t} =& v_\parallel \hat{\mathbf{b}} + \frac{\mu B + v_\parallel^2}{B_s^* \Omega_s}\, \hat{\mathbf{b}} \times \nabla B \\
&+ \frac{v_\parallel^2}{B_s^* \Omega_s} \left(\nabla \times B\right)_\perp - \frac{\nabla \langle \varphi \rangle}{B_s^*} \times \hat{\mathbf{b}}, \\
\frac{\mathrm{d}v_\parallel}{\mathrm{d}t} =& -\mu \left[\hat{\mathbf{b}} + \frac{v_\parallel^2}{B_s^* \Omega_s} \left(\nabla \times B\right)_\perp \right] \cdot \nabla B \\
&- \frac{Z_s e}{m_s} \left(\hat{\mathbf{b}} + \frac{v_\parallel^2}{B_s^* \Omega_s} \left[\hat{\mathbf{b}} \times \nabla B + \left(\nabla \times B\right)_\perp \right] \right) \cdot \nabla \langle \varphi \rangle , \\
\frac{\mathrm{d}\mu}{\mathrm{d}t} =& 0,
\end{aligned} \tag{3.29}$$

where we have used the definition[1]

$$B_s^* := B + \frac{m_s v_\parallel}{Z_s e} \hat{\mathbf{b}} \cdot \nabla \times \hat{\mathbf{b}}, \tag{3.30}$$

and $\langle \varphi \rangle$ is the gyroaveraged electrostatic potential.

In EUTERPE the so-called δf splitting is used and the 5D gyrocentre distribution function $F_s = F_s(\mathbf{R}, v_\parallel, \mu, t)$ is separated into a Maxwellian equilibrium part and a time-dependent perturbation

$$F_s(\mathbf{R}, v_\parallel, \mu, t) = F_{s0}(\mathbf{R}, v_\parallel, \mu) + F_{s1}(\mathbf{R}, v_\parallel, \mu, t). \tag{3.31}$$

The last term is usually written in the literature as δf. This approach allows to follow only the evolution of the perturbation δf, which has the advantage of reducing the numerical noise [52] and is computationally more efficient than following the full distribution function.

The distribution function F_{s1} is discretized using markers (or quasiparticles), each one contributing with a weight, as

$$F_{s1} = \sum_{p=1}^{N_p} w_p \delta^3(\mathbf{R} - \mathbf{R}_p) \delta(v_\parallel - v_{\parallel p}) \delta(\mu - \mu_p) / (2\pi B_s^*), \tag{3.32}$$

where N_p is the number of markers used in the simulation and $\mathbf{R}_p$, $v_{\parallel p}$, μ_p and w_p are the position, parallel velocity, magnetic moment and the weight

[1] In general, B_s^* can be approximated by $B_s^* \simeq B$.

assigned to the marker p, respectively. Using equations (3.32) and (3.31) in (3.28) an evolution equation for the weights can be obtained. The markers carry the charge and mass of each simulated species and are continuously evolved according to the equations (3.29) using cylindrical coordinates. Several integration schemes are implemented for the time integration of the equations of motion described by (3.29): a predictor-corrector and several fourth-order Runge-Kutta methods, including adaptive time step.

The equilibrium magnetic field, $\mathbf{B}$, and related quantities appearing in the equations of motion are calculated with VMEC and are mapped onto a grid in cylindrical coordinates through an intermediate code. The electrostatic potential φ is obtained from the quasineutrality equation which, assuming the long wavelength approximation $k_\perp \rho_s < 1$, reads

$$Z_i e \langle n_i \rangle - e n_e = -m_i \nabla \left(\frac{n_0}{B^2} \nabla_\perp \varphi \right), \tag{3.33}$$

where $\langle n_i \rangle$ is the gyroaveraged ion density, n_0 is the equilibrium density and n_e is the perturbed electron density. When the adiabatic-electron approximation is used the quasineutrality reads

$$Z_i e \langle n_i \rangle - e^2 n_0 \frac{\varphi - \langle \varphi \rangle_\psi}{T_e} = -m_i \nabla \left(\frac{n_0}{B^2} \nabla_\perp \varphi \right). \tag{3.34}$$

Here, $\langle \varphi \rangle_\psi$ is the potential averaged over a flux surface.

The quasineutrality equation is discretized using finite elements (B-splines) and the PETSc library is used for solving it. The potential can be filtered using squared and diagonal Fourier filters to reduce the noise.

Two coordinate systems are used in the code: cylindrical coordinates $\{R, Z, \phi_E\}$ are used for evolving the markers and the PEST-1 [53] $\{s_E, \theta_E, \phi_E\}$ system of magnetic coordinates is used for the fields, where s_E is the normalized toroidal flux and θ_E and ϕ_E are the poloidal and toroidal coordinates. This scheme requires to change between both coordinate systems, at every time step, which is facilitated by having the common toroidal coordinate ϕ_E.

Equation (3.28) is non-linear in general, but a linearized equation for F_{s1} can be written as

$$\begin{aligned} &\frac{\partial F_{s1}}{\partial t} + \left[v_\parallel \hat{\mathbf{b}} + \frac{\mu B + v_\parallel^2}{B_s^* \Omega_s} \hat{\mathbf{b}} \times \nabla B + \frac{v_\parallel^2}{B_s^* \Omega_s} (\nabla \times B)_\perp \right] \cdot \frac{\partial F_{s1}}{\partial \mathbf{R}} \\ &\quad - \mu \left[\hat{\mathbf{b}} + \frac{v_\parallel^2}{B_s^* \Omega_s} (\nabla \times B)_\perp \right] \cdot \nabla B \frac{\partial F_{s1}}{\partial v_\parallel} = \frac{\nabla \langle \varphi \rangle}{B_s^*} \times \hat{\mathbf{b}} \cdot \frac{\partial F_{s0}}{\partial \mathbf{R}} \\ &\quad + \frac{Z_s e}{m_s} \left(\hat{\mathbf{b}} + \frac{v_\parallel^2}{B_s^* \Omega_s} \left[\hat{\mathbf{b}} \times \nabla B + (\nabla \times B)_\perp \right] \right) \cdot \nabla \langle \varphi \rangle \frac{\partial F_{s0}}{\partial v_\parallel}. \end{aligned} \tag{3.35}$$

The simulations with EUTERPE shown in this thesis are linear and collisionless with either a plasma composed of fully kinetic ions and electrons or

one that consists of singly charged ions where the approximation of adiabatic electrons is used.

The code is written in FORTRAN and parallelized using MPI. The physical domain is divided into toroidal slices, each one managed by a processing unit. More information about the code can be found in References [37, 38, 54, 55, 56, 57].

3.4 The GENE code

GENE [15, 39, 40, 41] is a Eulerian electromagnetic gyrokinetic turbulence code. The code can use adiabatic electrons or fully kinetic species and is able to run linear and non-linear simulations including an arbitrary number of kinetic species.

The gyroaveraged Vlasov equation (3.28) for the distribution function is solved on a fixed grid in field aligned coordinates $\{x, y, z\}$, where x is the radial coordinate, z is the coordinate along the field line and the coordinates $\{y, z\}$ are used to describe a full flux surface (y is the coordinate along the binormal direction). The independent velocity coordinates are $\{v_\parallel, \mu\}$. The partial differential equation (3.28) is converted into an ordinary differential equation by discretizing the spatial derivatives of the distribution function by means of finite differences. Then, the resulting time evolution equation is evolved by using an explicit Runge-Kutta integration scheme.

GENE is able to deal with tokamak and stellarator geometries and it can be run in radially global, full flux surface or flux tube simulation domains by using specific boundary conditions in each case. Depending on the case the spatial coordinates are treated differently. Finite differences are always used in the z coordinate, and the code is always spectral in the y direction. In the flux-tube and full flux surface simulations it is spectral in the x and y directions, while in the radially global version the code is only spectral in y direction.

In the most general electromagnetic case, the equations of motion appearing in (3.28) are[2]:

$$\begin{aligned}
\frac{\mathrm{d}\mathbf{R}}{\mathrm{d}t} &= v_\parallel \hat{\mathbf{b}}_0 + \frac{B_0}{B^*_{0s\parallel}} \left(\mathbf{v}_{E\times B} + \mathbf{v}_{\nabla B_0} + \mathbf{v}_c\right) \\
\frac{\mathrm{d}v_\parallel}{\mathrm{d}t} &= -\frac{1}{m_s v_\parallel} \frac{\mathrm{d}\mathbf{R}}{\mathrm{d}t} \cdot \left[Z_s e \left\langle \mathbf{E}_1 \right\rangle - \mu \nabla \left(B_0 + \left\langle B_{1\parallel} \right\rangle\right)\right], \\
\frac{\mathrm{d}\mu}{\mathrm{d}t} &= 0.
\end{aligned} \tag{3.36}$$

[2]We follow the notation commonly used in the literature describing the GENE code. For this purpose, we use cgs units solely in this section.

where we have used the definitions for the drift velocities

$$\mathbf{v}_{E\times B} = -\frac{c}{B_0^2}\nabla\chi_1 \times \mathbf{B}_0, \tag{3.37}$$

$$\mathbf{v}_{\nabla B_0} = \frac{\mu}{m_s\Omega_s^*}\mathbf{b}_0 \times \nabla B_0, \tag{3.38}$$

$$\mathbf{v}_c = \frac{v_\parallel^2}{\Omega_s^*}\left(\nabla \times \hat{\mathbf{b}}_0\right)_\perp. \tag{3.39}$$

Here, c is the speed of light in vacuum, $\Omega_s^* = Z_s eB/(m_s c)$ is the gyrofrequency in cgs units, $\hat{\mathbf{b}}_0 = \mathbf{B}_0/B_0$ is the unit vector in the direction of the equilibrium magnetic field $\mathbf{B}_0$, $B_{0s\parallel}^* = \hat{\mathbf{b}}_0 \cdot \mathbf{B}_{0s}^*$ is approximated by $B_{0s\parallel}^* \simeq B_{0s}^*$, where

$$\mathbf{B}_{0s}^* = \mathbf{B}_0 + \nabla \times \left(\frac{\mathbf{B}_0 v_\parallel}{\Omega_s^*}\right), \tag{3.40}$$

$B_{1\parallel}$ is the parallel component of the magnetic field perturbation, $\langle \mathbf{E}_1 \rangle$ is the gyroaverage of the fluctuating part of the electric field, which is defined as

$$\langle \mathbf{E}_1 \rangle := -\nabla\langle\varphi_1\rangle - \hat{\mathbf{b}}_0 \frac{1}{c}\frac{\mathrm{d}\langle A_{1\parallel}\rangle}{\mathrm{d}t}, \tag{3.41}$$

the gyroaveraged modified potential is defined as

$$\langle\chi_1\rangle := \langle\varphi_1\rangle - \frac{v_\parallel}{c}\langle A_{1\parallel}\rangle - \frac{\mu}{c}\langle B_{1\parallel}\rangle \tag{3.42}$$

and φ_1 and $A_{1\parallel}$ are the fluctuating parts of the electrostatic potential and the parallel component of the magnetic potential, respectively.

GENE also uses a δf approximation in the distribution function. Using the decomposition given in (3.31), the linearized Vlasov equation without considering collisions reads

$$\begin{aligned}
&\frac{\partial g_{1s}}{\partial t} + \frac{B_0}{B_{0s\parallel}^*}\mathbf{v}_{E\times B}\cdot\left(\nabla F_{s0} + \frac{\mu}{m_s v_\parallel}\nabla B_0 \frac{\partial F_{s0}}{\partial v_\parallel}\right) \\
&\quad + \frac{B_0}{B_{0s\parallel}^*}\left(\mathbf{v}_{E\times B} + \mathbf{v}_{\nabla B_0} + \mathbf{v}_c\right)\cdot\nabla G_{1s} + v_\parallel \mathbf{b}_0 \cdot \nabla G_{1s} \\
&\quad + \frac{1}{m_s v_\parallel}\left(v_\parallel \mathbf{b}_0 + \frac{B_0}{B_{0s\parallel}^*}\mathbf{v}_c\right)\cdot\left[Z_s e\left\langle \mathbf{E}_1\right\rangle - \mu\nabla\left(B_0 + \left\langle B_{1\parallel}\right\rangle\right)\right]\frac{\partial F_{s1}}{\partial v_\parallel} = 0,
\end{aligned} \tag{3.43}$$

where we have used the definitions

$$g_{1s} := F_{s1} - \frac{Z_s e}{m_s c}\langle A_{1\parallel}\rangle \frac{\partial F_{s0}}{\partial v_\parallel} \tag{3.44}$$

and

$$G_{1s} := g_{s1} - \frac{Z_s e}{m_s v_\parallel}\chi_1 \frac{\partial F_{s0}}{\partial v_\parallel}. \tag{3.45}$$

Note that, as in this work we only deal with electrostatic perturbations, the equation which is actually solved in this case is largely simplified, by setting $A_{1||} = 0$ and $B_{1||} = 0$ in (3.41), (3.42), (3.43) and (3.44).

The solution to the Vlasov equation is obtained from the closure condition for the fields φ_1 and $A_{1\parallel}$ given by the quasineutrality equation and the Ampère's law. The quasineutrality equation reads

$$\begin{aligned}\sum_s \frac{Z_s^2 e}{T_s}\left(1-\Gamma_0\left(k_\perp^2\rho_{ts}^2\right)\right)\varphi_1 = \\ \sum_s Z_s\left[\Gamma_0\left(k_\perp^2\rho_{ts}^2\right)-\Gamma_1\left(k_\perp^2\rho_{ts}^2\right)\right]\frac{B_{1\parallel}}{B_0} \\ +\sum_s Z_s\frac{2\pi B_0}{m_s n_0}\int J_0(k_\perp\rho_s)F_{s1}\mathrm{d}v_\parallel\mathrm{d}\mu,\end{aligned} \tag{3.46}$$

where n_0 is the equilibrium density and we have used the definition

$$\Gamma_n\left(k_\perp^2\rho_{ts}^2\right) := I_n\left(k_\perp^2\rho_{ts}^2\right)\exp\left(-k_\perp^2\rho_{ts}^2\right), \tag{3.47}$$

where $I_n\left(k_\perp^2\rho_{ts}^2\right)$ is the modified Bessel function of the fist kind for integer values of n. The Ampère's law reads

$$\nabla_\perp^2 A_{1\parallel} = -\frac{8\pi^2 B_0}{c}\sum_s \frac{Z_s e}{m_s}\int v_\parallel J_0(k_\perp\rho_s)F_{s1}\mathrm{d}v_\parallel\mathrm{d}\mu. \tag{3.48}$$

These equations are solved without assumptions about the radial wavelength of the perturbation. For the electrostatic case, only the quasineutrality is required.

The numerical noise in GENE, mainly generated from the diffusive terms of the Vlasov equation, is controlled by the so-called hyper-diffusion term [58]. This artificial noise control method minimizes the unphysical effects obtained from the discretization schemes.

The code can take VMEC equilibria as input, which is transformed to GENE coordinates with the GIST [41] code package, and analytical equilibria using Miller indices. Other geometry interfaces are also available.

More details about the code GENE can be found in References [15, 39, 40, 41, 58, 59].

The GENE simulations shown in this thesis are linear and collisionless and have been performed both using fully kinetic species and also using the adiabatic electron approximation. For the simulations in tokamak geometry the flux tube version of the code was used. These simulations are basically 1D in space. In stellarators, the full flux surface version was used.

Chapter 4

Residual zonal flows in tokamaks and stellarators at arbitrary wavelengths

In Chapter 2 we derived expressions for the residual value in tokamak and stellarator geometries and for arbitrary wavelengths. The expression for fully kinetic species is given by (2.57), and by (2.59) when using the approximation of adiabatic electrons. In this chapter, we evaluate these expressions with our semianalytical method and we compare the results against those obtained from two gyrokinetic codes. The results shown in this chapter were published in [19].

We start in Section 4.1 by comparing CAS3D-K calculations of the residual level against analytical results from [6, 14], obtained in simplified tokamak geometry. We note that the results shown in these references were not derived as an initial value problem, but as the stationary solution of a forced system. We explain this in more detail in Section 4.3. In Section 4.2 our results are compared with those obtained with GENE and EUTERPE. We also compare the differences in computational time required by each approach showing that the semianalytical method is faster than the gyrokinetic simulations. Stellarator residual values are calculated for a range of wavelengths much wider than previously available in the literature. We comment on a purely stellarator effect already predicted in [7, 11]; namely, that the approximation of adiabatic electrons is always incorrect (even at long wavelengths) for the purpose of determining the residual zonal flow in stellarators. We quantify the error by computing, with CAS3D-K, the residual value when kinetic or adiabatic electrons are used. This result is confirmed by gyrokinetic simulations. We devote Section 4.3 to discuss the problem of a forced system that has become popular in the literature that is different from the initial value problem described in Section 4.2. A summary of the results in this chapter is presented in Section 4.4.

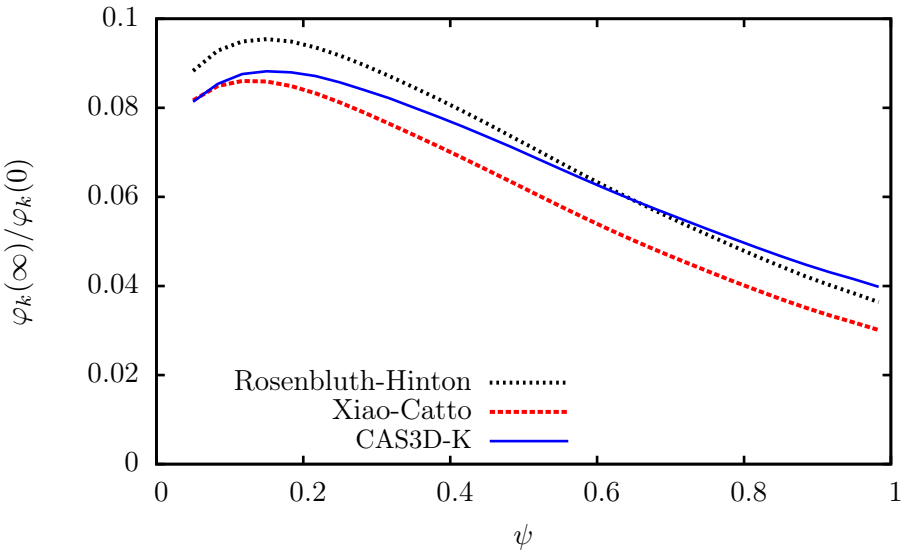

Figure 4.1: Radial dependence of the residual level given by (4.1), by (4.2), and by the evaluation of (2.59) with CAS3D-K in the long-wavelength limit. A tokamak with major radius $R = 1.7$ m, minor radius $a = 0.4$ m, and q profile given in figure 4.2 has been used.

4.1 Benchmark of CAS3D-K with previous results in simplified tokamak geometry

As a first check, we compare the results obtained with CAS3D-K against a well known analytical result. In reference [4], Rosenbluth and Hinton (R-H) calculated the residual level in large aspect ratio tokamaks with circular cross section and adiabatic electrons, in the limit $k_\perp \rho_{ti} \ll 1$. Denote the safety factor by q and the inverse aspect ratio by $\varepsilon = (a/R)\sqrt{\psi}$, where a is the minor radius and R is the major radius. The result obtained in [4] is

$$\frac{\varphi_k(\infty)}{\varphi_k(0)} = \frac{1}{1 + 1.6\, q^2 \varepsilon^{-1/2}}\,. \tag{4.1}$$

In reference [14], Xiao and Catto gave an expression more accurate in the inverse aspect ratio expansion. Namely,

$$\frac{\varphi_k(\infty)}{\varphi_k(0)} = \frac{1}{1 + 1.6 q^2 \varepsilon^{-1/2} + 0.5 q^2 + 0.36 q^2 \varepsilon^{1/2}}\,. \tag{4.2}$$

Both of these results were obtained by using the analytical equilibrium of a large aspect ratio circular tokamak which, in our coordinates, is given by

$$B = \frac{B_0}{1 + \varepsilon \cos(2\pi\theta)}, \tag{4.3}$$

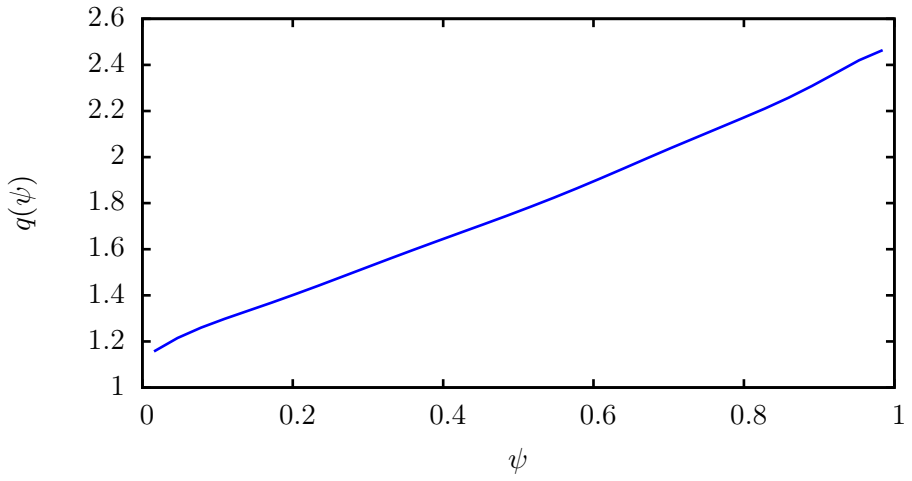

Figure 4.2: Safety factor profile of the tokamak employed for the calculations of Section 4.1.

where B_0 is the magnetic field strength at the magnetic axis. The analytical solutions (4.1) and (4.2) are plotted in figure 4.1, together with the numerical evaluation of (2.57) with CAS3D-K, for $k_\perp \rho_{ti} \ll 1$ and a Maxwellian initial condition. We use an axisymmetric tokamak with major radius $R = 1.7$ m, minor radius $a = 0.4$ m, and q profile given in figure 4.2. For the CAS3D-K computations, the equilibrium is obtained with VMEC employing the aspect ratio and safety factor values just mentioned. We also take a plasma consisting of singly charged ions and electrons, and assume flat density and temperature profiles with the same values for both species. The wavenumber used in the CAS3D-K calculation is $k_\psi = 0.5$ and the dimensionless quantity $\langle k_\perp \rho_{ti} \rangle_\psi$ ranges from 0.0015 in the innermost radial position to 0.0068 in the outermost one. We have checked that the residual zonal flow value obtained with CAS3D-K and shown in figure 4.1 does not change if $\langle k_\perp \rho_{ti} \rangle_\psi$ is further decreased. The regions of figure 4.1 where the curves agree and where the curves differ are as expected (see the remarks in [60] about figure 3(a) in that reference). The analytical equilibrium of a large aspect ratio circular tokamak, used in deriving the equations (4.1) and (4.2), differs less from the numerical equilibrium obtained with VMEC in radial positions closer to the center. We will see in Section 4.2 that the CAS3D-K results coincide with gyrokinetic simulations of zonal flow evolution, in which VMEC equilibria are also used.

Now, we turn our attention to compare CAS3D-K calculations with other numerical calculations. Xiao and Catto (X-C) also addressed in references [6, 14] the extension of the calculation in [4] to short wavelengths. They gave

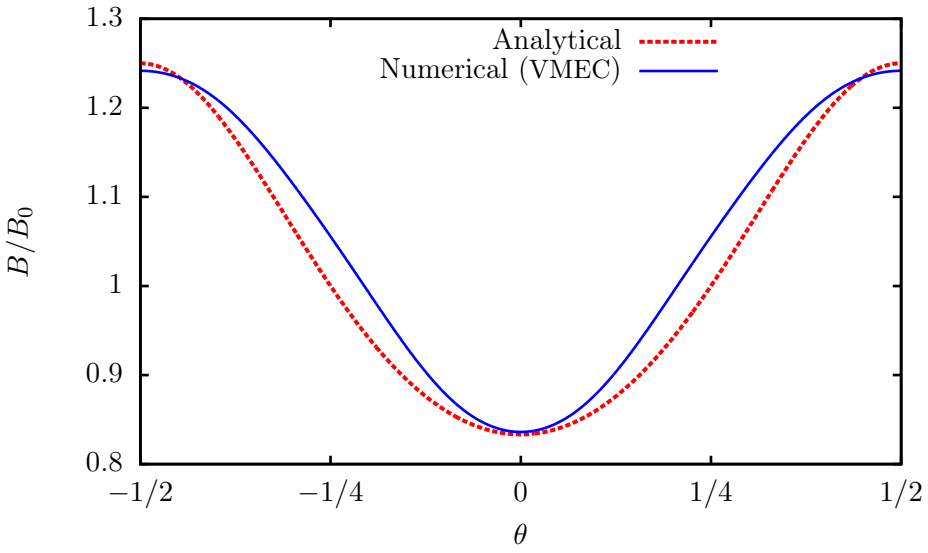

Figure 4.3: Magnetic field strength along a field line of the analytical large aspect ratio circular tokamak equilibrium, given by equation (4.3), with $\varepsilon = 0.2$, and for the numerical equilibrium obtained with VMEC (with $R = 1.7$ m, $a = 0.4$ m) at $\psi = 0.7$.

the result

$$\frac{\varphi_k(\infty)}{\varphi_k(0)} = \frac{\sum_s \frac{Z_s^2}{T_s} \left\{1 - J_{0s}^2\right\}_s}{\sum_s \frac{Z_s^2}{T_s} \left\{1 - \mathrm{e}^{-\mathrm{i}k_\psi \delta_s} J_{0s} \overline{\mathrm{e}^{\mathrm{i}k_\psi \delta_s} J_{0s}}\right\}_s} \tag{4.4}$$

for the residual zonal flow in a tokamak at arbitrary wavelengths and with kinetic electrons. The expression provided by X-C for the case of adiabatic electrons is

$$\frac{\varphi_k(\infty)}{\varphi_k(0)} = \frac{\sum_{s\neq e} \frac{Z_s^2}{T_s} \left\{1 - J_{0s}^2\right\}_s}{\sum_{s\neq e} \frac{Z_s^2}{T_s} \left\{1 - \mathrm{e}^{-\mathrm{i}k_\psi \delta_s} J_{0s} \overline{\mathrm{e}^{\mathrm{i}k_\psi \delta_s} J_{0s}}\right\}_s}. \tag{4.5}$$

In order to avoid any confusion, we have to point out that (4.4) and (4.5) were not derived as the solution of the initial value problem explained in Chapter 2, but assuming that the quasineutrality equation is forced with a source term. The argument of X-C can be streamlined as follows. Go back to equation (2.46) for the tokamak case (that is, $\overline{\omega_s} = 0$ for all particles). X-C consider that finite orbit width effects do not affect the initial condition;

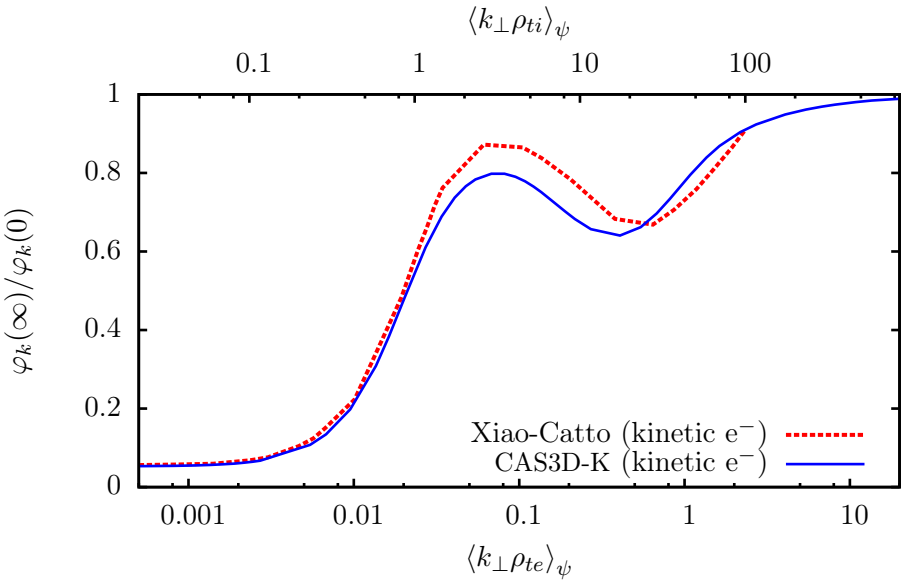

Figure 4.4: Comparison of the result in references [6, 14] and the evaluation of (4.4) with CAS3D-K. The parameters of the tokamak are the same as in figure 4.1.

i.e.

$$\sum_s Z_s \left\{ \mathrm{e}^{-\mathrm{i}k_\psi \delta_s} J_{0s} \overline{\mathrm{e}^{\mathrm{i}k_\psi \delta_s} f_s(0)/F_{s0}} \right\}_s = \sum_s Z_s \left\{ J_{0s} f_s(0)/F_{s0} \right\}_s = \left\langle \sum_s Z_s \int J_{0s} f_s(0) \mathrm{d}^3 v \right\rangle_\psi . \tag{4.6}$$

Hence, in this approximation, (2.57) gives

$$\varphi_k(\infty) \approx \frac{\left\langle \sum_s Z_s \int J_{0s} f_s(0) \mathrm{d}^3 v \right\rangle_\psi}{\sum_s \frac{Z_s^2 e}{T_s} \left[\{1\}_s - \left\{ \mathrm{e}^{-\mathrm{i}k_\psi \delta_s} J_{0s} \overline{\mathrm{e}^{\mathrm{i}k_\psi \delta_s} J_{0s}} \right\}_s^{\overline{\omega_s}=0} \right]} . \tag{4.7}$$

The quasineutrality equation at $t = 0$, (2.52), can be trivially rewritten as

$$\varphi_k(0) = \left(\sum_s \frac{Z_s^2 e}{T_s} \{1 - J_{0s}^2\}_s \right)^{-1} \left\langle \sum_s Z_s \int J_{0s} f_s(0) \mathrm{d}^3 v \right\rangle_\psi . \tag{4.8}$$

From the quotient of (4.7) and (4.8), one obtains equation (4.4). Analogously, one can obtain (4.5) from (2.58). From these manipulations, it is clear that in the X-C calculation the charge perturbation at $t = 0$ can be viewed as a constant source term in the quasineutrality equation.

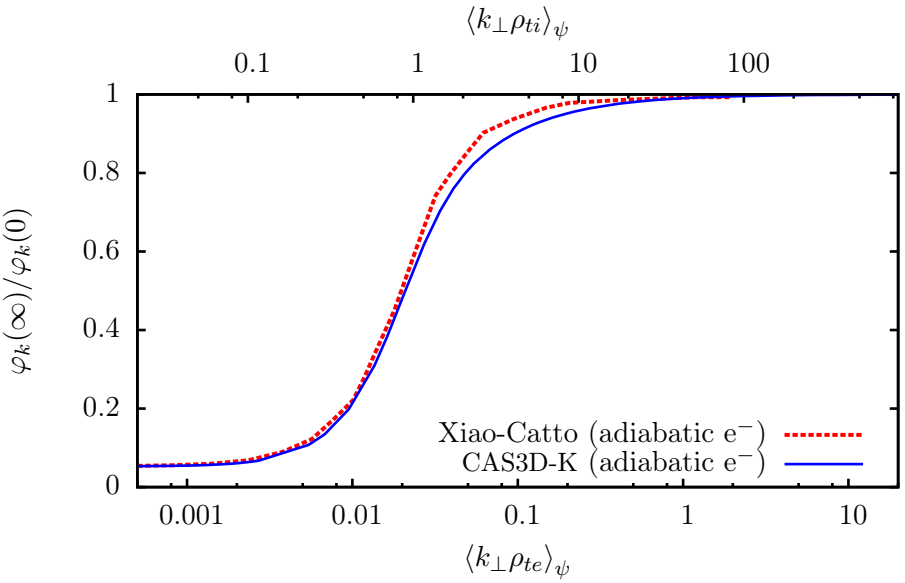

Figure 4.5: Comparison of the result in reference [14] for adiabatic electrons and the evaluation of equation (4.5) with CAS3D-K. The parameters of the tokamak are the same as in figure 4.1.

References [14] and [6] provided analytical evaluations of the right sides of (4.4) and (4.5) for simplified tokamak geometries. Since we can directly evaluate the right sides of (4.4) and (4.5) with CAS3D-K, we will compare the results as an additional check of our numerical tool.

In [6, 14], the analytical equilibrium of a circular cross section, large aspect ratio tokamak with safety factor $q = 2$ and inverse aspect ratio $\varepsilon = 0.2$ was used. For the calculations with CAS3D-K, we employ the VMEC tokamak equilibrium described above, which has similar parameters at $\psi = 0.7$. At this radial position, the VMEC equilibrium satisfies $q = 2$ and $\varepsilon = 0.2$ within an error of 1.5% ($\varepsilon = 0.197$ and $q = 2.03$). The difference between the VMEC equilibrium and the analytical one is illustrated in figure 4.3, where we compare the magnetic field strength along a field line for both equilibria. In the VMEC equilibrium, the value of the magnetic field strength at the magnetic axis is $B_0 = 1.87$ T. In general, deviations from circularity are expected in the numerical equilibrium because of effects like the Shafranov shift that are not taken into account in the analytical equilibrium. These deviations are smaller for radial positions closer to the center. The comparisons for the cases with fully kinetic species (4.4) and with adiabatic electrons (4.5) are shown in figures 4.4 and 4.5. The agreement is quite good. The fact that the curves present some differences, especially at short wavelengths, is not surprising because the equilibria are not exactly identical.

Note that the Xiao and Catto formulas (4.4) and (4.5) can be obtained

from an initial value problem calculation by choosing an initial condition $f_s(0)$ different from ours. However, the initial conditions that recover the X-C results necessarily have increasingly fast oscillations along the orbit for increasing k_ψ, and seem of limited interest for the analysis of turbulence simulations. For this reason, we choose the initial condition (2.56) that is in our opinion more relevant.

4.2 Residual zonal-flow obtained with CAS3D-K and gyrokinetic simulations

In this section, we calculate the residual zonal flow as an initial value problem for a wide range of radial wavelengths in tokamak and stellarator geometries with CAS3D-K. These calculations will be compared with the results from GENE and EUTERPE.

EUTERPE simulations are initiated with a zonal potential perturbation, which is produced by taking a perturbed distribution function

$$F_{s1}(0) = \epsilon \frac{Z_s e}{T_s} \left\langle k_\perp^2 \rho_{ts}^2 \right\rangle_\psi \varphi_k(0) \sin(k_\psi \psi)\, F_{s0}. \tag{4.9}$$

Here, F_{s0} is a Maxwellian distribution and ϵ is a small factor (on the order of 10^{-3}) that makes the perturbation to the distribution function, F_{s1}, much smaller than the equilibrium distribution, F_{s0}. After the fist time step, a zonal perturbation to the potential with the same radial dependence $\varphi(0) \propto \sin(k_\psi \psi)$ appears, that is used as the initial zonal-flow.

In EUTERPE, a long-wavelength approximation is used in the quasineutrality equation. Namely, the $\Gamma_0(x) = \exp(-x)\, I_0(x)$ function is approximated as $\Gamma_0(x) \approx 1 - x$, with $x = k_\perp^2 \rho_{ti}^2$, which is valid for $k_\perp \rho_{ti} \ll 1$. The initial condition (4.9) is a good approximation of (2.56) under these conditions (see Appendix B).

With the initial condition (4.9), the collisionless simulation is linearly evolved, retaining just a few (5 to 10) toroidal and poloidal Fourier modes of the potential. The $(m, n) = (0, 0)$ mode, which we can identify with φ_k in equation (2.19), is the dominant component of the potential spectrum during the simulation, thus proving that the assumption of an eikonal form in equation (2.19) is appropriate. Here, m and n label poloidal and toroidal modes, respectively. The time evolution of φ_k at a number of radial positions is tracked.

In the GENE simulations, we calculate the zonal-flow response for a wide range of radial wavelengths, using both adiabatic and kinetic electrons. We use the flux tube version of the code in tokamak geometry and the full flux surface version in stellarators. The distribution function is initiated according to (2.56). Since GENE works in Fourier space for the radial coordinate,

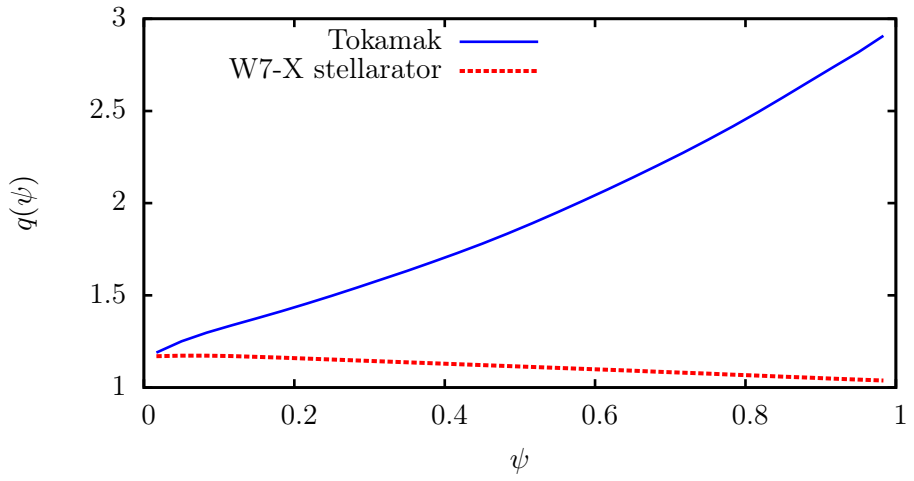

Figure 4.6: Safety factor profiles employed in Section 4.2 for the tokamak (solid line) and W7-X (dashed line) calculations.

we initialize the perturbed distribution function with only one radial mode which produces a potential with a single mode of unit amplitude.

To obtain the residual zonal-flow level and the oscillation frequency, the time trace of the zonal potential, or its radial derivative[1] (normalized to its initial value), is fitted to a model function with the form

$$\frac{\varphi_k'(t)}{\varphi_k'(0)} = A_{\mathrm{ZF}} \cos(\Omega_{\mathrm{ZF}} t) \exp\left(-\gamma_{\mathrm{ZF}} t\right) + R_{\mathrm{ZF}} + \frac{c_1}{1 + c_2 t^{c_3}}, \tag{4.10}$$

where R_{ZF} is the residual level, Ω_{ZF} is the zonal-flow oscillation frequency, A_{ZF} is the amplitude of the oscillation, γ_{ZF} is the damping rate, and $'$ means derivative with respect to the radial coordinate (normalized toroidal flux in EUTERPE). The last term in equation (4.10) accounts for the decay to the zonal-flow residual level, to which the oscillations are superimposed, and is described using the parameters c_1, c_2 and c_3. This term is important for cases in which the decay to this residual level is slow. The fit is performed with the non-linear fitting routine *fit* of the MATLAB software package. Note that, in principle, a similar value of the zonal-flow frequency could be obtained from a Fast Fourier Transform (FFT) of the time signal, but this method shows to be less precise in practice.

There are sources of error and uncertainty in the residual level and the oscillation frequency obtained by this procedure, related to the simulation itself and the approximations in the gyrokinetic code, and also associated to the fitting process.

[1] Assuming the eikonal form of the potential in equation (2.19), both the normalized potential and its radial derivative have a similar time evolution.

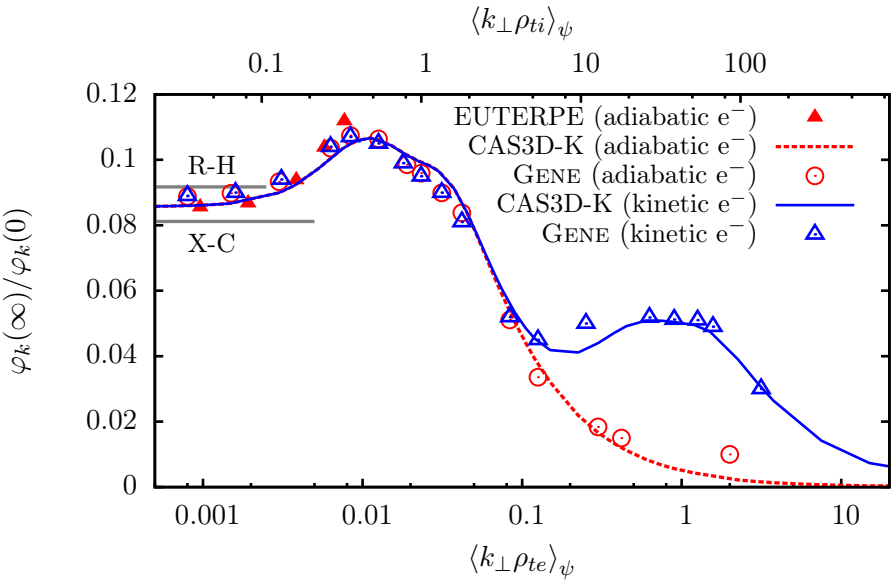

Figure 4.7: Residual zonal flow for the initial value problem in an axisymmetric large aspect ratio tokamak with major radius $R = 0.95$ m, minor radius $a = 0.25$ m and q profile given in figure 4.6. The values predicted by R-H and X-C (equations (4.1) and (4.2), respectively) are also shown for comparison.

In the CAS3D-K calculations shown in this chapter we have used the solution of δ_s for trapped particles with the expansion in bounce harmonics (3.18) instead of the integral method (3.13), the reason being that the latter was still not included in the code when the calculations in this chapter were performed. Although both methods give exactly the same value, the integral method requires less computational resources. In tokamaks, as only a small number of mode numbers are required for the description of the magnetic field, the differences in computational time by using (3.13) or (3.18) are not significant. This does not apply in stellarators as only passing particles contribute to the residual level.

In all the calculations shown in this chapter, we use flat density and temperature profiles with equal values for all species and we use the same VMEC equilibrium input for all the codes.

4.2.1 Tokamak

First, we compare gyrokinetic simulations and CAS3D-K calculations in tokamak geometry. We use an axisymmetric device with major radius $R = 0.95$ m, minor radius $a = 0.25$ m, and q profile given in figure 4.6, whose equilibrium is determined by VMEC. We use flat temperature profiles with $T_i = T_e$. The residual levels obtained with EUTERPE, CAS3D-K and the flux

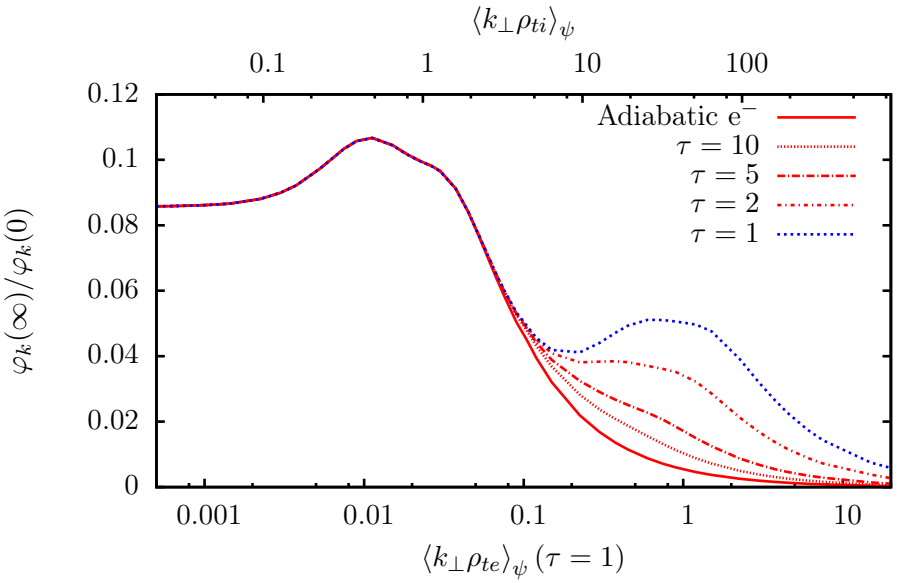

Figure 4.8: The same evaluation with CAS3D-K of equation (2.59) as in figure 4.7, with the adiabatic electron approximation, and the evaluation of equation (2.57) with fully kinetic species for different values of τ.

tube version of GENE are shown in figure 4.7 for a radial position $\psi = 0.25$. We show the calculations with fully kinetic species and also using the approximation of adiabatic electrons. The results of the gyrokinetic codes have been obtained fitting the temporal evolution of the potential to the model function (4.10). The results with CAS3D-K correspond to the evaluation of the equations (2.57) and (2.59). From figure 4.7, we can see that the agreement among the results of CAS3D-K, EUTERPE and GENE is excellent. When evaluating the residual level with gyrokinetic codes, a certain variability in the results must be assumed. This variability comes from the fitting method (smaller than 1%), the discretization in phase-space and the control of the numerical noise, among other factors. All the results in this work obtained with GENE show variations smaller than 10%. In any case, figure 4.7 shows that the residual level obtained by the three independent methods coincides within a margin smaller than this quantity, which gives us confidence to consider that the overall error is quite small.

As can be seen in figure 4.7, the residual value has local maxima centered at the scales of the electron and ion Larmor radii. In the long-wavelength limit, $k_\perp \rho_{ti} \ll 1$, the residual level in a tokamak does not depend on $k_\perp$. Its value is well predicted by (4.1), and even more accurately by (4.2), for a large aspect ratio tokamak with circular cross section. For the VMEC equilibrium used here, these predictions (also indicated in figure 4.7) are not so accurate for the reasons discussed in the paragraph below equation (4.2).

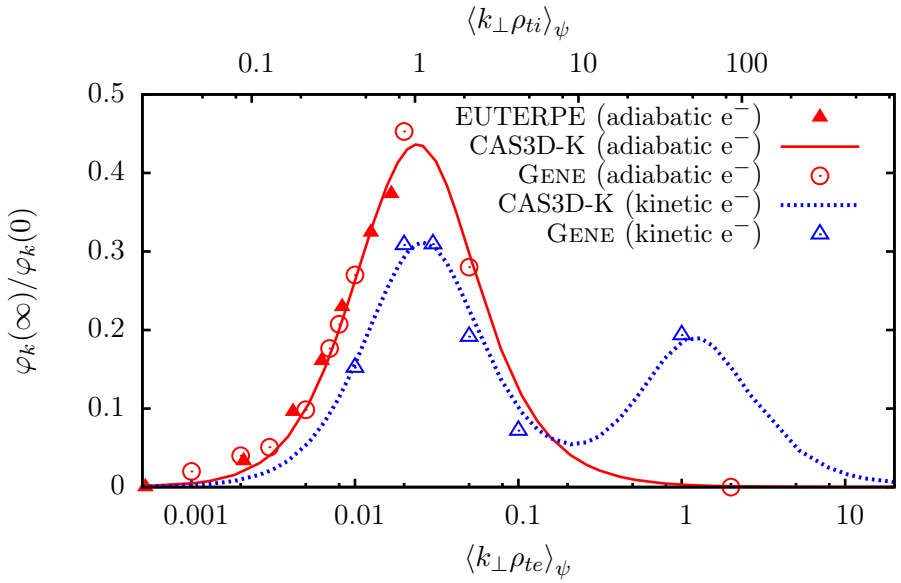

Figure 4.9: Residual zonal flow level for the initial value problem in the standard configuration of the W7-X stellarator at $\psi = 0.25$. The q profile is shown in figure 4.6.

At very short wavelengths, $k_\perp \rho_{te} > 2$, the residual value approaches zero as $\langle k_\perp \rho_{ts} \rangle_\psi^{-1}$ when using fully kinetic species and also for the adiabatic electron approximation. In figure 4.7, it is shown that the adiabatic electron approximation in tokamaks is good for $k_\perp \rho_{te} \lesssim 0.1$. In figure 4.8, we reproduce the results with CAS3D-K in figure 4.7 together with the evaluation of (2.57) for different values of $\tau := T_e/T_i$. On the electron scale, the results with the adiabatic electron approximation and with kinetic electrons only coincide in the limit $\tau \gg 1$. Due to the reasons pointed out above, the simulations with EUTERPE have been carried out only for $k_\perp \rho_{ti} < 1$. Finally, it is obvious that the results of the forced system of figures 4.4 and 4.5 and the initial value problem of figure 4.7 behave in a completely different way for $k_\perp \rho_{ti} \gtrsim 1$.

4.2.2 Stellarator

Now, we turn to stellarator geometry. We use an equilibrium for the standard configuration of the stellarator W7-X obtained with VMEC. The q profile is given in figure 4.6 and we take flat density and temperature profiles with $T_i = T_e$. In figure 4.9, calculations of the residual level with CAS3D-K, EUTERPE and the full flux surface version of GENE are shown for $\psi = 0.25$. Two curves correspond to CAS3D-K computations, one using adiabatic electrons (see equation (2.59)) and the other one using kinetic electrons (see equation (2.57)). In figure 4.9, the results of the gyrokinetic simulations were

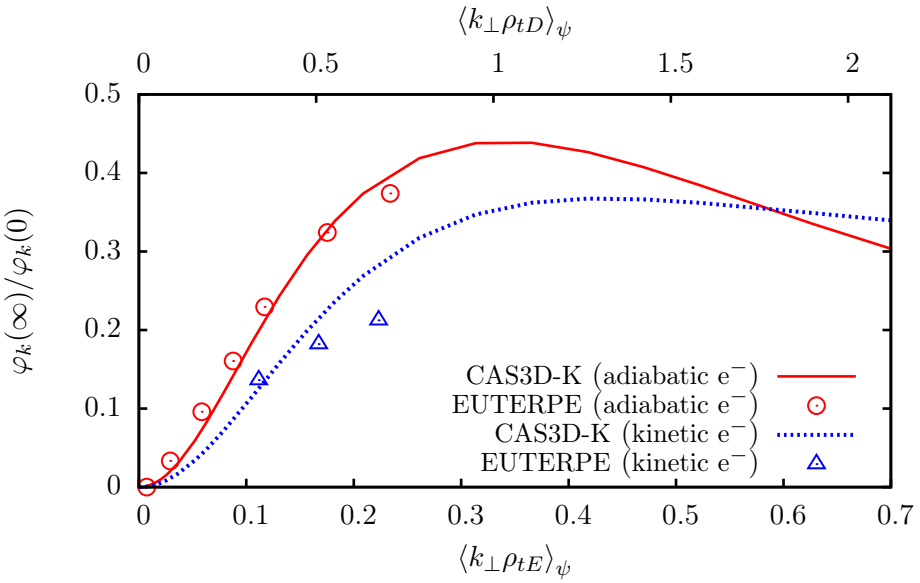

Figure 4.10: Residual zonal flow level for the initial value problem in the standard configuration of the W7-X stellarator at $\psi = 0.25$, with deuterium ions (D) and kinetic heavy electrons (E) ($m_E = 400 m_e$) and also using the approximation of adiabatic electrons.

obtained employing both the approximation of adiabatic electrons and fully kinetic species with GENE, whereas only calculations with adiabatic electrons are shown for EUTERPE. These results have been fitted to an exponential decay model (4.10) to get the residual value. Similar results can be obtained with an algebraic decay model as suggested in reference [11]. The results of CAS3D-K show remarkable agreement with both gyrokinetic codes.

As explained and quantified at the end of this section, the gyrokinetic simulations with kinetic species are much more demanding in terms of computational resources than those with adiabatic electrons. Global simulations with EUTERPE using fully kinetic electrons in stellarator geometry would require an extremely large computing time. This time can be reduced by increasing the mass of the species involved. We have calculated for deuterium ions and kinetic heavy electrons $s = \{D, E\}$, with $m_E = 400\, m_e$ and $T_D = T_E$. The results are shown in figure 4.10 where we compare the residual level calculated with EUTERPE and CAS3D-K at $\psi = 0.25$. The results with adiabatic electrons shown in this figure are exactly the same as those in figure 4.9, also with adiabatic electrons and obtained for hydrogen ions. Note that, with adiabatic electrons, as the residual level only depends on $\langle k_\perp \rho_{ti} \rangle_\psi$, the curves for hydrogen or deuterium ions are exactly the same.

In figure 4.9, like in tokamaks, we find local maxima of the residual level centered around the scales of the electron and ion Larmor radii. However,

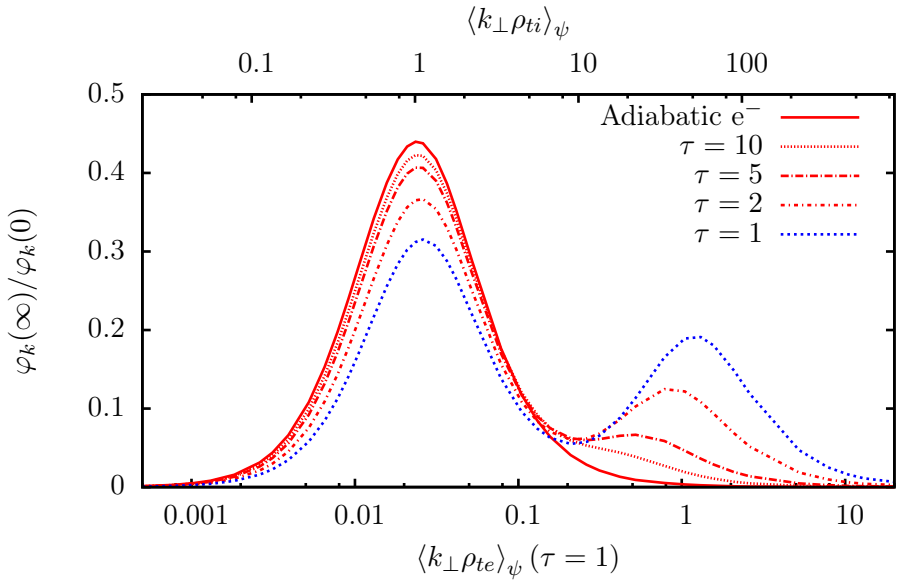

Figure 4.11: The same evaluation with CAS3D-K of equation (2.59) as in figure 4.9, with the adiabatic electron approximation, and the evaluation of equation (2.57) with fully kinetic species for different values of τ.

at long wavelengths, $k_\perp \rho_{ti} \ll 1$, the residual level as a function of $k_\perp \rho_{ti}$ behaves very differently in tokamaks and in stellarators (see, for example, figures 4.7 and 4.9). This can be easily understood by expanding (2.57) and (2.59) in $k_\perp \rho_{ti} \ll 1$. The numerator of these expressions scales quadratically with $k_\perp \rho_{ti}$ in tokamaks and stellarators. The difference comes from the denominator. In a stellarator, the denominator is non-zero when $k_\perp \rho_{ti} = 0$. However, in a tokamak the denominator scales quadratically with $k_\perp \rho_{ti}$. The denominator has been often related to the shielding effects of collisionless classical and neoclassical polarization currents [4, 6, 13, 14].

It is worth giving explicitly the $k_\perp \rho_{ti} \ll 1$ expansions of (2.57) and (2.59) in a stellarator and discussing a stellarator specific point in detail. The lowest order term of (2.57) gives

$$\frac{\varphi_k(\infty)}{\varphi_k(0)} = \frac{(1-\epsilon_t)\,\langle k_\perp \rho_{ti} \rangle_\psi^2}{\epsilon_t \left(1 + T_i/(Z_i^2 T_e)\right)} + O(\langle k_\perp \rho_{ti} \rangle_\psi^4), \tag{4.11}$$

where $\epsilon_t = n_s^{-1}\{1\}_s^{\text{trapped}}$ is the fraction of trapped particles. Here, the superindex "trapped" means that the phase-space integration is performed only over the trapped region. However, if we use the approximation of adiabatic electrons, (2.59), we find

$$\frac{\varphi_k(\infty)}{\varphi_k(0)} = \frac{(1-\epsilon_t)\,\langle k_\perp \rho_{ti} \rangle_\psi^2}{\epsilon_t} + O(\langle k_\perp \rho_{ti} \rangle_\psi^4). \tag{4.12}$$

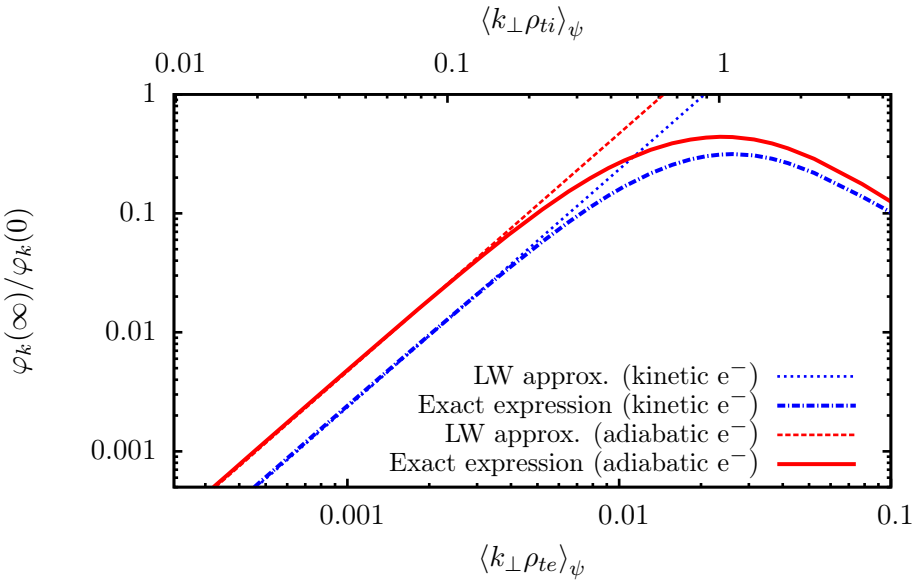

Figure 4.12: Range of validity of the long-wavelength (LW) approximations, when using fully kinetic species (4.11) and with the approximation of adiabatic electrons (4.12), compared to the exact expressions (2.57) and (2.59), in the standard configuration of the W7-X stellarator at $\psi = 0.25$ and with $T_i = T_e$.

Hence, in stellarators, the adiabatic electron approximation gives and incorrect residual zonal flow, even at long wavelengths. This has been pointed out in references [7, 16] and is confirmed by the calculations shown in figures 4.9 and 4.10. The curves in figure 4.11 for different values of τ quantify the error of the adiabatic electron approximation for any wavelength. As can be seen in this figure, the residual level obtained with this approximation, only coincides with that obtained with fully kinetic species in the limit $\tau \gg 1$. In figure 4.12, we plot the curves in figure 4.9 corresponding to CAS3D-K together with the evaluation of their expansions to lowest order in $k_\perp \rho_{ti} \ll 1$, (4.11) and (4.12). It is clear from figure 4.12 that (4.11) and (4.12) are good approximations of (2.57) and (2.59) respectively for $k_\perp \rho_{ti} \lesssim 0.2$.

We point out that at scales comparable to the ion Larmor radius, $k_\perp \rho_{ti} \sim 1$, the residual level appears to be larger in stellarators than in tokamaks (see, for example, figures 4.8 and 4.11). In order to discard trivial explanations, we have studied with CAS3D-K the residual level in a tokamak configuration with the same aspect ratio and q profile as those of the standard configuration of W7-X and the results are much closer to the tokamak case than to the stellarator results. This is not surprising because, as shown in reference [6], not only the aspect ratio but also shaping effects like elongation, triangularity and Shafranov shift, among others, affect the residual level. We leave for a

future work a detailed study of the magnetic configuration influence on the residual level.

4.2.3 Simulation conditions and computational time

The converged results shown in this chapter require disparate computing resources, depending on the code and the physical problem. The relevant numerical parameters and the computational resources required by each code are described below.

In CAS3D-K, we used 256 points for the integration over the velocity coordinate v, with $0 \leq v \leq 4\pi v_{ts}$. For the integration over the λ coordinate, we used 72 integration points in the tokamak and 24 in W7-X. Along the field line, we used 32 points at long wavelengths and up to 4096 for short wavelengths. This resolution allows the correct integration of the highly oscillatory functions. Thanks to axisymmetry, in a tokamak all field lines on a flux surface are equivalent. In W7-X, we used 1024 field lines to cover the flux surface for passing particles. For the evaluation of δ_s in the stellarator case, all the modes with $|m| \leq 8$ and $|n| \leq 8$ were retained. The calculations were carried out in the EULER cluster at CIEMAT, equipped with Xeon 5450 quadcore processors at 3 GHz and 4XDDR Infiniband network.

In GENE, a 1D spatial grid along the field line (z coordinate) is used in the tokamak cases while in stellarator simulations a 2D spatial grid in coordinates (y, z) is used to describe a full flux surface (y is the coordinate along the binormal direction). In velocity space, a 2D grid in parallel velocity and magnetic moment coordinates $(v_\parallel, \mu)$ is used in both the tokamak and the stellarator cases. The resolution of the spatial and velocity grids used are given in tables 4.1 and 4.2 for long and short wavelengths together with the time step and the total simulation time for each case. Times are given in $1/\Omega_G$ units, with $\Omega_G = a/v_{te}$, where we recall that a is the minor radius and v_{te} is the thermal velocity of electrons. The GENE simulations were run in HYDRA [61], equipped with Intel IvyBridge at 2.8 GHz and SandyBridge-EP at 2.6 GHz processors interconnected by Infiniband FDR14.

In EUTERPE, the electric potential is represented in a 3D spatial grid in PEST coordinates (s_E, θ_E, ϕ_E) whose radial resolution must be large enough to correctly represent the potential perturbation. The number of markers was set according to the grid resolution to maintain the ratio of markers per grid cell approximately constant. A low-pass squared filter in Fourier space $(k_{\theta_E}, k_{\phi_E})$ is used to reduce the noise. In table 4.3 the resolution of the spatial grid $(n_{s_E}, n_{\phi_E}, n_{\phi_E})$, the number of markers, the filter cutoff, the time step and the total simulation time used for each case are given. Times are given in $1/\Omega_E$ units, where $\Omega_E = eB^*/m_i$, e is the elementary charge, m_i is the ion mass and B^* is the average of the magnetic field along the magnetic axis. The EUTERPE simulations were carried out in EULER and MareNostrum III [62], equipped with Intel SandyBridge-EP processors at

	long wavelength ($k_\perp \rho_{ti} < 1$)		
	adiabatic e^-	kinetic e^-	
n_z	64	64	
$n_{v_\parallel}$	128	1024	
n_μ	40	40	tokamak
Δt_G	$1-6$	$0.03-0.06$	
T_G	$4000-15000$	$3000-10000$	
n_y	64	64	
n_z	256	128	
$n_{v_\parallel}$	128	$256-512$	stellarator
n_μ	20	20	
Δt_G	$4-8$	0.06	
T_G	$100000-200000$	40000	

Table 4.1: Numerical parameters used in the GENE simulations for long wavelengths. The time step (Δt_G) and the total simulation time (T_G) are given in Ω_G^{-1} units, with $\Omega_G = a/v_{te}$.

	short wavelength ($k_\perp \rho_{ti} > 1$)		
	adiabatic e^-	kinetic e^-	
n_z	128	256	
$n_{v_\parallel}$	$1024-2048$	$2048-4096$	
n_μ	40	40	tokamak
Δt_G	$0.2-1$	0.02	
T_G	$4000-10000$	150	
n_y	64	64	
n_z	128	128	
$n_{v_\parallel}$	128	$128-512$	stellarator
n_μ	20	$10-20$	
Δt_G	$0.2-5$	0.06	
T_G	$300-5000$	$10000-550000$	

Table 4.2: Numerical parameters used in the GENE simulations for short wavelengths. The time step (Δt_G) and the total simulation time (T_G) are given in Ω_G^{-1} units, with $\Omega_G = a/v_{te}$.

long wavelength	tokamak	stellarator	
$(k_\perp \rho_{ti} < 1)$	adiabatic e^-	adiabatic e^-	kinetic $e^{-\dagger}$
n_{s_E}	$32 - 192$	$64 - 192$	$32 - 96$
$n_{\theta_E} \times n_{\phi_E}$	16×16	32×32	16×16
# of markers	40 M − 240 M	40 M − 240 M	40 M − 120 M
filter cutoff	5	$5, 10^{\dagger\dagger}$	5
Δt_E	$10 - 5$	$50 - 20$	0.5
T_E	60000	400000	45000

Table 4.3: Numerical parameters used in the EUTERPE simulations. The time step (Δt_E) and the total simulation time (T_E) are given in Ω_E^{-1} units, with $\Omega_E = eB^*/m$. †This range corresponds to calculations with deuterium ions and heavy electrons. ††Only for the shortest-wavelength case.

2.6 GHz and Infiniband FDR10 interconnection.

In table 4.4 we illustrate the computational cost, in total CPU core hours (that is, the time summed up over all the cores employed in the simulation), for the different codes and cases studied. Of course, the values shown in table 4.4 are simply indicative, as they depend on the numerical details of the simulations and the type of CPU employed in each calculation. In addition, a systematic analysis of the optimal resolution to carry out the computations with each code has not been performed. The main conclusion that we can extract from table 4.4 is that determining the residual zonal flow with CAS3D-K is faster than with GENE and EUTERPE. This is specially true for stellarators. The reason is that in stellarators only passing particles contribute to the residual value, while in tokamaks also trapped particles count, and trapped trajectories typically demand a more careful numerical treatment than passing ones. Whereas the CAS3D-K calculation simply drops the contribution from the trapped region, the gyrokinetic runs simulate all trajectories. However, we can see from table 4.4 that the computational cost when using the gyrokinetic codes is higher in stellarator geometry because it requires increased resolution in phase-space to obtain converged results.

We observe that EUTERPE, a 3D global code, requires much more CPU time than GENE, particularly in the tokamak case, in which the flux tube version of GENE is used. The reason is that EUTERPE simulates the whole plasma while GENE is here operated in a radially local limit. The computational cost with EUTERPE increases with $k_\perp \rho_{ti}$, because more flux surfaces have to be considered as $k_\perp$ increases to properly resolve the radial structure of the potential in all the plasma volume. In EUTERPE the different values of $k_\perp \rho_{ti}$ at a given radial position are obtained by keeping the value of ρ_{ti} (determined by the ion mass, the temperature and the magnetic field) and varying the value of $k_\perp$. In CAS3D-K, the resolution at short wavelengths must be increased to correctly calculate the highly oscillatory functions re-

	long wavelengths $k_\perp \rho_{ti} < 1$		short wavelengths $k_\perp \rho_{ti} > 1$		
	adiabatic e^-	kinetic e^-	adiabatic e^-	kinetic e^-	
CAS3D-K	1.5	3	15	30	
GENE	10[††]	1300	150	200	tokamak
EUTERPE	7000	—	—	—	
CAS3D-K	0.5	1	4	8	
GENE	2000	40000	200	250000	stellarator
EUTERPE	20000	80000[†]	—	—	

Table 4.4: Estimated CPU time (total core hours) to obtain the residual zonal flow value with the different codes. We give estimations for tokamaks and stellarators; for adiabatic and kinetic electrons; and for long and short wavelengths. [†]This range corresponds to calculations with deuterium ions and heavy electrons. [††]For very small wavenumbers, GENE computes the residual zonal flow in a tokamak in approximately 0.5 CPU hours.

lated to the finite orbit width and the finite Larmor radius effects.

The analytical expression obtained by Rosenbluth and Hinton in reference [4], given by equation (4.1), has been largely used as a linear benchmark for gyrokinetic codes in tokamak geometry and in the long-wavelength limit. The results presented in this chapter show that CAS3D-K can be used to perform those benchmarks not only in tokamak geometry but also in stellarator geometry and for arbitrary wavelengths. Examples of such benchmarks are given in figure 4.7 for the global code EUTERPE and the flux tube version of GENE in tokamak geometry, and in figure 4.9 for EUTERPE and the full flux surface version of GENE in stellarator geometry.

4.3 Residual zonal-flow with a source term in the quasineutrality equation

It is a matter of fact that the tokamak calculation including a source term in the quasineutrality equation [6, 14] has become quite popular in the literature. Just for completeness, we give an analogous calculation for the stellarator in this section using gyrokinetic simulations and CAS3D-K. We also show the results for the tokamak using gyrokinetic codes (these were not included in Section 4.1). In particular, we calculate the residual zonal-flow of the forced system described in Section 4.1 in the tokamak and parameters given in Section 4.2.1. We also derive the equivalent expression for stellarators and we calculate its value in the standard configuration of the W7-X stellarator described in Section 4.2.2. In both cases, we show calculations obtained with CAS3D-K and GENE.

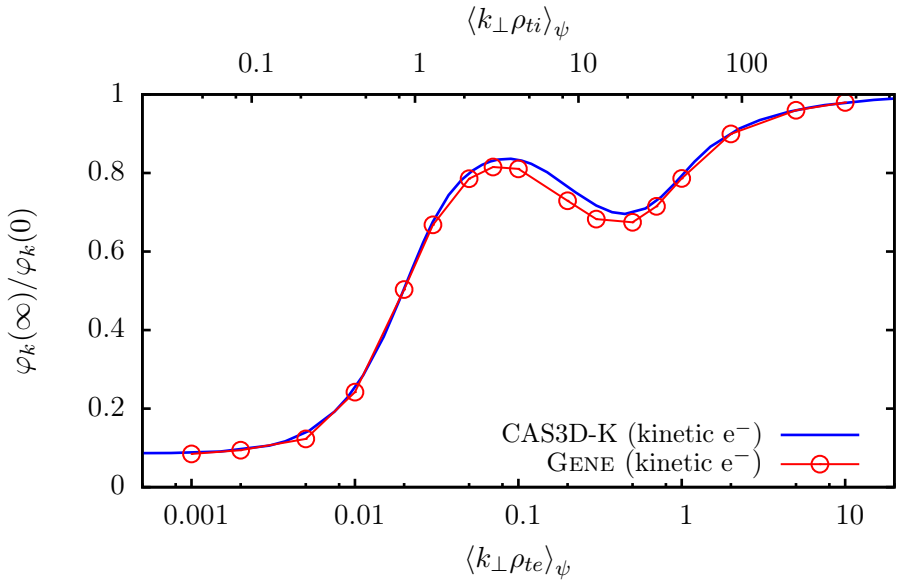

Figure 4.13: The evaluation of equation (4.4) with CAS3D-K for the tokamak of Section 4.2 at $\psi = 0.25$ is shown. The corresponding simulation with GENE including a source term in the quasineutrality equation is also plotted.

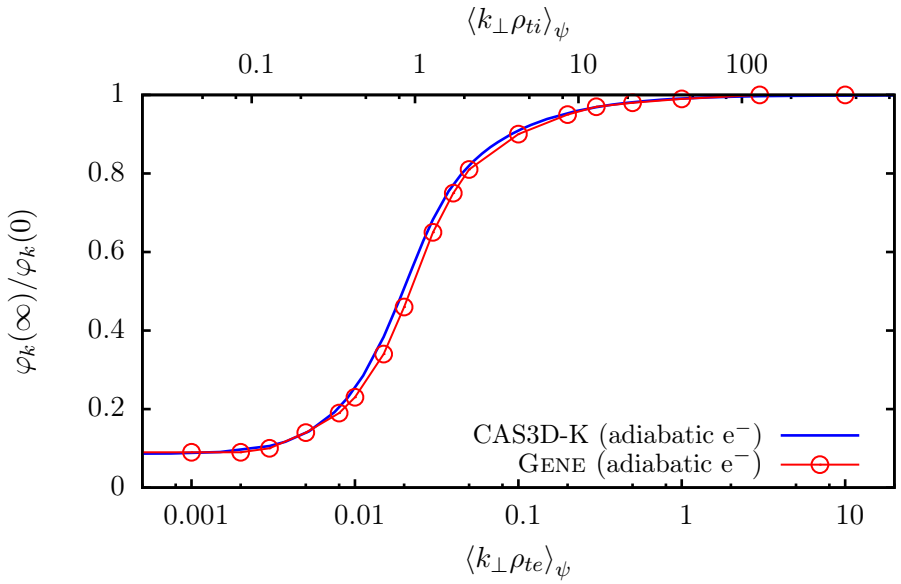

Figure 4.14: The same calculations as in figure 4.13, but employing adiabatic electrons.

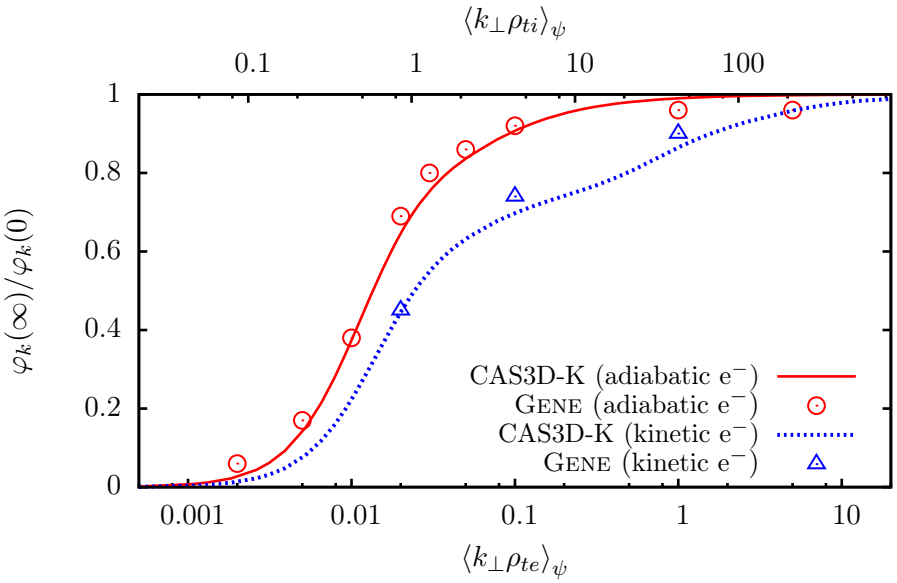

Figure 4.15: The results of the forced case for the standard configuration of the stellarator W7-X at $\psi = 0.25$.

Figures 4.13 and 4.14 are analogous to figures 4.4 and 4.5, but this time we employ the equilibrium and parameters of Section 4.2.1, and show the results obtained by both CAS3D-K and GENE. The gyrokinetic simulations have been carried out by taking vanishing initial condition and adding a constant source term to the quasineutrality equation. As can be seen in figures 4.13 and 4.14, both calculations show really good agreement.

A formulation of the residual zonal flow problem similar to that given in [6, 14] gives, in the stellarator case,

$$\frac{\varphi_k(\infty)}{\varphi_k(0)} = \frac{\sum_s \frac{Z_s^2}{T_s} \left\{1 - J_{0s}^2\right\}_s}{\sum_s \frac{Z_s^2}{T_s} \left[\{1\}_s - \left\{ \mathrm{e}^{-\mathrm{i}k_\psi \delta_s} J_{0s}\, \overline{\mathrm{e}^{\mathrm{i}k_\psi \delta_s} J_{0s}} \right\}_s^{\overline{\omega_s}=0}\right]}, \tag{4.13}$$

if all species are kinetic. In the approximation of adiabatic electrons, one has

$$\frac{\varphi_k(\infty)}{\varphi_k(0)} = \frac{\sum_{s\neq e} \frac{Z_s^2}{T_s} \left\{1 - J_{0s}^2\right\}_s}{\sum_{s\neq e} \frac{Z_s^2}{T_s} \left[\{1\}_s - \left\{ \mathrm{e}^{-\mathrm{i}k_\psi \delta_s} J_{0s}\, \overline{\mathrm{e}^{\mathrm{i}k_\psi \delta_s} J_{0s}} \right\}_s^{\overline{\omega_s}=0}\right]}. \tag{4.14}$$

The evaluation of these expressions with CAS3D-K, for the standard configuration of the stellarator W7-X and the parameters detailed in Section 4.2.2, is shown in figure 4.15. The results for the GENE simulations are also plotted. As can be seen in this figure, both calculations show good agree-

ment. Note that, the GENE calculations in this case require large resolution parameters and therefore large computational resources.

4.4 Summary of results in this chapter

In this chapter we have computed the residual zonal flow level in tokamak and stellarator geometries for a wide range of radial wavelengths, using both the approximation of adiabatic electrons and fully kinetic electrons. We have compared the results of CAS3D-K with those obtained from two gyrokinetic codes: the global code EUTERPE and the radially local versions of GENE (full flux surface and flux tube). The comparisons are shown in figures 4.7, 4.9 and 4.10.

A stellarator specific effect has been discussed in detail. Namely, the fact that the adiabatic electron approximation gives incorrect zonal flow residuals even for $k_\perp \rho_{ti} \ll 1$, unlike in tokamaks. This effect has also been confirmed by means of gyrokinetic simulations. This is shown in figures 4.9, 4.10 and 4.11.

Finally, we stress the efficiency of our semianalytical method to determine the residual zonal flow. Gyrokinetic simulations with GENE and EUTERPE to obtain the residual level are computationally expensive, especially with fully kinetic species, in the short-wavelength region, and in stellarator geometry. On the contrary, the calculations with CAS3D-K are less demanding (see table 4.4), particularly in stellarator geometry. These results show that CAS3D-K is a useful tool to calculate fast and accurately the residual level in any toroidal geometry and for arbitrary wavelengths. This code is even more useful in stellarator geometry as kinetic electrons must be considered to correctly calculate the residual level. It can also provide a good benchmark for gyrokinetic codes.

Chapter 5

Zonal-flow oscillation frequency in stellarators and rippled tokamaks

In this chapter, we prove the validity of the expression obtained in Section 2.4 for the zonal-flow oscillation frequency, Ω_{ZF}, and the approximations used in its derivation. For this purpose, we evaluate equation (2.66) with CAS3D-K in several stellarator devices and in a large aspect ratio tokamak with different ripple values. We compare these results with those from gyrokinetic simulations. The results shown in this chapter have been accepted for publication recently and can be found in Reference [20].

This chapter is organized as follows. In Section 5.1 we compute Ω_{ZF}, with both methods (that is, the semianalytical approach and the one based on gyrokinetic simulations), in a tokamak configuration with different ripple values, which we use as a test to gain insight into the problem and check the limitations of the numerical methods. In Section 5.2 we calculate the zonal-flow frequency in the W7-X, TJ-II and LHD stellarators. The computational requirements of the two approaches to the calculation of Ω_{ZF} are compared in Section 5.3. Finally, a summary of the results in this chapter is given in Section 5.4.

5.1 Zonal-flow oscillation frequency in tokamaks with ripple

For the evaluation of the zonal-flow frequency (2.66) with CAS3D-K, we use the integral version of δ_s for trapped particles (3.13). This method represents a significant simplification in contrast to the method using bounce harmonics (3.18). Although calculations of δ_s obtained with both methods give the same value, the integral method requires less computational resources and

is faster, especially in stellarators. In the evaluation of (2.62), (2.63) and (2.64), the integration over the velocity space is performed analytically as only moments of the Maxwellian distribution function are required. Some of these moments are given in equations (3.25), (3.26) and (3.27).

For the evaluation of the zonal-flow frequency with the gyrokinetic codes, we use the initial conditions and the fitting method described in Section 4.2. Several dynamics are mixed in the zonal flow relaxation, which makes the fitting process non trivial. First, there is a decay to the residual level and, superimposed to it, several oscillations appear with different amplitudes and characteristic times (see figures 5.3 and 5.6). Since we are interested in the low frequency oscillation, the faster GAM oscillation, usually appearing at the beginning of the relaxation, is excluded in the fitting process. A very similar value is obtained if instead of using the $(m, n) = (0, 0)$ component of the potential its flux-surface average is used[1].

Although the comparison of the frequency calculations is focused on the codes CAS3D-K and EUTERPE, calculations for the W7-X standard configuration have also been carried out with the code GENE. In the GENE simulations shown in this chapter, we use the full-flux surface version. In this version, the code is spectral in the radial coordinate, while a finite difference scheme is used for the coordinates along the flux surface.

In the calculations shown in this chapter, we also use flat density and temperature profiles and assume a plasma with adiabatic electrons and singly charged ions in all cases. Although the normalized toroidal flux, ψ, is used as a radial coordinate in the codes, in what follows we show the results in the more natural coordinate $r/a := \sqrt{\psi}$, where a is the minor radius of the device.

In order to understand the influence of the magnetic configuration on the zonal-flow oscillation, we take an axisymmetric tokamak equilibrium and modify it by adding different amounts of ripple. The resulting set of configurations allows us to study the dependence of the frequency on the ripple size and calibrate the calculation methods in a controlled path continuously departing from the axisymmetric case.

We start with the VMEC[2] input for the equilibrium of an axisymmetric large aspect ratio tokamak (LART) with major radius $R = 5$ m and minor radius $a = 0.5$ m, and modify the plasma boundary to include ripple. The ripple is generated by adding a poloidally symmetric perturbation to the boundary shape through non-zero coefficients $(R_{\mathrm{BC}})_{0,2}$ and $(Z_{\mathrm{BS}})_{0,2}$. We always take $(R_{\mathrm{BC}})_{0,2} = (Z_{\mathrm{BS}})_{0,2}$. Here, $(R_{\mathrm{BC}})_{m,n}$ and $(Z_{\mathrm{BS}})_{m,n}$ are the cosine and sine components of the coordinates R_{BC} and Z_{BS} at the boundary,

[1] Note that the $(m, n) = (0, 0)$ component of the potential is not strictly equal to the flux-surface average of the potential, in general.

[2] The equilibrium in VMEC can be expressed in flux coordinates and toroidal-cylindrical coordinates $\{R, Z, \hat{\phi}\}$, where R is the toroidal radial coordinate, Z is the height above the toroidal midplane and $\hat{\phi}$ is the toroidal angle.

$(Z_{\rm BS})_{0,2}$	r/a	B_{00} [T]	B_{10} [T]	B_{20} [T]	B_{30} [T]	B_{12} [T]	$\sqrt{\sum B_{mn}^2}$ [T]
	0.40	2.47	-9.58×10^{-2}	1.87×10^{-3}	-3.65×10^{-5}	-9.71×10^{-14}	3.40×10^{-13}
0	0.60	2.46	-1.45×10^{-1}	4.30×10^{-3}	-1.28×10^{-4}	1.06×10^{-13}	6.48×10^{-13}
	0.80	2.45	-1.93×10^{-1}	7.69×10^{-3}	-3.07×10^{-4}	-3.86×10^{-13}	7.99×10^{-13}
	0.40	2.47	-9.58×10^{-2}	1.87×10^{-3}	-3.65×10^{-5}	-5.99×10^{-6}	1.01×10^{-5}
0.0001	0.60	2.46	-1.45×10^{-1}	4.30×10^{-3}	-1.28×10^{-4}	-8.98×10^{-6}	1.27×10^{-5}
	0.80	2.45	-1.93×10^{-1}	7.69×10^{-3}	-3.07×10^{-4}	-1.19×10^{-5}	1.64×10^{-5}
	0.40	2.47	-9.58×10^{-2}	1.87×10^{-3}	-3.65×10^{-5}	-5.71×10^{-5}	8.76×10^{-5}
0.001	0.60	2.46	-1.45×10^{-1}	4.30×10^{-3}	-1.28×10^{-4}	-8.65×10^{-5}	1.30×10^{-4}
	0.80	2.45	-1.93×10^{-1}	7.69×10^{-3}	-3.07×10^{-4}	-1.17×10^{-4}	1.67×10^{-4}
	0.40	2.47	-9.58×10^{-2}	1.87×10^{-3}	-3.65×10^{-5}	-2.86×10^{-4}	4.40×10^{-4}
0.005	0.60	2.46	-1.45×10^{-1}	4.30×10^{-3}	-1.28×10^{-4}	-4.33×10^{-4}	6.49×10^{-4}
	0.80	2.45	-1.93×10^{-1}	7.69×10^{-3}	-3.07×10^{-4}	-5.83×10^{-4}	8.35×10^{-4}
	0.40	2.47	-9.58×10^{-2}	1.87×10^{-3}	-3.65×10^{-5}	-5.66×10^{-4}	9.70×10^{-4}
0.01	0.60	2.46	-1.45×10^{-1}	4.30×10^{-3}	-1.28×10^{-4}	-8.62×10^{-4}	1.33×10^{-3}
	0.80	2.45	-1.93×10^{-1}	7.69×10^{-3}	-3.07×10^{-4}	-1.17×10^{-3}	1.67×10^{-3}
	0.40	2.47	-9.58×10^{-2}	1.87×10^{-3}	-3.65×10^{-5}	-1.69×10^{-3}	3.13×10^{-3}
0.03	0.60	2.46	-1.45×10^{-1}	4.30×10^{-3}	-1.28×10^{-4}	-2.58×10^{-3}	4.02×10^{-3}
	0.80	2.45	-1.93×10^{-1}	7.69×10^{-3}	-3.06×10^{-4}	-3.50×10^{-3}	5.02×10^{-3}
	0.40	2.47	-9.57×10^{-2}	1.86×10^{-3}	-3.64×10^{-5}	-2.81×10^{-3}	5.43×10^{-3}
0.05	0.60	2.46	-1.45×10^{-1}	4.29×10^{-3}	-1.28×10^{-4}	-4.31×10^{-3}	6.76×10^{-3}
	0.80	2.45	-1.93×10^{-1}	7.68×10^{-3}	-3.06×10^{-4}	-5.83×10^{-3}	8.42×10^{-3}
	0.40	2.47	-9.56×10^{-2}	1.86×10^{-3}	-3.64×10^{-5}	-3.94×10^{-3}	7.77×10^{-3}
0.07	0.60	2.46	-1.45×10^{-1}	4.29×10^{-3}	-1.27×10^{-4}	-6.03×10^{-3}	9.58×10^{-3}
	0.80	2.45	-1.93×10^{-1}	7.67×10^{-3}	-3.05×10^{-4}	-8.17×10^{-3}	1.19×10^{-2}
	0.40	2.47	-9.54×10^{-2}	1.85×10^{-3}	-3.62×10^{-5}	-5.63×10^{-3}	1.16×10^{-2}
0.1	0.60	2.47	-1.44×10^{-1}	4.27×10^{-3}	-1.27×10^{-4}	-8.59×10^{-3}	1.41×10^{-2}
	0.80	2.45	-1.93×10^{-1}	7.64×10^{-3}	-3.04×10^{-4}	-1.16×10^{-2}	1.73×10^{-2}
	0.40	2.48	-9.48×10^{-2}	1.84×10^{-3}	-3.57×10^{-5}	-8.44×10^{-3}	1.89×10^{-2}
0.15	0.60	2.47	-1.44×10^{-1}	4.24×10^{-3}	-1.25×10^{-4}	-1.29×10^{-2}	2.24×10^{-2}
	0.80	2.46	-1.92×10^{-1}	7.58×10^{-3}	-3.01×10^{-4}	-1.76×10^{-2}	2.69×10^{-2}
	0.40	2.48	-9.41×10^{-2}	1.81×10^{-3}	-3.51×10^{-5}	-1.13×10^{-2}	2.79×10^{-2}
0.2	0.60	2.48	-1.43×10^{-1}	4.19×10^{-3}	-1.23×10^{-4}	-1.74×10^{-2}	3.21×10^{-2}
	0.80	2.46	-1.90×10^{-1}	7.50×10^{-3}	-2.96×10^{-4}	-2.35×10^{-2}	3.77×10^{-2}
	0.40	2.49	-9.31×10^{-2}	1.79×10^{-3}	-3.43×10^{-5}	-1.42×10^{-2}	3.88×10^{-2}
0.25	0.60	2.48	-1.41×10^{-1}	4.12×10^{-3}	-1.21×10^{-4}	-2.18×10^{-2}	4.34×10^{-2}
	0.80	2.47	-1.88×10^{-1}	7.39×10^{-3}	-2.91×10^{-4}	-2.96×10^{-2}	4.99×10^{-2}
	0.40	2.50	-9.20×10^{-2}	1.75×10^{-3}	-3.34×10^{-5}	-1.72×10^{-2}	5.17×10^{-2}
0.3	0.60	2.49	-1.39×10^{-1}	4.04×10^{-3}	-1.18×10^{-4}	-2.64×10^{-2}	5.67×10^{-2}
	0.80	2.48	-1.86×10^{-1}	7.26×10^{-3}	-2.84×10^{-4}	-3.58×10^{-2}	6.38×10^{-2}

Table 5.1: Some relevant quantities that describe the rippled tokamak configurations studied in the text as a function of the non-axisymmetric perturbation to the plasma boundary. Recall that we take $(R_{\rm BC})_{0,2} = (Z_{\rm BS})_{0,2}$.

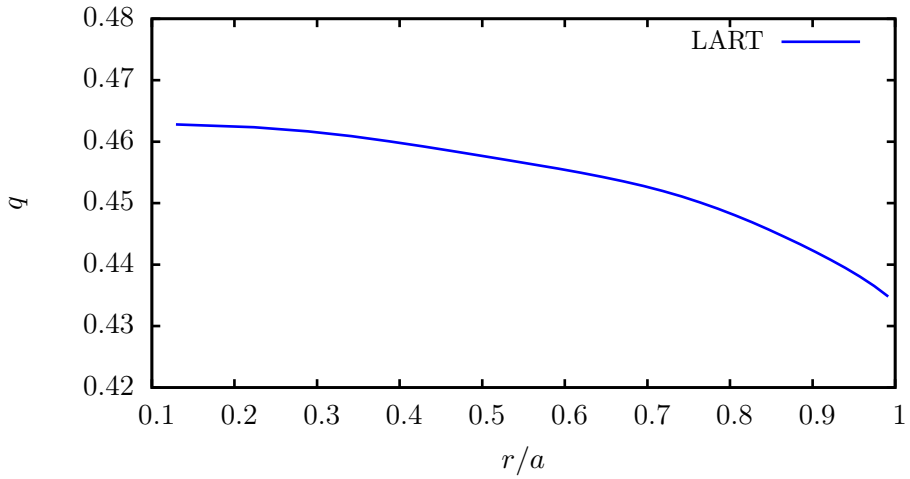

Figure 5.1: Radial profile of the safety factor of the large aspect ratio tokamak (LART) equilibria described in Section 5.1.

respectively, and m and n are poloidal and toroidal mode numbers (see [63]). We calculate the VMEC equilibrium employing 36 Fourier cosine components for B; specifically, $0 \leq |n| \leq 4$ and $0 \leq m \leq 3$. Note that, in this case $|B|$ can be written as a Fourier cosine series with coefficients $B_{m,n}$ as

$$|B|(\psi, \theta, \zeta) = \sum_{m=0}^{3} \sum_{n=-4}^{4} B_{m,n}(\psi) \cos(m\theta - n\zeta). \tag{5.1}$$

After including the $(Z_{\mathrm{BS}})_{0,2} \neq 0$ perturbation to the boundary, several modes $B_{0,n}$, with $n \neq 0$, are generated, whose size increases with the size of $(Z_{\mathrm{BS}})_{0,2}$. The non-axisymmetric perturbation can also modify slightly the axisymmetric components B_{00}, B_{10}, B_{20} and B_{30}. We list in table 5.1 some of the Fourier cosine coefficients of B at three radial positions for different values of the perturbation $(Z_{\mathrm{BS}})_{0,2}$. We give the axisymmetric components, the largest non-symmetric coefficient, B_{12}, and also $\sqrt{\sum_{n\neq 0} B_{mn}^2}$, where the sum includes all non-axisymmetric components. For the cases under study, we define the ripple by

$$\xi = \frac{\sqrt{\sum_{n\neq 0} B_{mn}^2}}{B_{10}}. \tag{5.2}$$

This parameter will be used as a measure of the perturbation to the axisymmetric equilibrium.

The average magnetic field strength at the axis is $B_0 \simeq 2.48$ T for the non-perturbed case and decreases slightly as the ripple amplitude is increased in the perturbed equilibria. The q profile, which is the same for all these

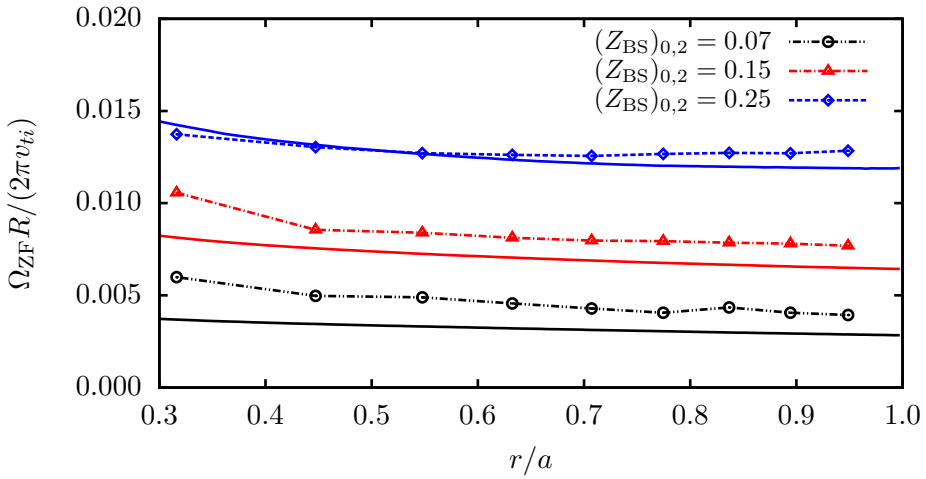

Figure 5.2: Radial dependence of $\Omega_{\rm ZF}$ in the large aspect ratio tokamak with different ripple values. The results of EUTERPE are shown with dashed lines (the specific points of the radial grid are marked) and the results of CAS3D-K are shown with solid lines.

configurations, is shown in figure 5.1. Note that this q profile is not standard for a tokamak configuration. We use unusually small safety factor values to reduce the amplitude of the GAM oscillation, which allows to observe the low frequency oscillation more clearly in the simulations.

In this set of configurations we calculate the zonal flow oscillation frequency with CAS3D-K and also by means of EUTERPE simulations. We use flat density and temperature profiles with $T_e = T_i = 5$ keV. In EUTERPE we use an initial perturbation with $k_\psi = 0.5\pi$, so that the normalized radial scale of the perturbation is $\langle k_\perp \rho_{ti} \rangle_\psi < 0.026$.

The radial dependence of the zonal-flow frequency calculated with CAS3D-K and EUTERPE for the tokamaks described above is shown in figure 5.2 for different ripple values. The oscillation frequency shows rather flat radial profiles with a slight increase near the magnetic axis. The calculations with both codes show good agreement and this is better in configurations with larger ripple amplitudes; the reason is given next. The time traces of the normalized zonal electric field corresponding to the cases shown in figure 5.2 are provided in figure 5.3 at a radial position of $r/a = 0.5$. As can be seen in this figure, the initial time steps are dominated by a fast oscillation followed by a decaying smaller-frequency oscillation which has larger amplitude in the tokamak configurations with larger ripple values. It is then clear from figure 5.3 that the estimation of the frequency with the fitting method is less precise in configurations with smaller ripple values because the amplitude of the zonal-flow oscillation in those configurations is actually small and it is

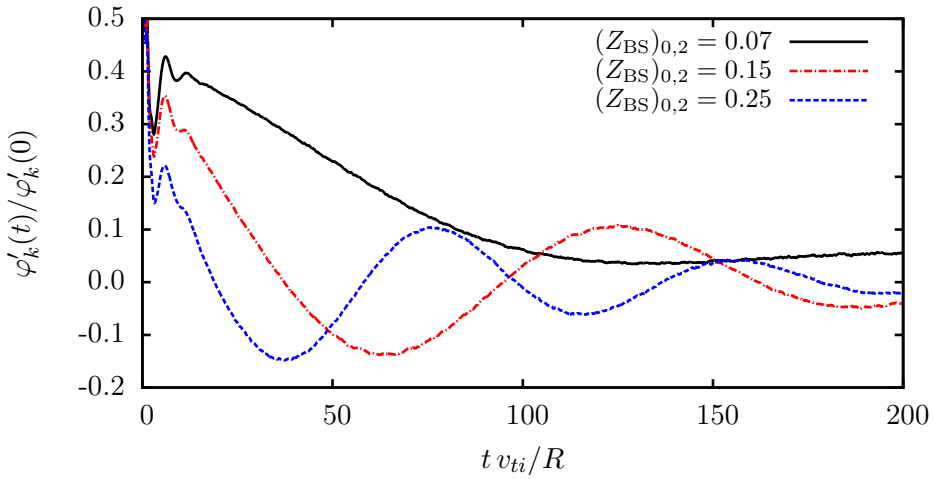

Figure 5.3: Time evolution of the normalized radial electric field in the large aspect ratio tokamak with different ripple values obtained with EUTERPE at $r/a = 0.5$.

superimposed to a slow decay to the residual level. In particular, the fitting method fails for sufficiently small ξ. Hence, the slight differences in the calculation of $\Omega_{\rm ZF}$ from the semianalytical approach and from the gyrokinetic simulations seem to be simply due to the uncertainties in the fitting method.

With CAS3D-K we can compute $\Omega_{\rm ZF}$ for arbitrarily small values of the ripple. Theoretically, a linear dependence of $\Omega_{\rm ZF}$ on ξ is expected for $\xi \ll 1$. Note that the results of [64] are applicable here and imply

$$\overline{\omega_i} \sim \frac{\xi \rho_{ti} v_{ti}}{L}, \tag{5.3}$$

for $\xi \ll 1$. Since A_0 and A_1 (see (2.62) and (2.63)) are dominated by the axisymmetric terms, the expansion of (2.66) for $\xi \ll 1$ yields

$$\Omega_{\rm ZF} \sim \xi \frac{v_{ti}}{L}. \tag{5.4}$$

This is confirmed by figure 5.4.

The series of perturbed tokamak equilibria used in this section have allowed us to clarify the dependence of the oscillation frequency with the ripple and understand some difficulties that appear in the process of comparing the two approaches that are the subject of this chapter. In particular, the calculation of the oscillation frequency by means of gyrokinetic simulations showed to have problems when the ripple size is too small because the fit of the potential time traces becomes complicated. The calculation with CAS3D-K, however, does not have this limitation and proved to be robust even with very small ripple amplitudes.

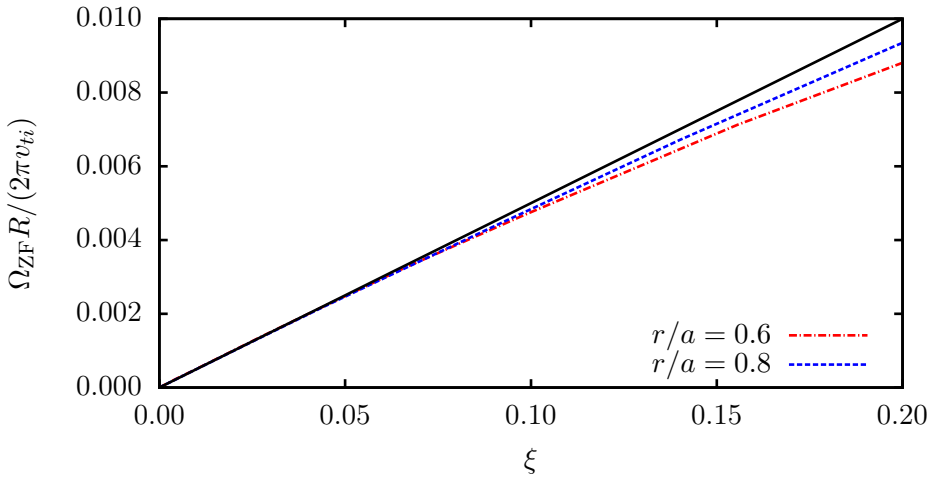

Figure 5.4: Dependence of $\Omega_{\rm ZF}$ with ξ in the large aspect ratio tokamak described in Section 5.1. Observe that for $\xi \ll 1$ the dependence is linear. The black straight line is a linear fit of the other two curves around $\xi = 0$.

5.2 Zonal-flow oscillation frequency in stellarators

In this section, we calculate the zonal-flow frequency in stellarator geometries with CAS3D-K and compare the results with those obtained from gyrokinetic simulations using the codes EUTERPE and GENE. Specifically, we work out the frequency in several magnetic configurations of the W7-X, TJ-II and LHD stellarators.

As discussed previously in the Introduction, the time evolution of an initial zonal-flow perturbation shows, in general, an initial damped GAM oscillation followed by a decaying low frequency oscillation. The collisionless damping of the GAM oscillation strongly depends on the safety factor, q. The safety factor profiles for all the stellarator configurations studied in this section are shown in figure 5.5. An example of the time traces of the zonal electric field obtained with EUTERPE is given in figure 5.6 for some of the considered stellarator configurations. As can be seen in this figure, the evolution of the initial zonal-flow perturbation is qualitatively different in each device. The standard and high mirror configurations of W7-X show a very small amplitude GAM oscillation before $t = 5R/v_{ti}$ and a much slower and higher-amplitude oscillation afterwards. The curve corresponding to LHD shows up to six clear cycles of the GAM oscillation, while the low frequency one is almost imperceptible. TJ-II represents an intermediate situation: the amplitude of the GAM oscillation is larger than in W7-X but smaller than in LHD. As for the low frequency oscillation, two oscillation cycles are perfectly observable. Therefore, obtaining an accurate value of

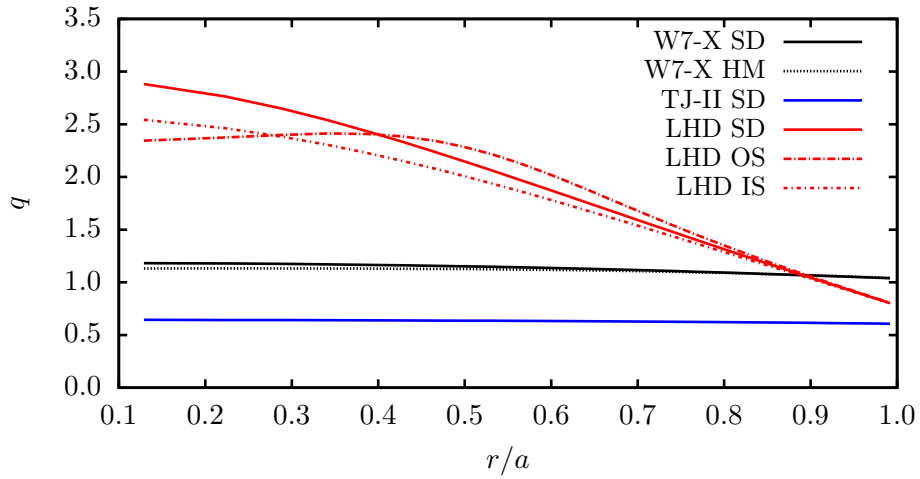

Figure 5.5: Safety factor radial profiles of the stellarator configurations described in Section 5.2.

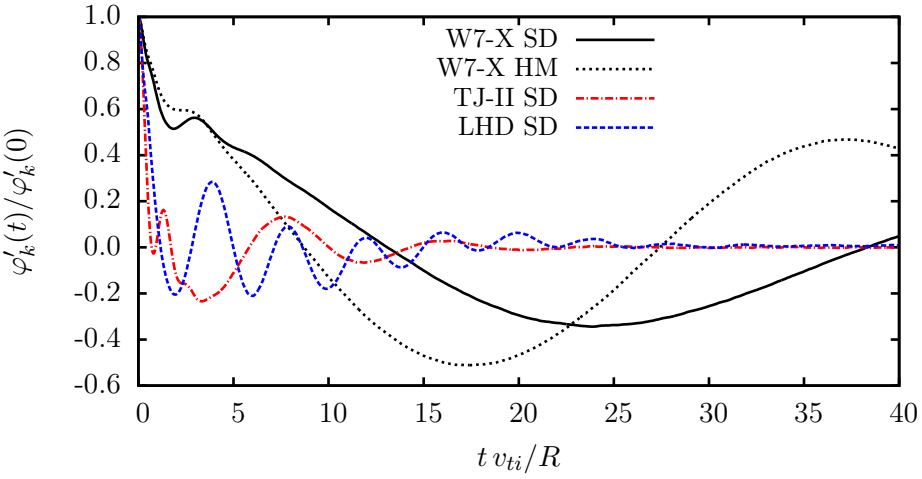

Figure 5.6: Time evolution of the normalized radial electric field obtained with EUTERPE for some of the stellarator configurations studied in Section 5.2 at $r/a = 0.5$. For the normalization of time in the horizontal axis, we have employed the major radius of each stellarator and the values of the thermal speed given in the corresponding subsection of Section 5.2. It is important to emphasize that, for the LHD SD curve, the oscillation that is seen with the naked eye does not correspond to the low-frequency oscillation but to the GAM.

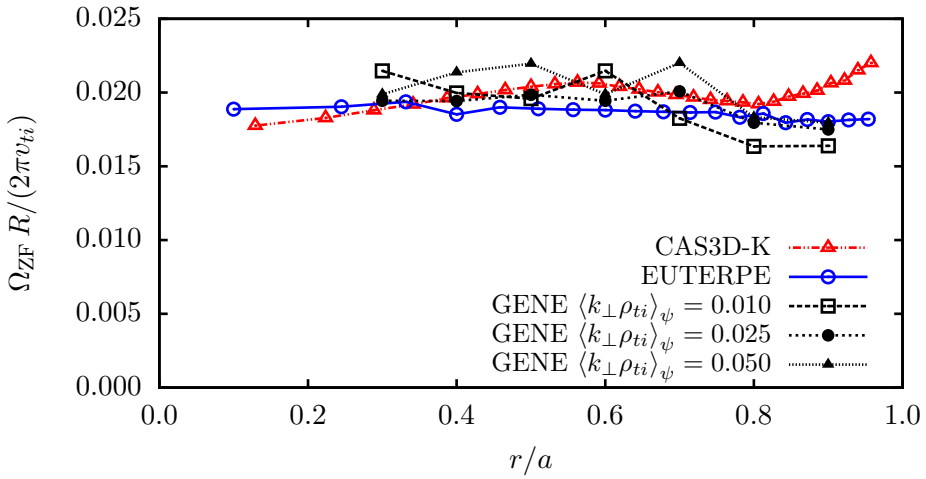

Figure 5.7: Zonal-flow frequency in the standard configuration of the W7-X stellarator obtained with CAS3D-K, EUTERPE and GENE. Several values of $\langle k_\perp \rho_{ti} \rangle_\psi$ are shown for GENE calculations. The EUTERPE calculations use $k_\psi = 0.5\pi$.

the zonal-flow frequency from the fitting method requires a careful analysis case by case.

5.2.1 W7-X stellarator: standard configuration

In this subsection we calculate the oscillation frequency in the standard configuration of the W7-X stellarator (W7-X SD). In the W7-X SD configuration the average magnetic field strength at the magnetic axis is $B_0 = 2.42$ T. The q profile of this configuration is given in figure 5.5. In the calculations presented here we use flat density and temperature profiles with $T_e = T_i = 5$ keV.

The calculations of the zonal-flow frequency with CAS3D-K, EUTERPE and GENE in the W7-X SD configuration are shown in figure 5.7. The oscillation frequency in all cases shows a rather flat radial profile and the agreement between them is very good. In the simulations carried out with EUTERPE we use an initial perturbation with $k_\psi = 0.5\pi$, so that the normalized radial scale of the perturbation varies radially, with $\langle k_\perp \rho_{ti} \rangle_\psi < 0.032$. Very similar values of the oscillation frequency were obtained in simulations with different (small) values of k_ψ (not shown here). Analogously, several simulations were carried out with GENE for different radial scales of the perturbation with $0.01 \leq \langle k_\perp \rho_{ti} \rangle_\psi \leq 0.05$ obtaining very similar values of the oscillation frequency (see figure 5.7). These results are in agreement with equation (2.66), which is independent of $k_\perp$ in the long-wavelength limit.

In the EUTERPE calculations, the error when obtaining the frequency

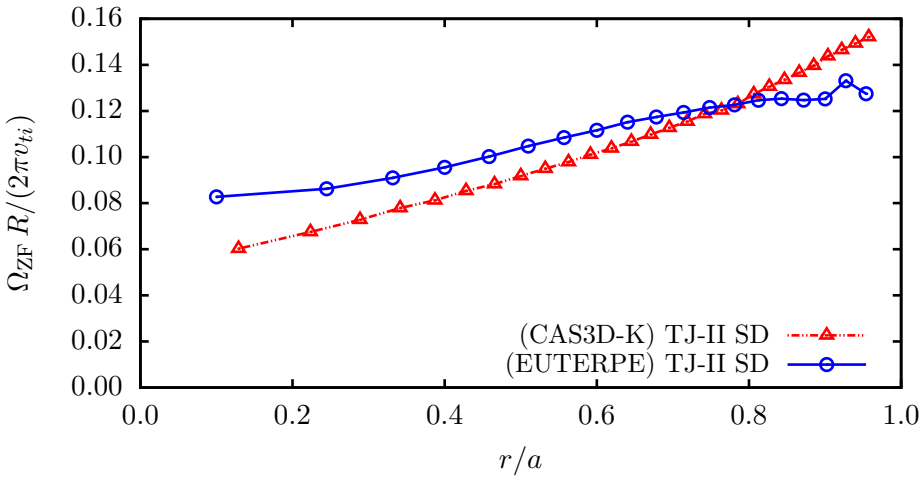

Figure 5.8: Calculation of the zonal-flow frequency in the standard configuration of the TJ-II stellarator obtained with CAS3D-K and EUTERPE. The radial scale of the initial perturbation in EUTERPE simulations is $k_\psi = 0.5\pi$.

is larger in the outer region of the plasma because the fit to the model function gives a less precise value. The treatment of lost particles at the outer boundary can also introduce some bias in the oscillation frequency. In the EUTERPE calculations an error on the order of a 20% of its value can be assumed in these radial positions. It is in these radial positions where the CAS3D-K calculation shows a significant increase in the frequency and the differences with the EUTERPE calculations are on the order of the error.

5.2.2 TJ-II stellarator

We have calculated the zonal flow oscillation frequency in the standard configuration of the TJ-II stellarator with CAS3D-K and EUTERPE. The q profile of this configuration is given in figure 5.5. We also use flat density and temperature profiles, in this case with temperatures $T_e = T_i = 100$ eV, close to typical ion temperature values in ECRH plasmas of TJ-II. In EUTERPE we use, as in the previous case, an initial perturbation with $k_\psi = 0.5\pi$, so that the normalized radial scale of the perturbation is $\langle k_\perp \rho_{ti} \rangle_\psi < 0.023$.

The results of the zonal-flow frequency calculated with CAS3D-K and EUTERPE for this configuration are shown in figure 5.8. As can be seen in this figure, the zonal-flow frequency in the TJ-II stellarator increases with the radial coordinate r/a and the calculations with the different numerical methods show a good agreement.

It is important to point out that in this configuration the calculation of Ω_{ZF} from the fit to the model function (4.10) is not as accurate as in the W7-X SD case because the damping of the low frequency oscillation is larger

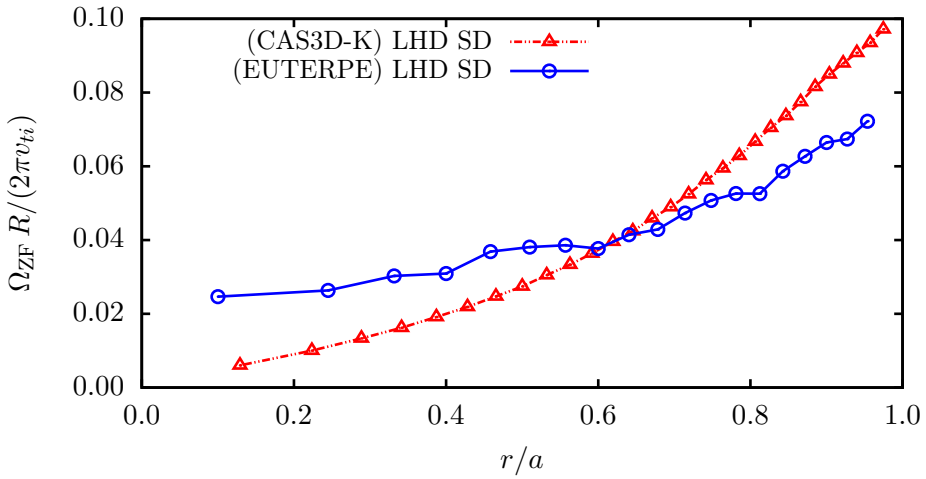

Figure 5.9: Zonal-flow frequency in the standard configuration of the LHD stellarator obtained with CAS3D-K and EUTERPE.

in TJ-II and fewer oscillation cycles are observed (see figure 5.6). However it can be calculated with reasonable accuracy from the EUTERPE electric field time traces for all radial positions because the initial GAM oscillation is quickly damped leaving a couple of cycles of neat zonal-flow low frequency oscillation. The first part of the time trace, in which the GAM oscillation is present, is not included in the fit.

5.2.3 LHD stellarator

In the LHD stellarator, we calculate the zonal-flow frequency in three magnetic configurations with different positions of the magnetic axis, $R_{\rm ax}$, and three different magnetic field strength at the magnetic axis, B_0. These are: the standard configuration (LHD SD) with $R_{\rm ax} = 3.74$ m and $B_0 = 2.53$ T; an outward-shifted configuration (LHD OS) with $R_{\rm ax} = 3.91$ m and $B_0 = 1.48$ T; and an inward-shifted configuration (LHD IS) with $R_{\rm ax} = 3.57$ m and $B_0 = 1.57$ T. The q profiles of these configurations are given in figure 5.5 and we take flat density and temperature profiles with $T_i = T_e = 5$ keV. In EUTERPE simulations we use an initial perturbation with $k_\psi = 0.5\pi$, so that the normalized radial scale of the perturbation is $\langle k_\perp \rho_{ti} \rangle_\psi < 0.018$.

The frequencies calculated with CAS3D-K and EUTERPE in the LHD SD configuration are shown in figure 5.9. Both calculations show a clear radial increase of the frequency. In this case, the agreement between calculations with CAS3D-K and EUTERPE cannot be expected to be optimal, as can be easily understood from a simple inspection of figure 5.6. This figure shows that the GAM oscillation is weakly damped and it is almost impossible to distinguish the low frequency oscillation. Therefore, in this configuration the

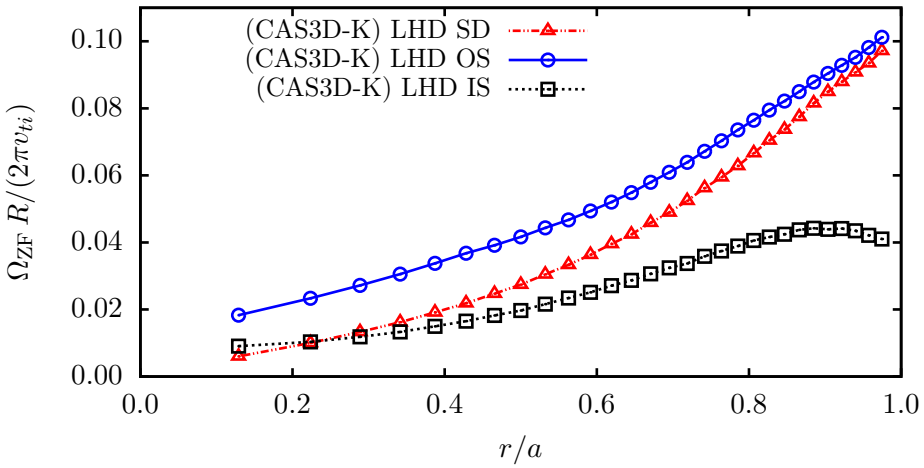

Figure 5.10: Zonal-flow frequency obtained with CAS3D-K in the LHD standard (LHD SD), outward-shifted (LHD OS) and inward-shifted (LHD IS) configurations.

fitting process turns out to be very complicated. In this sense, the agreement shown in figure 5.9 is actually remarkable.

In figure 5.10 we show the CAS3D-K calculations of the zonal-flow frequency in the LHD SD, LHD OS and LHD IS configurations. They also exhibit a radial increase of the frequency in all configurations, except for the LHD IS configuration in external radial positions, for $r/a > 0.9$. The inward-shifted configuration is better optimized for neoclassical transport, which has lower values of the averaged magnetic drift frequency, $\overline{\omega_s}$. This, at the same time, shows a larger value of the zonal-flow residual level (see reference [13]). As can be seen in figure 5.10, the frequency of the zonal-flow oscillation in the LHD IS configuration is smaller than in the LHD SD or LHD OS configurations, which is considered also a direct consequence of the reduction in $\overline{\omega_s}$.

We do not show the calculation of $\Omega_{\rm ZF}$ with EUTERPE in the IS and OS configurations of LHD because a fit to a model like (4.10) is not reliable. Basically, under the conditions chosen, the low-frequency oscillation is undetectable in the gyrokinetic simulations in these two configurations. The usefulness of calculating the zonal-flow oscillation frequency with CAS3D-K in the IS and OS configurations of LHD could be questioned in view that it is difficult to observe this oscillation in practice. However, this low frequency oscillation constitutes a natural mode of oscillation that could manifest under particular conditions that enhance it and/or diminish the GAM oscillation. Oscillations in this frequency range could, in principle, be excited by some forcing mechanism, such as fast ions or electrons, and might be measured.

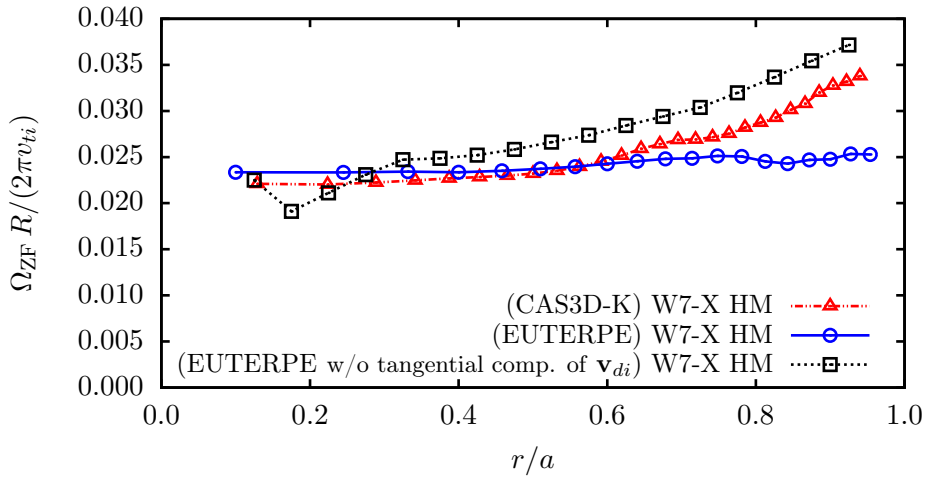

Figure 5.11: Zonal-flow frequency in the high-mirror configuration of the W7-X stellarator calculated with CAS3D-K and EUTERPE. The EUTERPE simulations employ $k_\psi = 0.5\pi$. As explained in the text, the EUTERPE simulations have been carried out in two settings: (a) including the full magnetic drift (blue curve); (b) retaining only the radial component of the magnetic drift (black curve).

With this idea in mind, the calculations shown in figure 5.10 could be useful even in this kind of configurations.

5.2.4 W7-X stellarator: high-mirror configuration

In figure 5.11 we show the values of $\Omega_{\rm ZF}$ for the high-mirror configuration of W7-X (W7-X HM) obtained with CAS3D-K (red line) and EUTERPE (blue line). In the calculations presented here we use, as in the W7-X SD case, flat density and temperature profiles with $T_e = T_i = 5$ keV. In the W7-X HM configuration the average magnetic field strength at the magnetic axis is $B_0 = 2.35$ T. The q profile is given in figure 5.5. In the EUTERPE simulations we use an initial perturbation with $k_\psi = 0.5\pi$, so that the normalized radial scale of the perturbation varies radially, with $\langle k_\perp \rho_{ti} \rangle_\psi < 0.032$.

The CAS3D-K and EUTERPE calculations are in very good agreement for $r/a < 0.6$, but not for $r/a > 0.6$. In this case the difference between calculations of CAS3D-K and EUTERPE seem too large to be attributed to fitting errors or boundary condition effects in the gyrokinetic simulations. Let us try to understand the disagreement.

Note that in equation (2.26) the component of the magnetic drift tangent to the flux surface has been neglected. This is formally correct as long as condition (2.20) is satisfied. We will see next, however, that in the W7-X HM configuration the neglected term contributes to the calculation of $\Omega_{\rm ZF}$. We

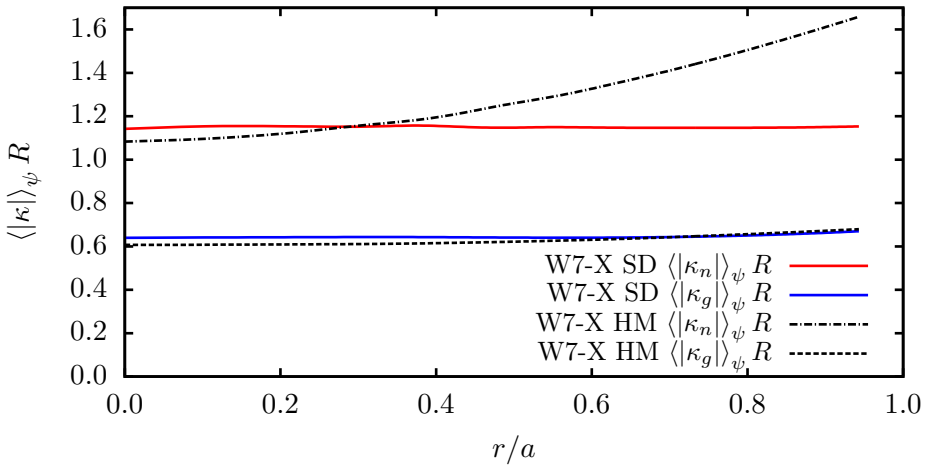

Figure 5.12: Flux-surface average of the absolute value of the geodesic and normal magnetic field line curvatures for the W7-X SD and W7-X HM configurations.

cannot easily extend the analytical calculation of Ω_{ZF} to include the effect of the tangential component of the magnetic drift, but we can carry out the EUTERPE simulations removing this component, and therefore leaving only the radial component of the magnetic drift, which is a more faithful comparison to (2.26).

The black curve in figure 5.11 corresponds to the EUTERPE simulation retaining only the radial component of the magnetic drift. In these simulations the damping of the low frequency oscillations increases significantly with respect to the cases in which the full magnetic drift is kept. This makes the fit to a damped oscillation model like (4.10) more difficult, but still possible. We can safely conclude that the role of the tangential magnetic drift in the W7-X HM configuration is needed to explain the radial dependence of Ω_{ZF} for $r/a > 0.6$.

The relevance of the tangential component of the magnetic drift in the W7-X HM configuration, by comparison to its irrelevance in the W7-X SD one, can be understood by looking at figure 5.12, where the flux-surface-averaged absolute value of the normal and geodesic components of the field line curvatures is shown for both configurations. While the geodesic component of the field line curvature is very similar in both cases, the normal component (related to the tangential component of the magnetic drift) is larger in the W7-X HM configuration than in the W7-X SD one. Actually, the difference is significant for $r/a \gtrsim 0.5$ and gets larger at outer positions (compare figure 5.12 with the black and blue curves in figure 5.11).

At this point, one might wonder why we do not do the same test for the

TJ-II and LHD SD configurations. That is, one might think that perhaps it is possible to prove that the agreement between CAS3D-K and EUTERPE simulations cannot be improved for TJ-II and LHD SD because the tangential component of the magnetic drift also counts in these configurations. However, this check turns out to be not feasible. In the simulations carried out neglecting the tangential component of the magnetic drift, the damping of the oscillations is remarkably higher with respect to the cases in which the full magnetic drift is retained. As we have already explained, in W7-X HM this effect is not enough to prevent a reasonable fit. On the contrary, in the rest of configurations studied (W7-X SD, TJ-II and LHD) the damping is so large when the tangential magnetic drift is removed that the fit is not reliable.

5.3 Simulation details and computational time

One of the most important features of the semianalytical method herein proposed for the evaluation of the zonal flow oscillation frequency is that it is faster than calculating it by means of gyrokinetic simulations with EUTERPE or GENE. We show in table 5.2 the total CPU time required to obtain the frequency with each method. The times shown in the table for CAS3D-K and GENE correspond to the time required for calculations at just one radial position, while for EUTERPE, as it is a global code, these values are given for the simulation of all radial positions at the same time. The values shown in table 5.2 are determined by the resolution used in the different cases with CAS3D-K and by the simulation time required to obtain a large enough number of oscillation cycles to make a fit in the case of EUTERPE and GENE. In the EUTERPE case, as they are global simulations, the minimum time required is determined by the most demanding radial position (the innermost radial locations, in general). These times represent the requirements for simulations or calculations converged with respect to the different numerical parameters and resolutions in each code. The numerical details in each case are listed below.

In CAS3D-K, the computation time to obtain converged results varies among devices and it depends on the phase-space resolution used in each case. The minimum resolution for the integration over the λ coordinate in all the calculations is $n_\lambda = 24$. The integration over the magnitude of the velocity is performed analytically. For the spatial integrals we use $n_\zeta = 128$ trajectories and $n_\theta = 512$ integration points per trajectory, in the case of passing particles. For trapped particles, these numbers are $n_\zeta = 16$ trajectories per integration group and $n_\theta = 512$ integration points per trajectory. The calculations in CAS3D-K are radially local. Therefore, the values in the table corresponding to CAS3D-K calculations are given per radial position and the ranges given in table 5.2 account for the maximum and minimum

	CAS3D-K	EUTERPE	GENE
LART (large ripple)	$3-4$	~ 2000	—
LART (small ripple)	$2-3$	~ 10000	—
W7-X SD	$2-3$	~ 2000	~ 180
W7-X HM	$2-3$	~ 2000	—
TJ-II SD	$3-4$	~ 1000	—
LHD SD, OS & IS	$1-3$	~ 3000	—

Table 5.2: CPU time (total core hours) required to obtain the zonal-flow frequency with CAS3D-K, EUTERPE and GENE in the magnetic configurations considered in this chapter. Note that the CAS3D-K and GENE calculations are radially local and the values in the table correspond to the time needed for the calculation at a single radial position. EUTERPE is radially global and the times in the table correspond to the full radius calculation.

CPU times among different radial positions at a given configuration.

The EUTERPE simulations presented here are not extremely demanding from a computational point of view as only the zonal ($(m,n)=(0,0)$ Fourier component) and several smaller amplitude sidebands are resolved. The simulations were carried out with the following numerical parameters. In all the cases the resolution in poloidal and toroidal angles in PEST coordinates was $n_{\theta_E}=32$ and $n_{\phi_E}=32$. The radial resolution was $n_{s_E}=24$ for the rippled tokamaks, TJ-II and LHD, while it was $n_{s_E}=32$ for the W7-X configurations. Simulations in W7-X were carried out with more radial resolution because several simulations with different radial scales of the perturbation, and maintaining the numerical parameters, were carried out for comparison. The number of markers used was $n_M = 40\text{M}-50\text{M}$.

In general, the EUTERPE calculations require larger computational resources for devices with lower zonal-flow frequencies as more simulation time is required to resolve a number of oscillation cycles that is large enough to make a fit. For the rippled tokamaks discussed in Section 5.1, the required computational time with EUTERPE increases by a factor of 5 for the case with smaller ripple with respect to that with the largest one because the oscillation frequency decreases by this factor, while all physical and numerical parameters in the simulation are the same. In the case of LHD configurations there is a large amplitude GAM oscillation, which makes difficult the fit of the potential time trace to a model like (4.10) for the low frequency oscillation, which has much smaller amplitude. A longer simulation time was required as compared to other configurations to obtain a reasonable fit in the LHD standard configuration. Only in the standard configuration of LHD a reliable fit of the potential time traces was possible.

The GENE calculations were performed employing its full flux-surface

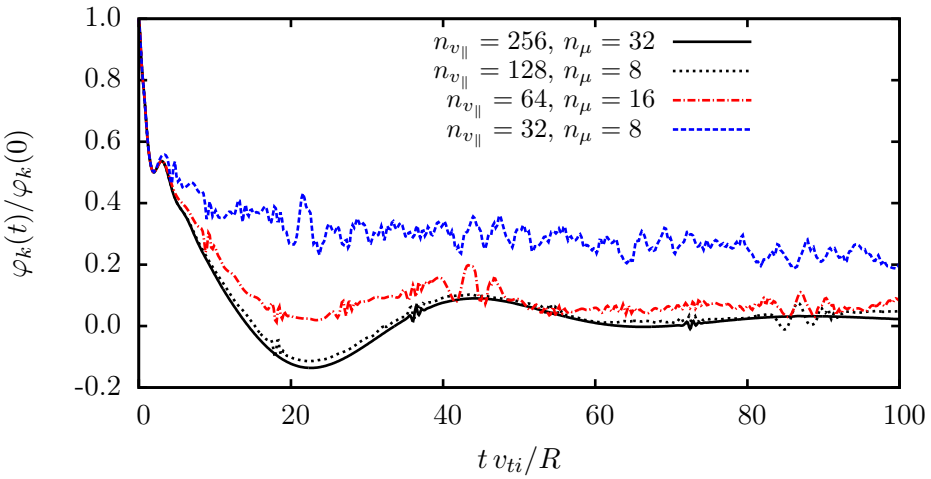

Figure 5.13: Time evolution of the electrostatic potential at $r/a = 0.5$ in the W7-X SD configuration obtained with GENE for different resolutions in velocity space. In all cases, the radial scale of the perturbation is the same, $\langle k_\perp \rho_{ti} \rangle_\psi = 0.05$.

version. Therefore, the calculations are 2D in the spatial coordinates $\{y, z\}$ and 2D in velocity space $\{v_\parallel, \mu\}$. Here, y is the coordinate along the binormal direction, z is the coordinate along the field line, $v_\parallel$ is the parallel velocity and μ is the magnetic moment coordinate. The results of the CPU time per radial position obtained with GENE in the W7-X SD configuration are given in table 5.2. An analysis of convergence in velocity space resolution was carried out and the results are shown in figure 5.13. In that figure, several electrostatic potential time traces at $r/a = 0.5$ are plotted, obtained from simulations with GENE in the W7-X SD configuration with $\langle k_\perp \rho_{ti} \rangle_\psi = 0.05$ and using different resolutions in velocity space. The CPU time given for GENE in table 5.2 corresponds to the simulation of figure 5.13 with $n_{v_\parallel} = 128$ and $n_\mu = 8$.

The calculations/simulations in this chapter were carried out in different supercomputers, with different capabilities, so that the computing time in the table 5.2 has to be considered as indicative. The EUTERPE simulations were carried out in two different supercomputers, EULER and MareNostrum III [62]. EULER is equipped with Intel Xeon 5450 quadcore processors at 3.0 GHz and Infiniband 4X DDR and Mare Nostrum III is equipped with Intel SandyBridge-EP processors at 2.6 GHz and Infiniband FDR10 interconnection. From 32 to 64 computing cores were used in the simulations. All the CAS3D-K calculations shown in this chapter were run also in the EULER supercomputer. The GENE calculations were carried out in the Uranus supercomputer, which is equipped with Intel Xeon E5-2630 processors at 2.4

GHz interconnected by Infiniband FDR. The computing time shown in the table is always the total CPU time (summed for all the computing cores used).

From the numbers shown in table 5.2, even corresponding to different computing facilities, it is clear that the calculations of the zonal-flow frequency with CAS3D-K are faster than those employing the gyrokinetic codes EUTERPE and Gene. This result strongly supports the usage of CAS3D-K in this type of computations.

5.4 Summary of results in this chapter

In this chapter, we have proven the efficiency of the semianalytical method for calculating the zonal flow oscillation frequency in stellarators and rippled tokamaks. It is based on the numerical evaluation of expression (2.66), which was first derived in [10] but had not been compared with the frequency obtained from gyrokinetic simulations so far.

We have used the extended version of CAS3D-K described in Chapter 3 for the evaluation of expression (2.66) in general rippled tokamak and stellarator configurations. The accuracy of this semianalytical approach was checked by comparing its results against the frequency obtained from gyrokinetic simulations with the global code EUTERPE and the radially local code Gene in a wide range of configurations. Specifically, we have calculated in a series of large aspect ratio tokamaks with different ripple values, as well as in the W7-X, TJ-II and LHD stellarators.

When using gyrokinetic codes, we obtain the zonal-flow frequency by fitting the time trace of the normalized zonal electrostatic potential (or electric field) to a model function, given in (4.10), including a damped oscillation and the decay to a residual value. The evolution of an initial zonal perturbation is initially dominated by a decaying GAM-like oscillation followed by a damped low frequency oscillation. Therefore, obtaining a precise value of the zonal-flow frequency from the fitting method is non-trivial, in general, and requires a case by case discussion.

The good agreement between the two methods (the semianalytical approach and the calculation of the frequency from gyrokinetic simulations) in real stellarator configurations supports the validity of the approximations in the derivation of (2.66) and the accuracy of the semianalytical approach via the extension of the CAS3D-K code. Only in the outer radial region of the high-mirror configuration of W7-X the accuracy of the semianalytical method is clearly insufficient. The reason is that, as we have explained, in this case, the tangential component of the magnetic drift, that is dropped in the analytical calculation leading to (2.66), must be kept.

The advantage of using CAS3D-K is that the computation time can be reduced up to two orders of magnitude with respect to the gyrokinetic cal-

culations. This makes this method an option to be included in an stellarator optimization loop, in which CAS3D-K could provide fast calculations of zonal flow relaxation properties (oscillation frequency and residual level [19]) to be used as figures of merit of stellarator configurations.

Chapter 6

Experimental evidence of the stellarator zonal-flow oscillation predicted theoretically

In this chapter, we present the first experimental evidence of the stellarator zonal flow oscillation. The experiments described in this chapter were carried out in the TJ-II stellarator, using the standard magnetic configuration. The injection of cryogenic hydrogen pellets produced a sudden perturbation to the density and the electrostatic potential of the plasma. The initial potential perturbation produced by the pellet ablation showed an oscillatory relaxation which is consistent with the theoretical model and the numerical calculations presented in Chapter 5. In this chapter, we review the experimental results and we show comparisons against numerical calculations with EUTERPE and semianalytical calculations with CAS3D-K. A large part of the content of this chapter can be found in Reference [18] which has been accepted for publication recently.

6.1 Experimental results

The hydrogen plasmas showed here were produced in the standard configuration of the TJ-II stellarator and heated by 30 kV neutral beam injection. TJ-II has four periods, an average field on axis of 0.96 T and edge rotational transform of 1.65. The discharges used here have line-averaged electron densities between $1 - 2.5 \times 10^{19}$ particles/m^3 and central electron and ion temperatures of 250 and 100 eV, respectively (note that, for these temperatures, the neutral beam-produced fast ions are slowed-down by Coulomb collisions with electrons). Typical profiles for these plasma conditions can

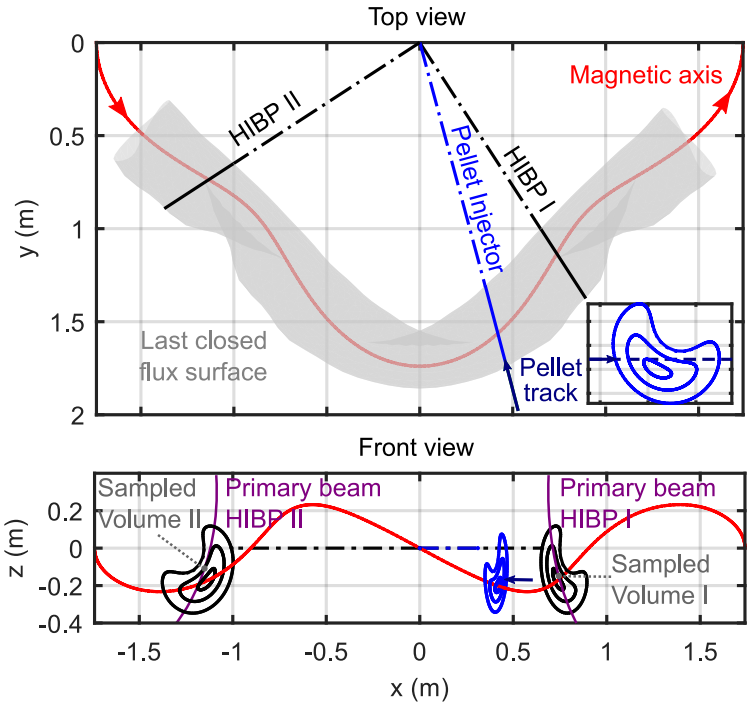

Figure 6.1: Schematic view of TJ-II magnetic geometry and experimental set-up. The positions of the pellet injection line and the two HIBP systems in equal cross-sections of two consecutive periods are shown. The upper plot shows a top view of one half of toroidal magnetic structure of the TJ-II stellarator. The magnetic axis is shown in red and a section of the last closed flux surface is shown in gray. The inset shows the cross section of several flux surfaces at the poloidal location of the pellet injector. These and the cross sections at the location of the HIBPs, are shown in a front view in the lower plot.

be found in [65, 66]. A cryogenic hydrogen pellet is injected into an otherwise effectively stationary phase of each discharge, causing a rapid change of the plasma parameters. The transient dynamics of the electric field that follows the pellet ablation is studied by means of two heavy ion beam probe (HIBP) systems [65, 67]. A schematic view of the setup showing the relative location of the pellet injection line and the two probing systems is presented in figure 6.1. The HIBP diagnostics were set to measure plasma potential at fixed points of the plasma cross section (termed "sampled volume" in figure 6.1) with spatial resolution of 1.5 cm and 2 MHz sampling rate.

Figure 6.2 shows several diagnostic signals in a 600 μs time window during a pellet injection. The ablation of the pellet, from its entry into the plasma until its complete ablation, is registered with silicon diodes that measure the line radiation (at 656.3 nm) emitted from the neutral cloud that surrounds

the pellet [68].

Pellets are injected with velocities of ∼1000 m/s and contain between 5×10^{18} and 10^{19} particles when condensed in the injector. Whereas the actual size of the pellets at first contact with the plasma edge varies, the estimated fueling efficiency is about 50%. The injections cause a prompt ∼10% reduction of the electron and ion temperatures as the pellet travels into the central plasma, and a ∼40% increase of the line-averaged plasma density. The central temperatures return to their previous levels after 5 ms, while the evolution of the line-averaged density is significantly slower (not shown in figure 6.2, see [65]). The plasma electric field undergoes a rapid evolution as observed with Doppler reflectometry in the plasma edge and the HIBP I and II in more interior positions (Fig. 6.2). The high time resolution and good signal-to-noise ratio of the beam probes allow to resolve a damped oscillation in the electrostatic potential transient response, qualitatively similar to the relaxation typically observed in numerical Rosenbluth-Hinton tests in three dimensional magnetic fields [10, 22].

6.2 Comparison of experimental results with numerical calculations

A direct comparison of the measured and simulated relaxation with EUTERPE is shown in Figure 6.3. The beginning of the simulation shows a quickly damped geodesic acoustic mode followed by the lower frequency damped oscillation as described in the previous chapter. In this case the plasma potential measurements are also fitted (after removing the very low frequencies, below 1 kHz) to a damped oscillation model described by equation (4.10), which is also shown in the figure to highlight the similarity with the result of the linear gyrokinetic simulation. The same model is used for the simulated time trace, thus obtaining pairs of experimental and simulated oscillation frequency, Ω_{ZF}, and damping rate, γ_{ZF}.

The experimental density and temperature profiles together with the background radial electric field, obtained with the drift-kinetic equation solver DKES [70], are used to define the equilibrium state. The ion and electron temperature profiles for some discharges are given in Figures 6.4 and 6.5, and the density profiles are given in Figure 6.6. In the EUTERPE calculations, the zonal component of the electrostatic potential at the flux surface of interest is monitored, which corresponds to the simulation values displayed in Figure 6.3. Both, collisionless and also collisional simulations have been carried out confirming that the oscillation frequency is basically determined by collisionless processes and not much affected by collisions, while the damping rate is largely dependent on the collisionality.

To systematize and quantify the comparison shown in Figure 6.3, values of the oscillation frequency and decay time are extracted from both the sim-

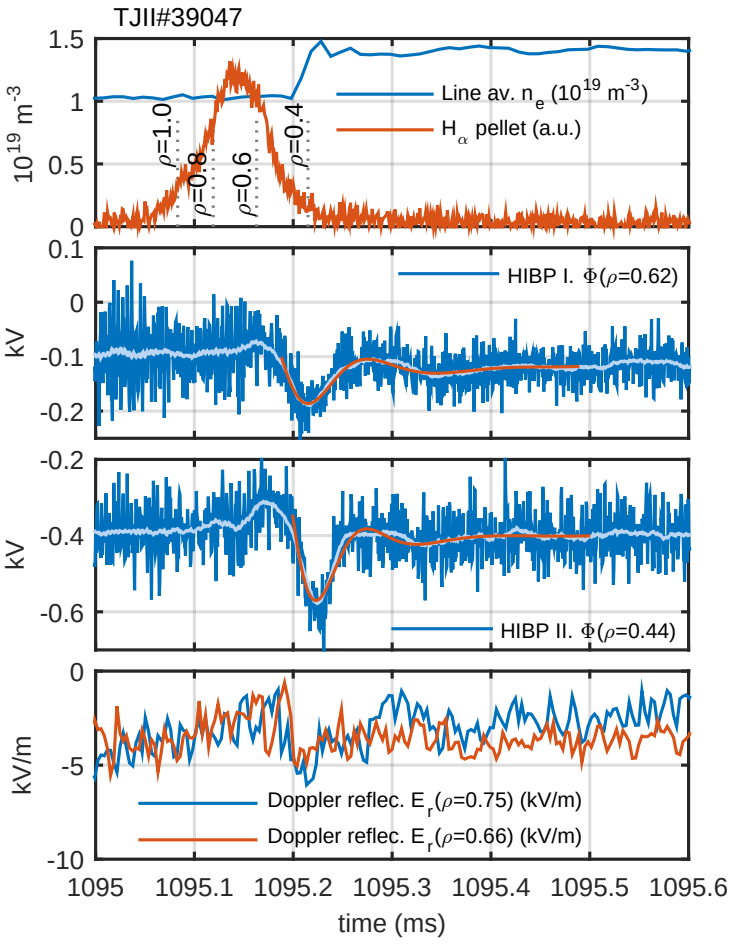

Figure 6.2: Evolution of plasma parameters following a pellet injection into the TJ-II stellarator. Top: line averaged electron density and H_α pellet monitor. Center: plasma electrostatic potential at two radial locations from the HIBP diagnostic. Bottom: radial electric field in two peripheral radial locations from Doppler reflectometry [69]. In the central plots, the smoothed HIBP signals are shown in lighter blue and fits to a model damped oscillation are shown in red.

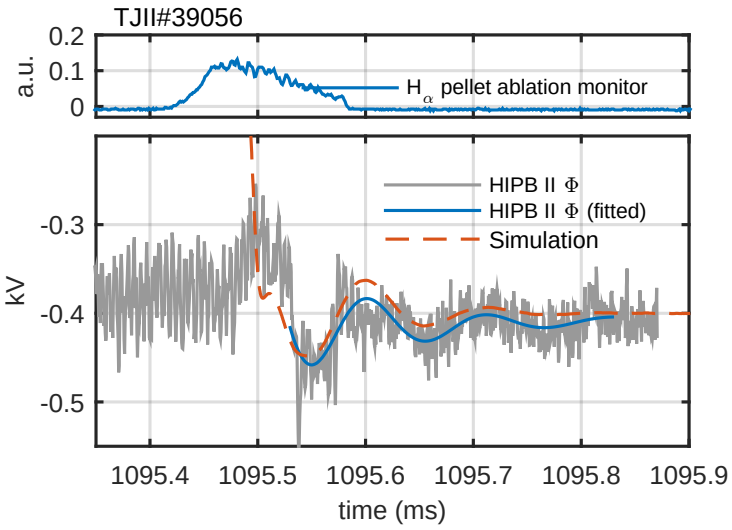

Figure 6.3: Time traces of the H_α ablation monitor in a pellet injection (top) and of the electrostatic potential in the gyrokinetic simulation and in a pellet-induced transient in the TJ-II stellarator (bottom).

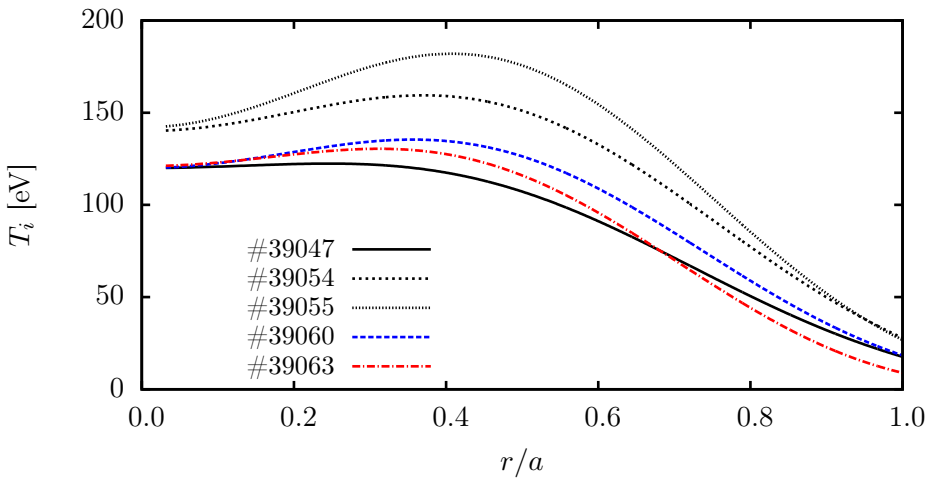

Figure 6.4: Ion temperature profiles of the discharges used in the numerical calculations with EUTERPE and CAS3D-K.

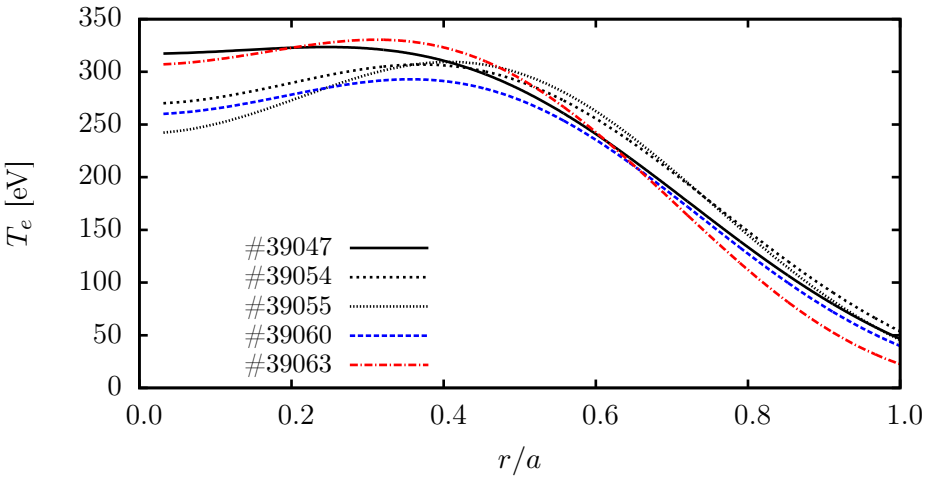

Figure 6.5: Electron temperature profiles of the discharges used in the numerical calculations with EUTERPE.

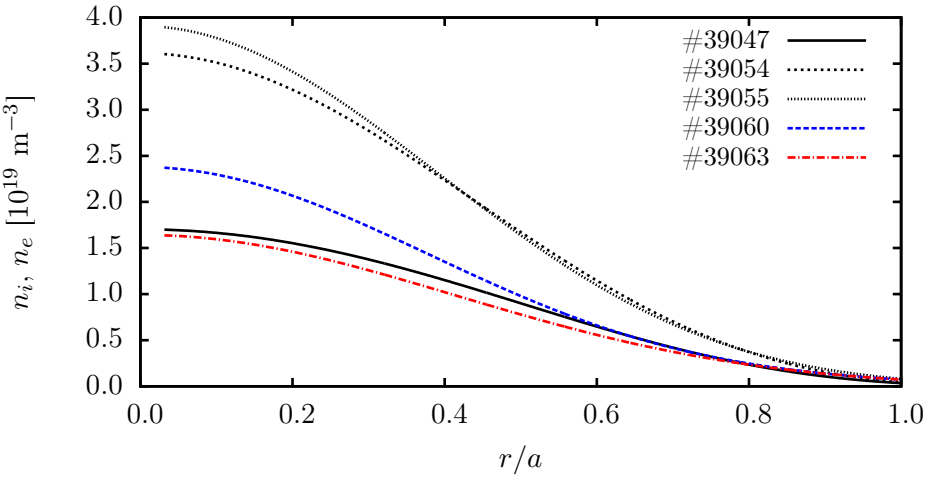

Figure 6.6: Ion and electron density profiles of the discharges used in the numerical calculations with EUTERPE.

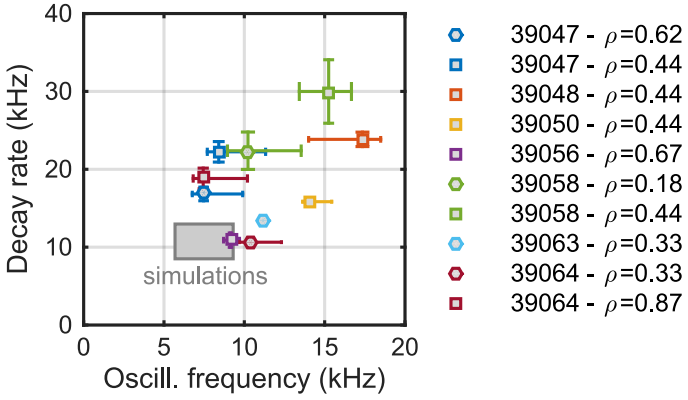

Figure 6.7: Comparison of measured and simulated oscillation frequencies and damping rate for several discharges and radial positions. Measurements obtained with the HIBP I and II are labeled with circles and squares receptively. The gray rectangle encompasses the values obtained from the simulated zonal potential relaxation for several radii in the rage $0.3 \leq \rho \leq 0.9$ and five different experimental profile sets representative of the discharges.

ulated and measured damped oscillation. This is done for the database of pellet injections in which a damped oscillation is visible. We note that not all pellet injections cause a measurable oscillation in the HIBP potentials, which is attributed to the imperfect reproducibility of the pellet and the different target plasma conditions. The results are presented in Figure 6.7, with error bars corresponding to 95% confidence level in the estimation of the frequency and damping rate. The magnitude of the relative uncertainty in the fitted parameters being less than 20% was the acceptance criteria for the points in this plot. The rectangle covers the same confidence level for the parameters extracted from the decays simulated for several experimental discharges and the range of radial positions of experimental measurements. Simulations were carried out for five plasma discharges of the series for which density and temperature profiles were available. The agreement between the parameters of the simulated and measured relaxations is reasonable. In general, both the simulated damping rate and oscillation frequency show a shift towards smaller values compared to the measurement. Oscillation frequency displays a better agreement (within a factor of 2) and less dispersion than the damping rates. We note that the former, which is essentially determined by collisionless mechanisms, is expected to be less affected by the uncertainties in the local plasma parameters and plasma composition [71] as compared to the latter.

Now, we turn to compare the zonal-flow frequency obtained with gyrokinetic simulations and our semianalytical method. In this case, we carry out

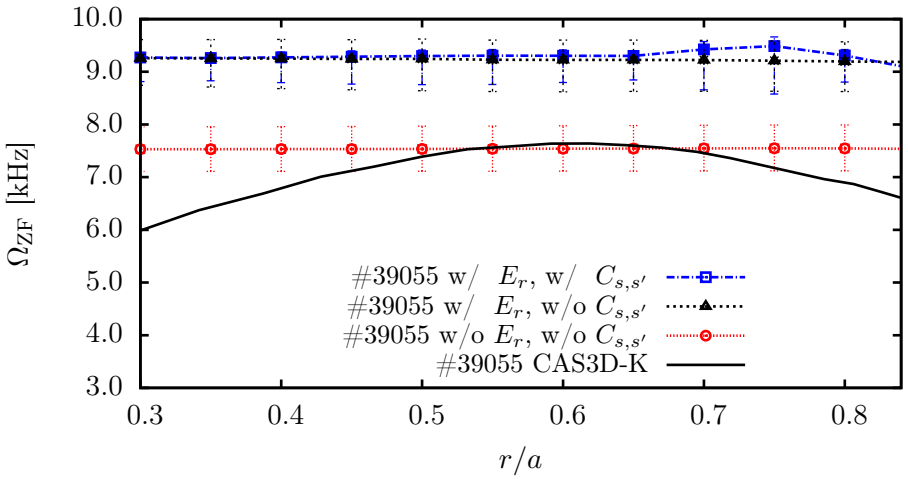

Figure 6.8: Calculations of the zonal-flow frequency in the discharge #39055 obtained with CAS3D-K and with EUTERPE under three conditions: with collisions and radial electric field, E_r; without collisions but with E_r; and without collisions and E_r.

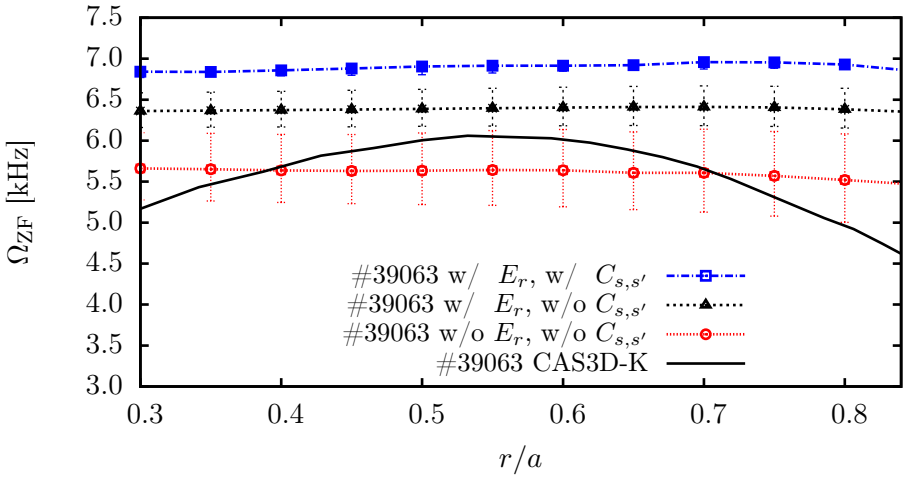

Figure 6.9: Same as in Figure 6.8 but for discharge #39063.

EUTERPE simulations under three conditions; with collisions and radial electric field, E_r; without collisions but with E_r; and without collisions and E_r. For these calculations we use the temperature and density profiles given in Figures 6.4, 6.5 and 6.6. The results obtained for the discharge #39055 are given in Figure 6.8 and those for discharge #39063 are shown in Figure 6.9 as examples. Note that in Figure 6.9 the calculations for the case including electric field and collisions (blue line in the figure) do not show error bars. The oscillation fitting is more difficult in cases with an extra damping due to collisions, so that the fit algorithm could not estimate the confidence margin. An error around 7% in the frequency, similar to that in Figure 6.8, can be expected in this case.

In its actual state, the CAS3D-K calculations contain the information on how the magnetic configuration affects the zonal-flow frequency but do not take into account other properties of the plasma that have been considered in the EUTERPE calculations such as the radial electric field, collisions and relatively large temperature and density gradients. As can be seen in Figures 6.8 and 6.9, the agreement between CAS3D-K and EUTERPE is better in the central radial positions. The CAS3D-K calculations shown in these figures have been performed with the same magnetic configuration as those shown in Section 5.2.2, the only difference being the temperature and density profiles. In Figure 5.8 the CAS3D-K calculations gave smaller values for the frequency than EUTERPE for a wide range of radial locations ($r/a < 0.8$) while the CAS3D-K frequency was larger for $r/a > 0.8$. Interestingly, in the cases shown in Figures 6.8 and 6.9 the CAS3D-K calculations give slightly smaller frequency values than EUTERPE for $r/a > 0.7$. It seems reasonable that density and temperature gradients, which are larger in the outer region of the plasma, play a role in the zonal-flow relaxation which is not taken into account in CAS3D-K and could explain the change in tendencies as compared to Figure 5.8. We leave for future work the implementation and the study of the effect of the radial electric field, collisions and temperature and density gradients with CAS3D-K.

6.3 Summary of results in this chapter

In conclusion, we have presented measurements of zonal electrostatic potential relaxation in pellet-induced fast transients which are consistent with the theoretical expectations and with gyrokinetic simulations. The results shown in this chapter are important in as much as the non-linear turbulence saturation level and heat transport coefficients in stellarators depend on the features of the collisionless damping of zonal electrostatic potential perturbations, of which the present results are the first direct observation.

Semianalytical calculations are provided to compare against those obtained with EUTERPE. The agreement between these calculations is better

when collisions and radial electric field are not considered in EUTERPE, and it is better around $r/a = 0.5$. Since collisions, radial electric field, and large density and temperature gradients are not considered in CAS3D-K we identify them as the relevant effects that explain the moderate disagreement between EUTERPE and CAS3D-K. We leave for future work the implementation and study of these effects with CAS3D-K.

The methodology and observations presented here could be reproduced, in principle, in the Wendelstein 7-X stellarator, whose magnetic configuration and low collisionality plasma conditions might allow an even clearer observation of this phenomenon.

Chapter 7

Conclusions

In this thesis, we have studied in detail several properties of the relaxation process of zonal flows in tokamaks and stellarators. Namely, the residual zonal-flow level and the zonal-flow oscillation frequency. A numerical tool for the evaluation of these quantities has been developed and its results have been compared systematically against other numerical calculations with gyrokinetic codes and analytical results. This tool has proven to be much faster that gyrokinetic simulations, specially in stellarator devices.

In Chapter 2, we have treated analytically the linear and collisionless evolution of zonal flows as an initial value problem, and derived expressions for the residual value that are valid for arbitrary wavelengths and for tokamak and stellarator geometries. In particular, we have developed further the theory of the residual zonal-flow level in stellarators to allow for short wavelengths. In this chapter, we have also given the derivation of the expression for the zonal-flow oscillation frequency.

The expressions derived in Chapter 2 involve certain averages in phase-space and the solution of magnetic differential equations that cannot be evaluated analytically, except for simplified geometries. For this purpose, in Chapter 3, we have explained the extensions that we have implemented into the code CAS3D-K to perform the evaluation of such expressions. More specifically, we have included the integration over the velocity coordinates v and σ, the solution to the magnetic differential equations to obtain the relevant finite orbit-width effects and the implementation of the finite Larmor radius effects through Bessel-related functions. We have tested the extension of the code by comparing its results with analytical formulae available in the literature and with gyrokinetic simulations.

In Chapter 4, we have computed the residual zonal-flow level in tokamak and stellarator geometries for a wide range of radial wavelengths, using both the approximation of adiabatic electrons and fully kinetic species. We have compared the results of CAS3D-K with those obtained from two gyrokinetic codes: the global code EUTERPE an the radially local version of GENE.

These comparisons show a very good agreement. We also show that CAS3D-K can be useful to evaluate fast and accurately the residual level, up to three orders of magnitude faster, and to perform benchmarks in stellarator geometry. The fact that in stellarators the adiabatic electron approximation gives incorrect zonal flow residuals, even at long wavelengths, has been discussed in detail and confirmed by means of gyrokinetic simulations.

In Chapter 5, we showed calculations of the zonal-flow oscillation frequency in toroidal devices. Specifically, we have calculated the zonal-flow frequency in a series of large aspect ratio tokamaks with different ripple values and in the W7-X, TJ-II and LHD stellarators. The accuracy of the semianalytical method was checked by comparing its results against those obtained with the global code EUTERPE and, when possible, with the radially local version of GENE. These are the first comparisons between a semianalytical method and gyrokinetic simulations. When using gyrokinetic codes, we obtain the zonal-flow frequency by fitting the time trace of the normalized zonal electrostatic potential to a model function which includes a damped oscillation and a decay to the residual value. We have shown that this fitting method is non-trivial, in general, as the time evolution of the electrostatic potential is composed of a GAM oscillation on top of that of the zonal-flow. Therefore, obtaining a precise value of the zonal-flow frequency from this method is not always possible. In these cases, the CAS3D-K calculations prove to be very useful as the code solves only the zonal contribution to the frequency.

In Chapter 6 we show the first experimental evidence of the zonal electrostatic potential relaxation, measured recently in the TJ-II stellarator. These measurements are compared with the theoretical calculations (using the methods described in Chapter 5). These comparisons show to be in good agreement, supporting the validity of the theoretical predictions of the zonal-flow frequency.

Appendix A

Magnetic differential equations

In this appendix, we give the solution δ_s to the magnetic differential equation (2.29). We use Boozer coordinates. That is, we assume that $\{\psi, \theta, \zeta\}$ are such that the contravariant form of $\mathbf{B}$ is given by (2.1), and its covariant form is given by

$$\mathbf{B} = I_t \nabla\theta - I_p \nabla\zeta + \widetilde{\beta}\,(\psi, \theta, \zeta)\,\nabla\psi. \tag{A.1}$$

The square root of the metric determinant is $\sqrt{g} = (I_t \Psi_p' - I_p \Psi_t')/B^2$. Here, $I_t = I_t(\psi)$ and $I_p = I_p(\psi)$ are the toroidal and poloidal currents, respectively. In Boozer coordinates, the radial magnetic drift reads

$$\omega_s = -\frac{1}{\tau_b \Psi_p'}\left[I_p \partial_\theta + I_t \partial_\zeta\right] \rho_{\|s}. \tag{A.2}$$

The parallel gyroradius is defined as $\rho_{\|s} = v_\| / \Omega_s$, whereas $\tau_b = B\sqrt{g}/(v_\| \Psi_p')$.

A.1 Magnetic differential equation for passing particles

For passing particles, $\overline{\omega_s} = 0$. The magnetic differential equation to be solved is then given by

$$v_\| \hat{\mathbf{b}} \cdot \nabla \delta_s = \omega_s, \tag{A.3}$$

which in Boozer coordinates becomes

$$\left(\Psi_p' \partial_\theta + \Psi_t' \partial_\zeta\right) \delta_s = -\left(I_p \partial_\theta + I_t \partial_\zeta\right) \rho_{\|s}. \tag{A.4}$$

This equation is easily solved in Fourier space, giving

$$\delta_s = C - \sum_{m,n \neq 0} \left[\frac{m I_p + n I_t}{m \Psi_p' + n \Psi_t'}\right] (\rho_{\|s})_{mn} \mathrm{e}^{2\pi \mathrm{i}(m\theta + n\zeta)}, \tag{A.5}$$

where the coefficients $(\rho_{\|s})_{mn}$ are defined by

$$\rho_{\|s} = \sum_{m,n} (\rho_{\|s})_{mn} \mathrm{e}^{2\pi \mathrm{i}(m\theta + n\zeta)} \tag{A.6}$$

and C is a constant. The solution is found by choosing the integration constant as $C = -I_p(\rho_{\|s})_{00}/\Psi_p'$, which gives

$$\delta_s = -\frac{I_p}{\Psi_p'} \left[\rho_{\|s} + \left(\frac{I_t}{qI_p} - 1 \right) \sum_{m,n\neq 0} \left(\frac{qn}{m+qn} \right) (\rho_{\|s})_{mn} \mathrm{e}^{2\pi \mathrm{i}(m\theta + n\zeta)} \right]. \tag{A.7}$$

This solution, already given in [10], is valid for any toroidal geometry. For tokamaks, it reduces to $\delta_s = -I_p\, \rho_{\|s}/\Psi_p'$.

A.2 Magnetic differential equation for trapped particles

For trapped particles, the magnetic differential equation is given by

$$v_\| \hat{\mathbf{b}} \cdot \nabla \delta_s = \omega_s - \overline{\omega_s}. \tag{A.8}$$

In coordinates $\{\psi, \theta, \alpha\}$, with $\alpha = \zeta - q\theta$ (and $\{\psi, \theta, \zeta\}$ being Boozer coordinates), one has

$$\omega_s = -\frac{1}{\tau_b \Psi_p'} \left[I_p \partial_\theta + (I_t - qI_p)\partial_\alpha \right] \rho_{\|s}, \tag{A.9}$$

and equation (A.8) then reads

$$\tau_b^{-1} \partial_\theta \left(\frac{I_p}{\Psi_p'} \rho_{\|s} + \delta_s \right) = \widetilde{\omega}_{s\alpha}, \tag{A.10}$$

where

$$\widetilde{\omega}_{s\alpha} := \frac{qI_p - I_t}{\Psi_p'} \left[\tau_b^{-1} \partial_\alpha \rho_{\|s} - \overline{\tau_b^{-1} \partial_\alpha \rho_{\|s}} \right]. \tag{A.11}$$

The coordinate along the magnetic field line, θ, is not monotonic over the periodic orbit delimited by the bounce points θ_{b_1} and θ_{b_2}. We define a monotonic coordinate τ by

$$\tau := \begin{cases} \int_{\theta_{b_1}}^{\theta} |\tau_b| \, \mathrm{d}\theta' & \text{when} \quad \sigma > 0 \\ \widehat{\tau}_b/2 - \int_{\theta_{b_2}}^{\theta} |\tau_b| \, \mathrm{d}\theta' & \text{when} \quad \sigma < 0, \end{cases} \tag{A.12}$$

with

$$\widehat{\tau}_b = 2\int_{\theta_{b_1}}^{\theta_{b_2}} |\tau_b|\,\mathrm{d}\theta. \tag{A.13}$$

Then, the solution of (A.10) can be easily written in integral form as

$$\delta_s = -\frac{I_p}{\Psi_p'}\rho_{\|s} + \int_0^{\tau} \widetilde{\omega}_{s\alpha}\mathrm{d}\tau'. \tag{A.14}$$

Another solution for (A.14) using an expansion in bounce harmonics. This can be found by using the periodicity in τ by writing

$$\widetilde{\omega}_{s\alpha} = \sum_{l\neq 0} (\omega_{s\alpha})_l\, \mathrm{e}^{\mathrm{i}l\widehat{\omega}_b\tau}, \tag{A.15}$$

with $\widehat{\omega}_b := 2\pi/\widehat{\tau}_b$ and

$$(\omega_{s\alpha})_l = (\widehat{\tau}_b/2)^{-1}\int_0^{\widehat{\tau}_b/2} \omega_{s\alpha}(\tau)\cos\left(l\widehat{\omega}_b\tau\right)\mathrm{d}\tau. \tag{A.16}$$

Here, the fact that $\omega_{s\alpha}(\tau)$ is even in τ has been employed. Finally, we can write

$$\delta_s = -\frac{I_p}{\Psi_p'}\rho_{\|s} + 2\sum_{l>0}\frac{(\omega_{s\alpha})_l}{l\,\widehat{\omega}_b}\sin\left(l\,\widehat{\omega}_b\tau\right). \tag{A.17}$$

Note that for tokamaks (A.17) simply gives $\delta_s = -I_p\rho_{\|s}/\Psi_p'$ and this expression coincides with that for passing particles.

Appendix B

Power series expansions of some functions at long wavelengths

In this appendix, we present the power series expansions used throughout the thesis. At the end of this section we comment on the validity of these expansions and their relation with the zonal-flow initial condition at long wavelengths.

The relevant finite Larmor radius effects are contained in the Bessel-related functions $J_0(k_\perp\rho_s)$, the zeroth order Bessel function of the first kind, and the Gamma function $\Gamma_0(k_\perp^2\rho_{ts}^2)$, which is defined as

$$\Gamma_0\left(k_\perp^2\rho_{ts}^2\right) := \exp\left(-k_\perp^2\rho_{ts}^2\right) I_0\left(k_\perp^2\rho_{ts}^2\right), \tag{B.1}$$

where $I_0(k_\perp^2\rho_{ts}^2)$ is the zeroth-order modified Bessel function of the first kind. In the long-wavelength approximations $k_\perp\rho_s \sim k_\perp\rho_{ts} \ll 1$, the power series expansions of these Bessel-related functions can be written as

$$J_0(k_\perp\rho_s) = 1 - \frac{(k_\perp\rho_s)^2}{4} + \frac{(k_\perp\rho_s)^4}{64} + O((k_\perp\rho_s)^6), \tag{B.2}$$

$$J_0^2(k_\perp\rho_s) = 1 - \frac{(k_\perp\rho_s)^2}{2} + \frac{3\,(k_\perp\rho_s)^4}{32} + O((k_\perp\rho_s)^6) \tag{B.3}$$

and

$$\Gamma_0\left((k_\perp\rho_{ts})^2\right) = 1 - (k_\perp\rho_{ts})^2 + \frac{3(k_\perp\rho_{ts})^4}{4} + O((k_\perp\rho_{ts})^6). \tag{B.4}$$

Therefore, using these power series expansions, the expression of the zonal-flow initial condition (2.56) for long wavelengths reads

$$f_s^{\mathrm{lw}}(0) = \frac{Z_s e}{T_s}\left\langle k_\perp^2\rho_{ts}^2\right\rangle_\psi F_{s0}\,\varphi_k(0). \tag{B.5}$$

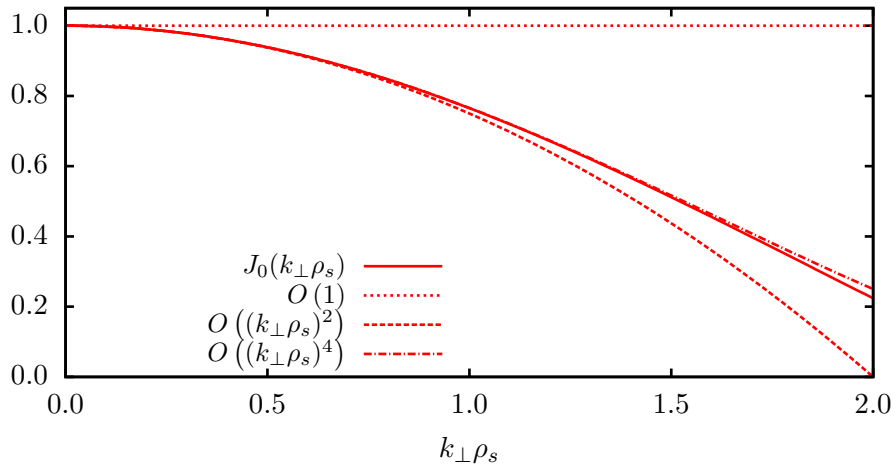

Figure B.1: Plot of $J_0(k_\perp \rho_s)$ and its power series expansions (B.2) keeping terms up to orders $O(1)$, $O((k_\perp \rho_s)^2)$ and $O((k_\perp \rho_s)^4)$.

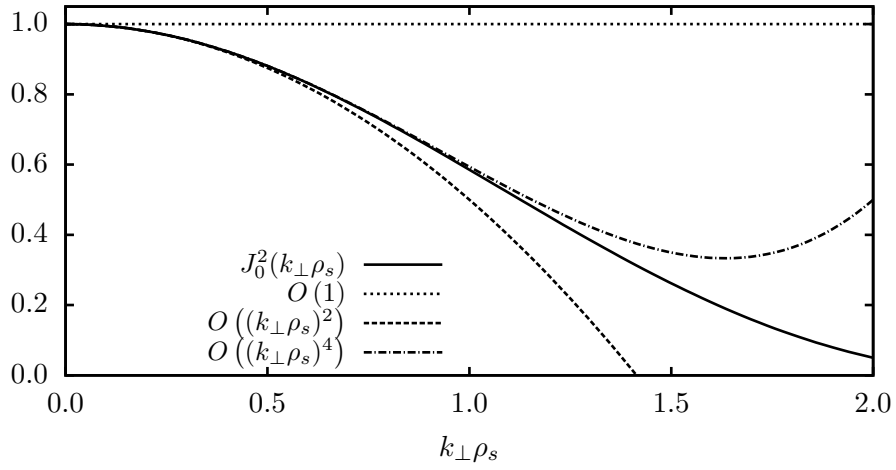

Figure B.2: Plot of $J_0^2(k_\perp \rho_s)$ and its power series expansions (B.3) keeping terms up to orders $O(1)$, $O((k_\perp \rho_s)^2)$ and $O((k_\perp \rho_s)^4)$.

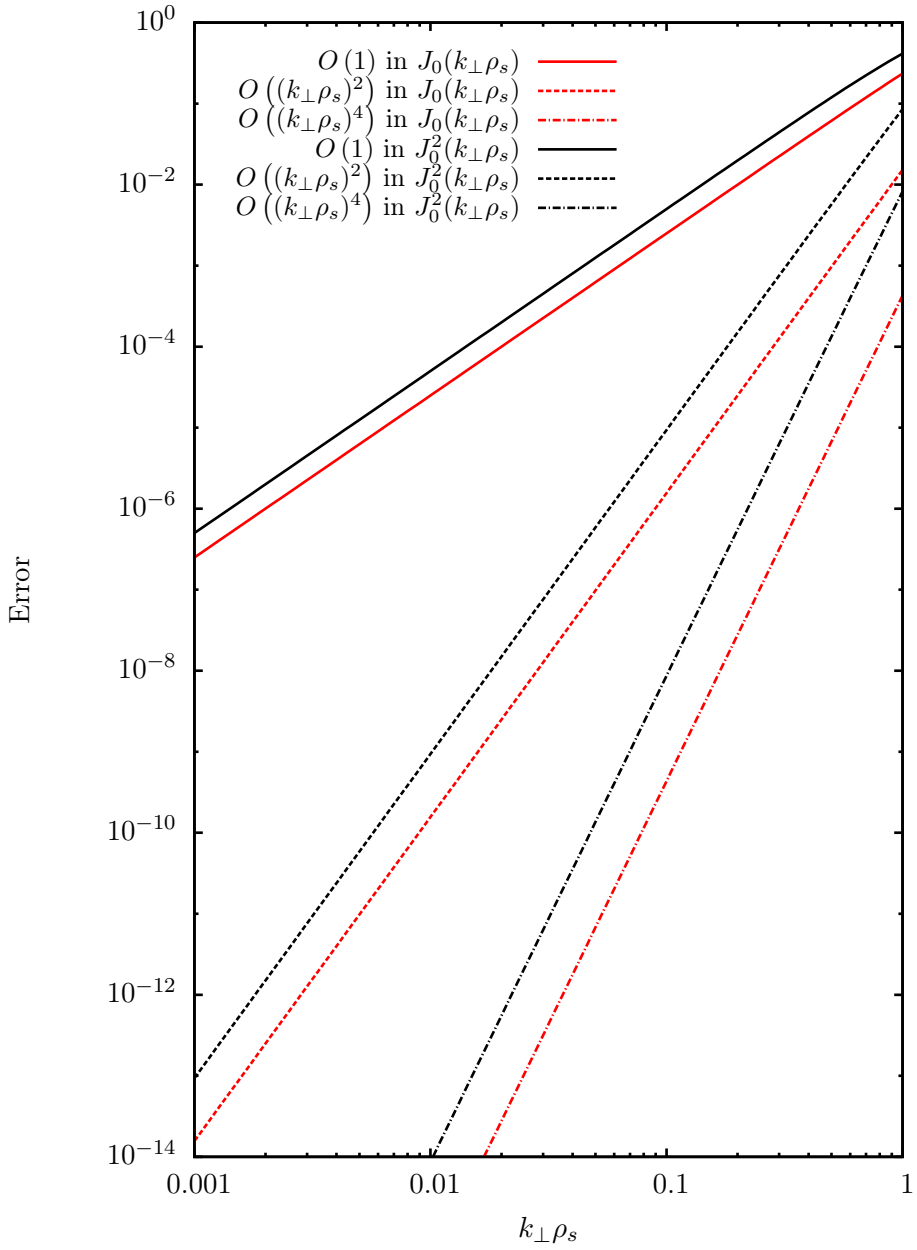

Figure B.3: Error in the power series expansion of the functions $J_0(k_\perp\rho_s)$ and $J_0^2(k_\perp\rho_s)$ when keeping terms up to orders $O(1)$, $O((k_\perp\rho_s)^2)$ and $O((k_\perp\rho_s)^4)$.

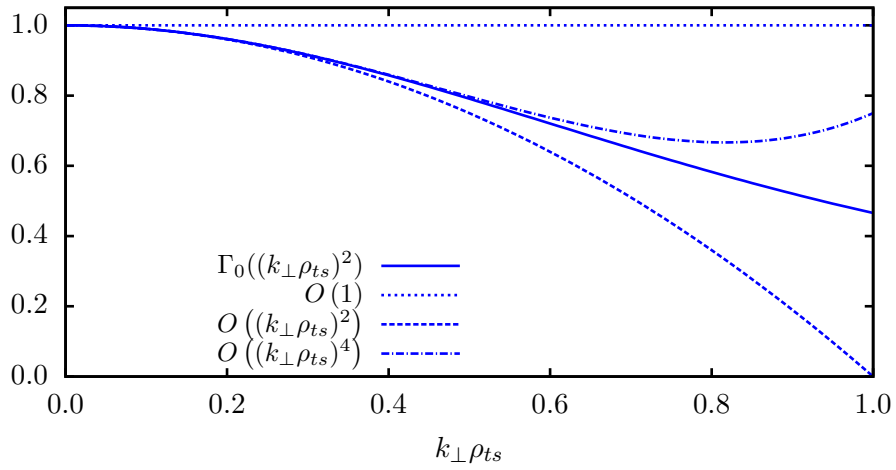

Figure B.4: Plot of $\Gamma_0\left(k_\perp^2\rho_{ts}^2\right)$ and the power series expansions for different orders in $k_\perp\rho_{ts} \ll 1$, as in equation (B.4).

Note that, all the gyrokinetic simulations with EUTERPE shown in this work have been initialized using this initial condition.

The finite orbit-width effects are encoded in δ_s, defined as the radial displacement of the particle's gyrocenter from their mean surface. In the equation that describes the residual zonal-flow, these effects are contained in the complex exponentials $\exp(\pm \mathrm{i} k_\psi \delta_s)$. The power series expansion of these exponentials for $k_\psi \delta_s \ll 1$ read

$$\mathrm{e}^{\pm \mathrm{i} k_\psi \delta_s} = 1 \pm \mathrm{i} k_\psi \delta_s - \frac{(k_\psi \delta_s)^2}{2} \mp \mathrm{i} \frac{(k_\psi \delta_s)^3}{6} + \frac{(k_\psi \delta_s)^4}{24} + O((k_\psi \delta_s)^5). \quad \text{(B.6)}$$

B.1 Validity range of the power series expansions

Throughout this work, we have employed the power series expansions given in equations (B.2), (B.3) and (B.4). We devote this section to analyze in more detail the estimation of the range of validity of these expansions. In this thesis, only expansion keeping terms up to order 2 of these functions have been required.

In figure B.1, we show a plot of the Bessel function $J_0(k_\perp\rho_s)$ and the power series expansions keeping terms up to orders $O(1)$, $O((k_\perp\rho_s)^2)$ and $O((k_\perp\rho_s)^4)$, as described in equation (B.2). Equivalently, we plot in figure B.2 the $J_0^2(k_\perp\rho_s)$ function as in (B.3) for the same orders. The error when using these approximations is shown in figure B.3. As can be seen in this figure, in the case of $J_0(k_\perp\rho_s)$, the error when using terms up to $O((k_\perp\rho_s)^2)$ is smaller than 1% for $k_\perp\rho_s \lesssim 0.9$. In $J_0^2(k_\perp\rho_s)$, this value of the error is achieved for wavelengths with $k_\perp\rho_s \lesssim 0.6$.

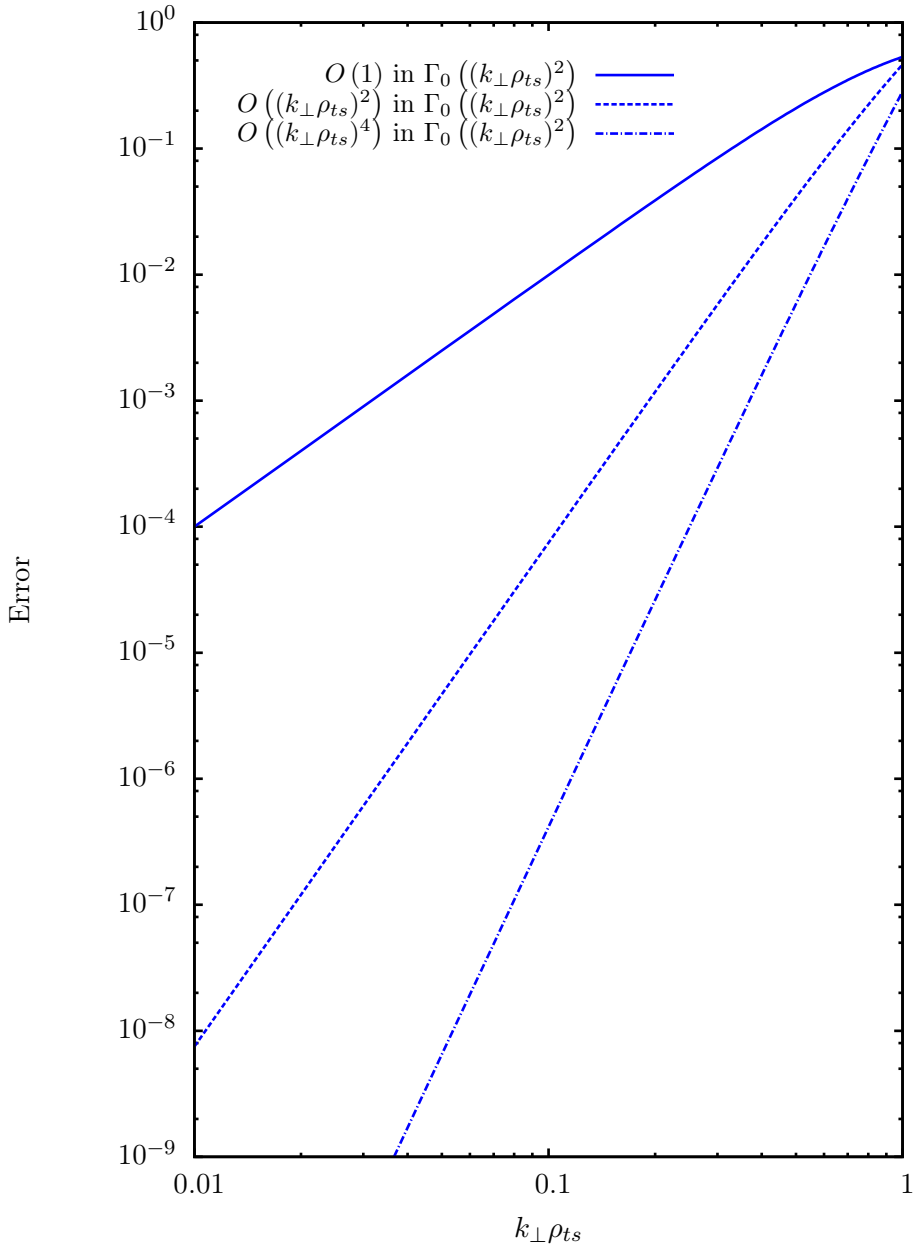

Figure B.5: Error in the power series expansion of $\Gamma_0\left(k_\perp^2\rho_{ts}^2\right)$ when keeping terms up to orders $O(1)$, $O((k_\perp\rho_{ts})^2)$ and $O((k_\perp\rho_{ts})^4)$.

The power series expansions of the Gamma function $\Gamma_0\left(k_\perp^2\rho_{ts}^2\right)$ keeping terms up to orders $O(1)$, $O((k_\perp\rho_{ts})^2)$ and $O((k_\perp\rho_{ts})^4)$, as described by equation (B.4), are shown in figure B.4. A plot of the error when using these approximations are given in figure B.5. It is clear from this figure that the error is larger than those for the Bessel functions, as shown in figure B.3. In particular, the error when using terms up to $O((k_\perp\rho_s)^2)$ is smaller than 1% for $k_\perp\rho_{ts} \lesssim 0.35$, and smaller that 5% for $k_\perp\rho_{ts} \lesssim 0.52$.

In view of the results shown in this section, an error smaller than 1% in the long-wavelength approximation of the initial condition (B.5) could be achieved for wavelengths up to $k_\perp\rho_{ts} \sim 0.35$ when calculating with EUTERPE. In practice, this value appears to be consistent in tokamaks as shown in Section 4.2.1 (see for example the EUTERPE results shown in figure 4.7). In stellarators, the long-wavelength approximation of the initial condition shows to be valid for wavelengths up to $k_\perp\rho_{ts} \sim 0.7$. This is shown in Section 4.2.2 (see figures 4.6 and 4.10). In Chapter 5, the long-wavelength approximations described in this appendix were used in the derivation of the zonal-flow oscillation frequency. All the calculations shown in that chapter have been performed for wavelengths with $k_\perp\rho_{ts} \leq 0.05$.

List of Figures

List of Tables

Bibliography

[1] W. Horton. Drift waves and transport. *Rev. Mod. Phys.*, 71:735–778, Apr 1999. doi: 10.1103/RevModPhys.71.735. URL http://link.aps.org/doi/10.1103/RevModPhys.71.735.

[2] P.H. Diamond, S.-I. Itoh, K. Itoh, and T.S. Hahm. Zonal flows in plasma–a review. *Plasma Physics and Controlled Fusion*, 47(5):R35, 2005. URL http://stacks.iop.org/0741-3335/47/i=5/a=R01.

[3] G.W. Hammett, M.A. Beer, W. Dorland, S.C. Cowley, and S.A. Smith. Developments in the gyrofluid approach to tokamak turbulence simulations. *Plasma Physics and Controlled Fusion*, 35(8):973, 1993. URL http://stacks.iop.org/0741-3335/35/i=8/a=006.

[4] M.N. Rosenbluth and F.L. Hinton. Poloidal flow driven by ion-temperature-gradient turbulence in tokamaks. *Phys. Rev. Lett.*, 80: 724–727, Jan 1998. doi: 10.1103/PhysRevLett.80.724. URL http://link.aps.org/doi/10.1103/PhysRevLett.80.724.

[5] F.L. Hinton and M.N. Rosenbluth. Dynamics of axisymmetric $\mathbf{E} \times \mathbf{B}$ and poloidal flows in tokamaks. *Plasma Physics and Controlled Fusion*, 41(3A):A653, 1999. URL http://stacks.iop.org/0741-3335/41/i=3A/a=059.

[6] Y. Xiao, P.J. Catto, and W. Dorland. Effects of finite poloidal gyroradius, shaping, and collisions on the zonal flow residual[a)]. *Physics of Plasmas*, 14(5), 2007. doi: http://dx.doi.org/10.1063/1.2718519. URL http://scitation.aip.org/content/aip/journal/pop/14/5/10.1063/1.2718519;jsessionid=dP0sY9NmfupDeQ7f0APfGP8j.x-aip-live-06.

[7] H. Sugama and T.-H. Watanabe. Collisionless damping of zonal flows in helical systems. *Physics of Plasmas*, 13(1):012501, 2006. doi: http://dx.doi.org/10.1063/1.2149311. URL http://scitation.aip.org/content/aip/journal/pop/13/1/10.1063/1.2149311.

[8] H. Sugama and T.-H. Watanabe. Erratum: Collisionless damping of zonal flows in helical systems [*Physics of Plasmas* **13**, 012501

(2006)]. *Physics of Plasmas*, 14(7):079902, 2007. doi: http://dx.doi.org/10.1063/1.2748056. URL http://scitation.aip.org/content/aip/journal/pop/14/7/10.1063/1.2748056.

[9] S. Ferrando-Margalet, H. Sugama, and T.-H. Watanabe. Zonal flows and ion temperature gradient instabilities in multiple-helicity magnetic fields. *Physics of Plasmas*, 14(12):122505, 2007. doi: http://dx.doi.org/10.1063/1.2813182. URL http://scitation.aip.org/content/aip/journal/pop/14/12/10.1063/1.2813182.

[10] A. Mishchenko, P. Helander, and A. Könies. Collisionless dynamics of zonal flows in stellarator geometry. *Physics of Plasmas*, 15(7), 2008. doi: http://dx.doi.org/10.1063/1.2963085. URL http://scitation.aip.org/content/aip/journal/pop/15/7/10.1063/1.2963085.

[11] P Helander, A Mishchenko, R Kleiber, and P Xanthopoulos. Oscillations of zonal flows in stellarators. *Plasma Physics and Controlled Fusion*, 53 (5):054006, 2011. URL http://stacks.iop.org/0741-3335/53/i=5/a=054006.

[12] P. Xanthopoulos, A. Mischchenko, P. Helander, H. Sugama, and T.-H. Watanabe. Zonal flow dynamics and control of turbulent transport in stellarators. *Phys. Rev. Lett.*, 107:245002, Dec 2011. doi: 10.1103/PhysRevLett.107.245002. URL http://link.aps.org/doi/10.1103/PhysRevLett.107.245002.

[13] T.-H. Watanabe, H. Sugama, and S. Ferrando-Margalet. Reduction of turbulent transport with zonal flows enhanced in helical systems. *Phys. Rev. Lett.*, 100:195002, May 2008. doi: 10.1103/PhysRevLett.100.195002. URL http://link.aps.org/doi/10.1103/PhysRevLett.100.195002.

[14] Y. Xiao and P.J. Catto. Short wavelength effects on the collisionless neoclassical polarization and residual zonal flow level. *Physics of Plasmas*, 13(10), 2006. doi: http://dx.doi.org/10.1063/1.2358497. URL http://scitation.aip.org/content/aip/journal/pop/13/10/10.1063/1.2358497.

[15] F. Jenko, W. Dorland, M. Kotschenreuther, and B.N. Rogers. Electron temperature gradient driven turbulence. *Physics of Plasmas*, 7(5):1904–1910, 2000. doi: http://dx.doi.org/10.1063/1.874014. URL http://scitation.aip.org/content/aip/journal/pop/7/5/10.1063/1.874014.

[16] H. Sugama and T.-H. Watanabe. Dynamics of zonal flows in helical systems. *Phys. Rev. Lett.*, 94:115001, Mar 2005. doi: 10.1103/

PhysRevLett.94.115001. URL http://link.aps.org/doi/10.1103/PhysRevLett.94.115001.

[17] N. Winsor, J.L. Johnson, and J.M. Dawson. Geodesic acoustic waves in hydromagnetic systems. *Physics of Fluids*, 11(11):2448–2450, 1968. doi: 10.1063/1.1691835. URL http://aip.scitation.org/doi/abs/10.1063/1.1691835.

[18] J.A. Alonso, E. Sanchez, I. Calvo, J.L. Velasco, S. Perfilov, A. Chmyga, L.G. Eliseev, L.I. Krupnik, T. Estrada, R. Kleiber, K.J. McCarthy, A.V. Melnikov, P. Monreal, F.I. Parra, A.I. Zhezhera, and the TJ-II Team. Observation of oscillatory radial electric field relaxation in a helical plasma. *Accepted for publication in Physical Review Letters. ArXiv e-prints*, September 2016. URL https://arxiv.org/pdf/1609.00281.

[19] P. Monreal, I. Calvo, E. Sánchez, F.I. Parra, A. Bustos, A. Könies, R. Kleiber, and T. Görler. Residual zonal flows in tokamaks and stellarators at arbitrary wavelengths. *Plasma Physics and Controlled Fusion*, 58(4):045018, 2016. URL http://stacks.iop.org/0741-3335/58/i=4/a=045018.

[20] P. Monreal, E. Sánchez, I. Calvo, A. Bustos, F. I. Parra, A. Mishchenko, A. Könies, and R. Kleiber. Semianalytical calculation of the zonal-flow oscillation frequency in stellarators. *Accepted for publication in Plasma Physics and Controlled Fusion. ArXiv e-prints*, January 2017. URL https://arxiv.org/abs/1701.02722.

[21] J. Sánchez, D. Alegre, A. Alonso, J. Alonso, P. Álvarez, J. Arévalo, E. Ascasíbar, A. Baciero, D. Baiao, E. Blanco, M. Borchardt, J. Botija, A. Bustos, E. de la Cal, I. Calvo, A. Cappa, D. Carralero, R. Carrasco, F. Castejón, R. Castro, G. Catalán, A.A. Chmyga, M. Chamorro, L. Eliseev, T. Estrada, F. Fernández, J.M. Fontdecaba, L. García, R. García-Gómez, P. García-Sánchez, S. da Graca, J. Guasp, R. Hatzky, J. Hernández, J. Hernanz, J. Herranz, C. Hidalgo, J.A. Jiménez, A. Jiménez-Denche, I. Kirpitchev, R. Kleiber, A.D. Komarov, A.S. Kozachok, L. Krupnik, F. Lapayese, M. Liniers, D. López-Bruna, A. López-Fraguas, J. López-Razola, A. Martín, F. Martín-Díaz, F. Martín-Hernández, A.B. Martín-Rojo, J. Martínez-Fernández, K.J. McCarthy, F. Medina, M. Medrano, L. Melón, A.V. Melnikov, P. Méndez, B. van Milligen, P. Monreal, M. Navarro, I.S. Nedzelskiy, M.A. Ochando, J. Olivares, E. Oyarzábal, J.L. de Pablos, L. Pacios, I. Pastor, M.A. Pedrosa, A. de la Peña, A. Pereira, A. Petrov, S. Petrov, A.B. Portas, E. Rincón, L. Ríos, C. Rodríguez, B. Rojo, J.A. Romero, A. Ros, M. Sánchez, E. Sánchez, E. Sánchez-Sarabia, K. Sarksian, J.A. Sebastián, C. Silva, E.R. Solano, A. Soleto, B. Sun, F.L. Tabarés,

D. Tafalla, M. Tereshchenko, A. Tolkachev, J. Vega, G. Velasco, J.L. Velasco, G. Wolfers, and B. Zurro. Dynamics of flows and confinement in the TJ-II stellarator. *Nuclear Fusion*, 53(10):104016, 2013. URL http://stacks.iop.org/0029-5515/53/i=10/a=104016.

[22] E. Sánchez, R. Kleiber, R. Hatzky, M. Borchardt, P. Monreal, F. Castejón, A. López-Fraguas, X. Sáez, J.L. Velasco, I. Calvo, A. Alonso, and D. López-Bruna. Collisionless damping of flows in the TJ-II stellarator. *Plasma Physics and Controlled Fusion*, 55(1):014015, 2013. URL http://stacks.iop.org/0741-3335/55/i=1/a=014015.

[23] J. Sánchez, D. Alegre, A. Alonso, J. Alonso, P. Alvarez, J. Arévalo, E. Ascasíbar, A. Baciero, D. Baiao, J.M. Barcala, E. Blanco, M. Borchardt, J. Botija, S. Cabrera, E. de la Cal, I. Calvo, A. Cappa, R. Carrasco, F. Castejón, R. Castro, A. De Castro, G. Catalán, A.A. Chmyga, M. Chamorro, A. Dinklage, L. Eliseev, T. Estrada, F. Fernández-Marina, J.M. Fontdecaba, L. García, R. García-Gómez, J.M. García-Rega na, J. Guasp, R. Hatzky, J. Hernández, J. Herranz, C. Hidalgo, E. Hollmann, J.A. Jiménez, A. Jiménez-Denche, I. Kirpitchev, R. Kleiber, A.D. Komarov, A.S. Kozachok, L. Krupnik, F. Lapayese, M. Liniers, B. Liu, D. López-Bruna, A. López-Fraguas, J. López-Razola, A. Martín de Aguilera, F. Martín-Díaz, F. Martín-Hernández, A.B. Martín-Rojo, J. Martínez-Fernández, K.J. McCarthy, F. Medina, M. Medrano, L. Melón, A.V. Melnikov, P. Méndez, B. van Milligen, A. Molinero, P. Monreal, R. Moreno, M. Navarro, I.S. Nedzelskiy, M.A. Ochando, J. Olivares, E. Oyarzábal, J.L. de Pablos, L. Pacios, I. Pastor, M.A. Pedrosa, A. de la Peña, A. Pereira, A. Petrov, S. Petrov, A.B. Portas, G. Rattá, E. Rincón, L. Ríos, C. Rodríguez, B. Rojo, A. Ros, M. Sánchez, E. Sánchez, E. Sánchez-Sarabia, K. Sarksian, S. Satake, J.A. Sebastián, C. Silva, E.R. Solano, A. Soleto, B. Sun, F.L. Tabarés, D. Tafalla, S. Tallents, A. Tolkachev, J. Vega, G. Velasco, J.L. Velasco, G. Wolfers, M. Yokoyama, and B. Zurro. Transport, stability and plasma control studies in the TJ-II stellarator. *Nuclear Fusion*, 55(10): 104014, 2015. URL http://stacks.iop.org/0029-5515/55/i=10/a=104014.

[24] P.J. Catto. Linearized gyro-kinetics. *Plasma Physics*, 20(7):719, 1978. URL http://stacks.iop.org/0032-1028/20/i=7/a=011.

[25] E.A. Frieman and L. Chen. Nonlinear gyrokinetic equations for low-frequency electromagnetic waves in general plasma equilibria. *Physics of Fluids*, 25(3):502–508, 1982. doi: http://dx.doi.org/10.1063/1.863762. URL http://scitation.aip.org/content/aip/journal/pof1/25/3/10.1063/1.863762.

[26] A.J. Brizard and T.S. Hahm. Foundations of nonlinear gyrokinetic theory. *Rev. Mod. Phys.*, 79:421–468, Apr 2007. doi: 10.1103/RevModPhys.79.421. URL http://link.aps.org/doi/10.1103/RevModPhys.79.421.

[27] F.I. Parra and I. Calvo. Phase-space lagrangian derivation of electrostatic gyrokinetics in general geometry. *Plasma Physics and Controlled Fusion*, 53(4):045001, 2011. URL http://stacks.iop.org/0741-3335/53/i=4/a=045001.

[28] Daniel H.E. Dubin, John A. Krommes, C. Oberman, and W.W. Lee. Nonlinear gyrokinetic equations. *Physics of Fluids*, 26(12):3524–3535, 1983. doi: http://dx.doi.org/10.1063/1.864113. URL http://scitation.aip.org/content/aip/journal/pof1/26/12/10.1063/1.864113.

[29] F.I. Parra and M. Barnes. Intrinsic rotation in tokamaks: theory. *Plasma Physics and Controlled Fusion*, 57(4):045002, 2015. URL http://stacks.iop.org/0741-3335/57/i=4/a=045002.

[30] I. Calvo and F.I. Parra. Long-wavelength limit of gyrokinetics in a turbulent tokamak and its intrinsic ambipolarity. *Plasma Physics and Controlled Fusion*, 54(11):115007, 2012. URL http://stacks.iop.org/0741-3335/54/i=11/a=115007.

[31] F.I. Parra and M. Barnes. Equivalence of two different approaches to global δf gyrokinetic simulations. *Plasma Physics and Controlled Fusion*, 57(5):054003, 2015. URL http://stacks.iop.org/0741-3335/57/i=5/a=054003.

[32] J.R. Cary and S.G. Shasharina. Helical plasma confinement devices with good confinement properties. *Phys. Rev. Lett.*, 78:674–677, Jan 1997. doi: 10.1103/PhysRevLett.78.674. URL http://link.aps.org/doi/10.1103/PhysRevLett.78.674.

[33] J.R. Cary and S.G. Shasharina. Omnigenity and quasihelicity in helical plasma confinement systems. *Physics of Plasmas*, 4(9):3323–3333, 1997. doi: http://dx.doi.org/10.1063/1.872473. URL http://scitation.aip.org/content/aip/journal/pop/4/9/10.1063/1.872473.

[34] F.I. Parra, I. Calvo, P. Helander, and M. Landreman. Less constrained omnigeneous stellarators. *Nuclear Fusion*, 55(3):033005, 2015. URL http://stacks.iop.org/0029-5515/55/i=3/a=033005.

[35] A. Könies. A kinetic magnetohydrodynamic energy integral in three dimensional geometry. *Physics of Plasmas*, 7(4):1139–1147, 2000. doi: http://dx.doi.org/10.1063/1.873922. URL http://scitation.aip.org/content/aip/journal/pop/7/4/10.1063/1.873922.

[36] A. Könies, A. Mishchenko, and R. Hatzky. From kinetic MHD in stellarators to a fully kinetic description of wave particle interaction. *AIP Conference Proceedings*, 1069(1):133–143, 2008. doi: http://dx.doi.org/10.1063/1.3033696. URL `http://scitation.aip.org/content/aip/proceeding/aipcp/10.1063/1.3033696`.

[37] G. Jost, T.M. Tran, W.A. Cooper, L. Villard, and K. Appert. Global linear gyrokinetic simulations in quasi-symmetric configurations. *Physics of Plasmas*, 8(7), 2001.

[38] R. Kleiber and R. Hatzky. A partly matrix-free solver for the gyrokinetic field equation in three-dimensional geometry. *Computer Physics Communications*, 183(2):305 – 308, 2012. ISSN 0010-4655. doi: http://dx.doi.org/10.1016/j.cpc.2011.10.008. URL `http://www.sciencedirect.com/science/article/pii/S0010465511003365`.

[39] T. Görler, X. Lapillonne, S. Brunner, T. Dannert, F. Jenko, F. Merz, and D. Told. The global version of the gyrokinetic turbulence code GENE. *Journal of Computational Physics*, 230(18):7053 – 7071, 2011. ISSN 0021-9991. doi: http://dx.doi.org/10.1016/j.jcp.2011.05.034. URL `http://www.sciencedirect.com/science/article/pii/S0021999111003457`.

[40] The GENE code. URL `http://genecode.org`.

[41] P. Xanthopoulos, W. A. Cooper, F. Jenko, Yu. Turkin, A. Runov, and J. Geiger. A geometry interface for gyrokinetic microturbulence investigations in toroidal configurations. *Physics of Plasmas*, 16(8), 2009. doi: http://dx.doi.org/10.1063/1.3187907. URL `http://scitation.aip.org/content/aip/journal/pop/16/8/10.1063/1.3187907`.

[42] C. Schwab. Ideal magnetohydrodynamics: Global mode analysis of three-dimensional plasma configurations. *Physics of Fluids B: Plasma Physics*, 5(9):3195–3206, 1993. doi: 10.1063/1.860656. URL `http://dx.doi.org/10.1063/1.860656`.

[43] C. Nührenberg. Global ideal magnetohydrodynamic stability analysis for the configurational space of Wendelstein 7-X. *Physics of Plasmas*, 3(6):2401–2410, 1996. doi: 10.1063/1.871924. URL `http://dx.doi.org/10.1063/1.871924`.

[44] C. Nührenberg. Compressional ideal magnetohydrodynamics: Unstable global modes, stable spectra, and Alfvén eigenmodes in Wendelstein 7-X-type equilibria. *Physics of Plasmas*, 6(1):137–147, 1999. doi: 10.1063/1.873268. URL `http://dx.doi.org/10.1063/1.873268`.

[45] A. Könies, T. Feher, P. Lauber, A. Mishchenko, R. Kleiber, M. Borchardt, S. Briguglio, G. Vlad, N. Gorelenkov, M. Isaev, R. Hatzky, D. Spong, Y. Todo, and W. Cooper. Benchmark of Gyrokinetic, Kinetic MHD and Gyrofluid Codes for the Linear Calculation of Fast Particle Driven TAE Dynamics. volume IAEA-CN–197, 2012. URL http://www-naweb.iaea.org/napc/physics/FEC/FEC2012/papers/437_ITRP134.pdf.

[46] Ph. Lauber, S. Günter, M. Brüdgam, A. Könies, and S.D. Pinches. Kinetic Properties of Alfvén Modes in Tokamak Plasmas. *AIP Conference Proceedings*, 871(1):147–156, 2006. doi: 10.1063/1.2404547. URL http://aip.scitation.org/doi/abs/10.1063/1.2404547.

[47] Ph. Lauber, S. Günter, A. Könies, and S.D. Pinches. LIGKA: A linear gyrokinetic code for the description of background kinetic and fast particle effects on the MHD stability in tokamaks. *Journal of Computational Physics*, 226(1):447 – 465, 2007. ISSN 0021-9991. doi: http://dx.doi.org/10.1016/j.jcp.2007.04.019. URL http://www.sciencedirect.com/science/article/pii/S0021999107001660.

[48] C. Slaby, A. Könies, and R. Kleiber. Numerical investigation of non-perturbative kinetic effects of energetic particles on toroidicity-induced Alfvén eigenmodes in tokamaks and stellarators. *Physics of Plasmas*, 23(9):092501, 2016. doi: http://dx.doi.org/10.1063/1.4961916. URL http://scitation.aip.org/content/aip/journal/pop/23/9/10.1063/1.4961916.

[49] S.P. Hirshman and J.C. Whitson. Steepest-descent moment method for three-dimensional magnetohydrodynamic equilibria. *Physics of Fluids (1958-1988)*, 26(12):3553–3568, 1983. doi: http://dx.doi.org/10.1063/1.864116. URL http://scitation.aip.org/content/aip/journal/pof1/26/12/10.1063/1.864116.

[50] The GSL-GNU Scientific Library. URL http://www.gnu.org/software/gsl.

[51] Brian Gough. *GNU Scientific Library Reference Manual - Third Edition*. Network Theory Ltd., 3rd edition, 2009. ISBN 0954612078, 9780954612078. URL http://www.gnu.org/software/gsl/manual/gsl-ref.html.

[52] A.Y. Aydemir. A unified Monte Carlo interpretation of particle simulations and applications to non-neutral plasmas. *Physics of Plasmas*, 1 (4):822–831, 1994. doi: 10.1063/1.870740. URL http://dx.doi.org/10.1063/1.870740.

[53] R.C. Grimm, J.M. Greene, and J.L. Johnson. *Computation of the magnetohydrodynamic spectrum in axisymmetric toroidal confinement systems*, pages 253–280. 1976. URL http://adsabs.harvard.edu/abs/1976cofu.book..253G.

[54] V. Kornilov, R. Kleiber, and R. Hatzky. Gyrokinetic global electrostatic ion-temperature-gradient modes in finite β equilibria of Wendelstein 7-X. *Nuclear Fusion*, 45(4):238, 2005. URL http://stacks.iop.org/0029-5515/45/i=4/a=003.

[55] K. Kauffmann, R. Kleiber, R. Hatzky, and M. Borchardt. Global linear gyrokinetic simulations for LHD including collisions. *Journal of Physics: Conference Series*, 260(1):012014, 2010. URL http://stacks.iop.org/1742-6596/260/i=1/a=012014.

[56] R. Kleiber, R. Hatzky, A. Könies, K. Kauffmann, and P. Helander. An improved control-variate scheme for particle-in-cell simulations with collisions. *Computer Physics Communications*, 182(4):1005 – 1012, 2011. ISSN 0010-4655. doi: http://dx.doi.org/10.1016/j.cpc.2010.12.045. URL http://www.sciencedirect.com/science/article/pii/S0010465510005382.

[57] M. Borchardt, R. Kleiber, and W. Hackbusch. A fast solver for the gyrokinetic field equation with adiabatic electrons. *Journal of Computational Physics*, 231(18):6207 – 6212, 2012. ISSN 0021-9991. doi: http://dx.doi.org/10.1016/j.jcp.2012.06.001. URL http://www.sciencedirect.com/science/article/pii/S0021999112003002.

[58] M.J. Pueschel, T. Dannert, and F. Jenko. On the role of numerical dissipation in gyrokinetic Vlasov simulations of plasma microturbulence. *Computer Physics Communications*, 181(8):1428 – 1437, 2010. ISSN 0010-4655. doi: http://dx.doi.org/10.1016/j.cpc.2010.04.010. URL http://www.sciencedirect.com/science/article/pii/S0010465510001219.

[59] X. Lapillonne, B.F. McMillan, T. Görler, S. Brunner, T. Dannert, F. Jenko, F. Merz, and L. Villard. Nonlinear steady state benchmark of global gyrokinetic codes. *Physics of Plasmas*, 17(11):112321, 2010. doi: 10.1063/1.3518118. URL http://dx.doi.org/10.1063/1.3518118.

[60] Y. Osamu and S. Hideo. Collisionless kinetic-fluid simulation of zonal flows in non-circular tokamaks. *Physics of Plasmas*, 19(9), 2012. doi: http://dx.doi.org/10.1063/1.4751451. URL http://scitation.aip.org/content/aip/journal/pop/19/9/10.1063/1.4751451.

[61] The HYDRA supercomputer. URL http://www.mpcdf.mpg.de/services/computing/hydra/about-the-system.

[62] The MareNostrum III. URL http://www.bsc.es/marenostrum-support-services/mn3.

[63] The VMEC wiki. URL http://vmecwiki.pppl.wikispaces.net/VMEC.

[64] I. Calvo, F.I. Parra, J.L. Velasco, and J.A. Alonso. Stellarators close to quasisymmetry. *Plasma Physics and Controlled Fusion*, 55(12):125014, 2013. URL http://stacks.iop.org/0741-3335/55/i=12/a=125014.

[65] J.L. Velasco, K.J. McCarthy, N. Panadero, S. Satake, D. López-Bruna, A. Alonso, I. Calvo, A. Dinklage, T. Estrada, J.M. Fontdecaba, J. Hernández, R. García, F. Medina, M. Ochando, I. Pastor, S. Perfilov, E. Sánchez, A. Soleto, B.Ph. Van Milligen, A. Zhezhera, and the TJ-II Team. Particle transport after pellet injection in the TJ-II stellarator. *Plasma Physics and Controlled Fusion*, 58(8):084004, 2016. URL http://stacks.iop.org/0741-3335/58/i=8/a=084004.

[66] A.V. Melnikov, A. Alonso, E. Ascasibar, R. Balbin, A. Chmyga, Y. N. Dnestrovskij, L. Eliseev, T. Estrada, J. Fontdecaba, C. Fuentes, et al., and the TJ-II Team. Plasma potential evolution study by HIBP diagnostic during NBI experiments in the TJ-II stellarator. *Fusion Science and Technology*, 51(1):31, 2007. URL http://www.ans.org/pubs/journals/fst/a_1284.

[67] A.V. Melnikov, C. Hidalgo, L.G. Eliseev, E. Ascasibar, A.A. Chmyga, K.S. Dyabilin, I.A. Krasilnikov, V.A. Krupin, L.I. Krupnik, S.M. Khrebtov, A.D. Komarov, A.S. Kozachek, D. López-Bruna, S.E. Lysenko, V.A. Mavrin, J.L. de Pablos, I. Pastor, S.V. Perfilov, M.A. Pedrosa, R.V. Shurygin, V.A. Vershkov, T-10 Team, and TJ-II Team. Plasma potential and turbulence dynamics in toroidal devices (survey of T-10 and TJ-II experiments). *Nuclear Fusion*, 51(8):083043, 2011. URL http://stacks.iop.org/0029-5515/51/i=8/a=083043.

[68] K. J. McCarthy, N. Panadero, I. Arapoglou, S. K. Combs, J. B. O. Caughman, E. de la Cal, C. Foust, R. García Gomez, J. Hernandez Sanchez, F. Martín Hernandez, M. Navarro Santana, I. Pastor Diaz, M. C. Rodriguez Fernandez, and J. L. Velasco Garasa. A Pellet Injector And Associated Plasma Diagnostics For Performing Plasma Studies And Fuelling In The TJ-II Stellarator. In *1st EPS conference on Plasma Diagnostics (ECPD2015)*, page 134, 2015. URL https://pos.sissa.it/archive/conferences/240/134/ECPD2015_134.pdf.

[69] T. Happel, T. Estrada, E. Blanco, V. Tribaldos, A. Cappa, and A. Bustos. Doppler reflectometer system in the stellarator TJ-II. *Review of Scientific Instruments*, 80(7):073502, 2009. doi: 10.1063/1.3160106. URL http://dx.doi.org/10.1063/1.3160106.

[70] K. C. Shaing, E. C. Crume Jr., J. S. Tolliver, S. P. Hirshman, and W. I. van Rij. Bootstrap current and parallel viscosity in the low collisionality regime in toroidal plasmas. *Physics of Fluids B: Plasma Physics*, 1(1): 148–152, 1989. doi: 10.1063/1.859093. URL `http://dx.doi.org/10.1063/1.859093`.

[71] S. Braun, P. Helander, E.A. Belli, and J. Candy. Effect of impurities on collisional zonal flow damping in tokamaks. *Plasma Physics and Controlled Fusion*, 51(6):065011, 2009. URL `http://stacks.iop.org/0741-3335/51/i=6/a=065011`.